FIBER RANDOM GRATING AND ITS APPLICATIONS

by

Yanping Xu

Thesis submitted to the
Faculty of Graduate and Postdoctoral Studies
In partial fulfillment of the requirements for the Degree of

Doctor of Philosophy

in

Physics

Ottawa-Carleton Institute for Physics
University of Ottawa
Ottawa, Ontario, Canada

To my family

Abstract

Femtosecond (fs) laser micromachining has been a useful technique either to modify and remove materials or to change the properties of a material, and can be applied to transparent and absorptive substances. Recently high-power fs laser radiation has drawn intensive attention for the induction of refractive index change to fabricate micro-structures in dielectric materials. This thesis studies the optical properties of a novel fiber random grating fabricated by fs laser micromachining technique and extends its applications from optical sensing to random fiber lasers and optical random bit generations.

The thesis mainly consists of three parts. In the first part, the physical mechanism behind the fs laser micromachining technique and the fabrication of the fiber random grating are introduced. By employing a wavelength-division spectral cross-correlation algorithm, a novel multi-parameter fiber-optic sensor based on the fiber random grating is proposed and demonstrated to realize simultaneous measurements of temperature, axial strain, and surrounding refractive index.

In the second part, Brillouin random fiber laser (BRFL) and Erbium-doped fiber random laser (EDFRL) are introduced, respectively. Firstly, we propose a novel Brillouin random fiber laser with a narrow linewidth of ~860 Hz based on the bi-directionally pumped stimulated Brillouin scattering (SBS) in a 10-km-long optical fiber. A random fiber Fabry-Perot (FP) resonator is built up through the pump depletion effects of SBS at both ends of the fiber. The novel laser is successfully applied for linewidth characterization beyond 860 Hz of light source under test. Secondly, the random grating-based FP resonator is introduced to build up a novel BRFL with narrow-linewidth of ~45.8Hz and reduced lasing threshold. The

intensity and frequency noises of the proposed random laser are effectively suppressed due to the reduced resonating modes and mode competition. Finally, the fiber random grating is used as random distributed feedback in an EDFRL to achieve both static (temperature, strain) and dynamic (ultrasound) parameter sensing. Multiple lasing lines with high signal-to-noise ratio (SNR) up to 40dB are achieved, which gives an access for a high-fidelity multiple-static-parameter sensing application. By monitoring the wavelength shifts of each peak, temperature and strain have been simultaneously measured with small errors. The fiber random grating in the EDFRL is also able to sense the ultrasound waves. By achieving single mode lasing with the EDFRL, ultrasound waves with frequencies from 20kHz to 0.8MHz could be detected with higher sensitivity and SNR improvement up to 20dB compared with conventional piezoelectric acoustic sensors.

In the third part, we demonstrate that a semiconductor laser perturbed by the distributed feedback from a fiber random grating can emit light chaotically without the time delay signature (TDS). A theoretical model is developed by modifying the Lang-Kobayashi model to numerically explore the chaotic dynamics of the laser diode subjected to the random distributed feedback. It is predicted that the random distributed feedback is superior to the single reflection feedback in suppressing the TDS. In experiments, The TDS with the maximum suppression is achieved with a value of 0.0088, which is the smallest to date.

Acknowledgments

It has been almost six years since I joint the Fiber Optics Group in University of Ottawa. During this long journey pursuing for my Ph.D., I have grown up from a boy dreaming to be a scientist to a man with abilities to conduct research. There were moments of frustration and moments of happiness interwoven in this period, but most impressively, moments of self-recognition and enjoying the scientific research. This thesis cannot be finished without the help of many people contributed in many ways. I'm so honored to have this opportunity to thank all the people who have helped me over the past six years. I will cherish this unforgettable experience forever.

First of all, I would like to sincerely thank my supervisors, Prof. Xiaoyi Bao and Prof. Ping Lu, for their careful guidance and support in my graduate study. It is my great honor to know Prof. Bao and Prof. Lu both at professional and personal level. Prof. Bao, with her strong passion, broad knowledge and thoughtful insight in research, impresses me a lot. Her creative ideas, rigorous attitude and rich research experience have taught and inspired me to challenge the useful but difficult research topics one by one. Prof. Lu provided me not only a lot of insightful and helpful suggestions and ideas during my research process, but also invaluable kind care with my daily lives. His encouragement and constant support greatly increase my confidence in research and contribute to my successful completion of Master and Ph.D. studies. I would also express my great gratitude to Prof. Liang Chen for his precious advices and instructive discussions, which significantly improves the quality of this thesis. I also thank Prof. Stephen Mihailov in National Research Council Canada for his help in experimental arrangements for device fabrication and valuable suggestions and revisions

on research topics and manuscripts.

Many thanks are given to Dr. Ping Lu for his great ideas, useful suggestions and thoughtful discussions. Dr. Lu has provided much assistance and guidance when I started my research. He is a kind and open-minded person who is always willing to share ideas and launch discussions with me. It is no exaggeration to say that he helped me a lot to knock the door for research and this thesis cannot be completed without his guidance.

I would like to specially thank Dr. Zengguang Qin. He is more than a research partner but one of my sincere friends. His comments and suggestions have greatly benefited me during my research. He was always with me whenever I got confused, lost and disappointed.

I would like to express my gratitude to Prof. Mingjiang Zhang, Dr. Yang Lu, and Prof. Zhonghua Ou. They provided tremendous assistance and guidance with my researches and experiments. It is a great pleasure to collaborate with them to work on several exciting research projects.

I'm also thankful to Mr. Dao Xiang and Ms. Meiqi Ren, who have been my sincere friends in the Fiber Optics group. We attended courses and conducted experiments together, shared ideas and had discussions, and experienced lots of happy moments when participating the NSERC CREATE SERA program. I also thank Mr. Song Gao and Dr. Liang Zhang for helpful discussions and assistance when I'm depressed and confused.

I would like to acknowledge funding support by the NSERC CREATE SERA program over the past three years. I thank the program director, Prof. Mark Green in Queen's University, for his constant help and support in the program and internship applications.

Special thanks will be given to Mr. Terry Gerritsen, Dr. Richard MacRosty, Mr. Ravi Pula, and Mr. Jakob Janzen, my colleagues in Control Technologies of Hatch Ltd., where I spent four months doing my internship. It is a memorable experience working in Hatch with

such nice guys and I wouldn't learn a lot without their advices and suggestions. In particular, I would like to express my gratitude to John, who is the owner of the house where I lived in Mississauga, for his kind encouragements and comforts when I was low during the internship.

I am thankful to all the other colleagues in Fiber Optics group — Prof. Zhengying Li, Prof. Ping Han, Dr. Chen Wang, Mr. Bhavaye Saxena, Dr. Daisy Williams, Mr. Robert Chutu Li, Dr. Yang Li, Dr. Qian He, Mr. Tian Wang, Prof. Chunhua Wang, Mr. Benoit Vanus. My life in the laboratory was enriched by their company.

I am thankful to the former colleagues in Fiber Optics group during my Master studies — Dr. Ganbin Lin, Mr. Jia Song, Dr. Wenhai Li, Dr. Xiaozhen Wang, Dr. Dapeng Zhou, Dr. Meng Pang, Prof. Yuangang Lu, Mr. Jeremie Harris and Mr. Graeme Niedermayer for their useful technical assistance and discussions.

Special thanks go to my fiancée Muzi Li for her love and support. Her encouragement and understanding through the years allowed me to face challenges with great confidence. Finally, I am deeply indebted to my family in China, especially my parents. It is their encouragement, enduring love and understanding for me to pursue my graduate study.

It is impossible to remember all, and I apologize to those I have inadvertently left out.

Again, thank you all!

Statement of originality

This work contains no material which has been accepted for the award of any other degree or diploma in any university or other tertiary institution and, to the best of my knowledge and belief, contains no material previously published or written by another person, except where due reference has been made in the text.

I give consent to this copy of my thesis, when deposited in the University Library, being available for loan and photocopying.

SIGNED: ……..

DATE: ……...

Supervisors: Prof. Xiaoyi Bao and Prof. Ping Lu

Contents

Abstract iii

Acknowledgments v

Statement of originality viii

List of Figures xi

List of Tables xiv

List of Acronyms xv

1 Introduction 1
- 1.1 Background and motivation ... 1
  - 1.1.1 Femtosecond laser micromachining and fiber Bragg grating fabricated by fs laser 1
  - 1.1.2 Random lasers ... 5
  - 1.1.3 Chaotic semiconductor lasers ... 11
- 1.2 Thesis contribution ... 13
- 1.3 Thesis outline ... 16

2 Fiber random grating and its application in fiber-optic sensing 18
- 2.1 Background ... 18
- 2.2 Fabrication of fiber random grating ... 21
- 2.3 Optical properties of fiber random grating ... 23
- 2.4 Comparison with regular FBG and random FBG ... 26
- 2.5 Fiber random grating based multi-parameter sensor ... 29
- 2.6 Conclusion ... 37

3 Introduction of random fiber lasers 38
- 3.1 Random feedback mechanisms in optical fibers ... 38
  - 3.1.1 Intrinsic Rayleigh scattering ... 39
  - 3.1.2 EnhancedRayleighscattering ... 42
- 3.2 Random fiber lasers with different gain mechanisms ... 44
  - 3.2.1 Raman random fiber laser ... 44
  - 3.2.2 Brillouin random fiber laser ... 49
  - 3.2.3 Erbium-doped fiber random laser ... 55
- 3.3 Lasing mode and linewidth characterization ... 60
  - 3.3.1 Lasing mode ... 60
  - 3.3.2 Linewidth characterization ... 64
- 3.4 Intensity noise measurement ... 68
- 3.5 Frequency noise measurement ... 71
- 3.6 Applications of random fiber lasers ... 76

4 Random Fabry–Perot resonator-based sub-kHz Brillouin random fiber laser and its application in linewidth measurement 79
- 4.1 Introduction ... 79

4.2 Theoretical model 82
4.3 Experimental results 87
4.4 Conclusion 91

5 Low noise Brillouin random fiber laser with random grating based resonator 93
5.1 Introduction 93
5.2 Experimental configuration and theoretical model 95
5.3 Experimental results 98
5.4 Conclusion 106

6 Multi-parameter sensor based on EDF random fiber lasers with fiber random grating feedback 107
6.1 Introduction 108
6.2 Experimental configuration and theoretical model 110
6.3 Experimental results 114
6.4 Conclusion 118

7 Highly sensitive fiber random grating based EDF random fiber laser sensor for ultrasound detection 119
7.1 Introduction 120
7.2 Experimental configuration and operation principle 123
7.3 Experimental results 130
7.4 Conclusion 134

8 Time-delay signature suppression in a chaotic semiconductor laser by fiber random grating induced distributed feedback 136
8.1 Introduction 137
8.2 Experimental configuration 138
8.3 Theoretical model and simulated results 140
8.4 Experimental results 144
8.5 Conclusion 149

9 Summary and future work 150
9.1 Summary 150
9.2 Future work 152

Curriculum Vitae 155

Publications 156

Bibliography 159

List of Figures

1-1. Schematic of the fs laser incident on glass and diagram of the excitation of electrons to the conduction band. 3
1-2. Schematic of a regular uniform FBG and its transmission and reflection spectra.....4
1-3. Schematics of (a) conventional Fabry-perot resonator and (b) random lasing in a disordered medium [13]. 6
1-4. Schematic of Rayleigh scattering based random fiber laser [26]. 9
2-1. Experimental setup of the plane-by-plane fs laser micromachining system with microscopic images of the fiber random grating sample. 21
2-2. Experimental setup for monitoring the reflection and transmission spectra of random grating. 24
2-3. Reflection spectra of (a) regular FBG, (b) random FBG, and (c) fiber random grating.. 26
2-4. Correlation analysis flow chart for simulated reflection spectra. 31
2-5. Measured reflection spectra of the random grating at reference temperature (a) and changed temperature (b); (c) Auto-correlation spectrum of (a); (d) Cross-correlation spectrum of (a) and (b). 33
2-6. (a)Three spectrum subsections selected in the reflection spectrum of fiber-optic random grating; cross-correlation peak wavelength shift calibration results for (b) temperature, (c) strain, and (d) refractive index. 35
3-1. Schematic diagram of Raman scattering from a quantum mechanical viewpoint [77].. 45
3-2. Normalized Raman gain spectrum for a fused silica fiber when pump and Stokes waves are copolarized (solid curve). The dotted curve shows the spectrum when the pump and Stokes waves are orthogonally polarized [77]....46
3-3. Different configurations of Raman random fiber lasers: (a) forward-pumped laser, (b) backward-pumped laser and (c) single-arm configuration. [26] 47
3-4. (a) Measured output power of Raman random fiber laser [27]; (b) Lasing spectra of Raman random fiber laser as a function of pump power [26]....49
3-5. Brillouin gain spectra of three fibers: (a) silica-core fiber, (b) depressed-cladding fiber, and (c) dispersion-shifted fiber. [85] 52
3-6. Experimental setup of first demonstration of BRFL [71]. 53
3-7. Cascaded fiber composed of three types of fibers with different Brillouin frequencies [86]. 54
3-8. Schematic of BRFL with half-open ring cavity [87]. 55
3-9. Energy level structure of the erbium ion and some common optical transitions. 56
3-10. Absorption and gain spectra of an EDF amplifier with core doped with germania [89]. 57
3-11. Experimental setup of inscribing FBGs with random spacing along a Er/Ge co-doped fiber [74]. 58
3-12. Experimental setup of half-open linear cavity RDF based random fiber laser [90]. 59
3-13. Schematic of a random fiber ring laser with Rayleigh feedback. 61
3-14. Resonance properties of random fiber ring laser with (a) flattened gain and (b) un-

flattened gain. 62
3-15. Schematic of the delayed self-heterodyne technique for laser linewidth measurement. 64
3-16. Schematic of the RIN measurement setup. 69
3-17. RIN comparison between half-open linear cavity Rayleigh random fiber laser (blue), half-open ring cavity random fiber laser with random grating feedback induced by CO_2 laser (red), and commercial fiber laser (green). [75] 70
3-18. (a) Conventional Fabry-Perot resonator with fixed cavity; (b) random fiber laser with random distributed feedback. 73
3-19. Experimental setup used to measure the laser phase and frequency noise [98]. 74
4-1. Configuration of random fiber FP resonator based Brillouin fiber laser. 84
4-2. (a) Power evolution of pump and Stokes light in SBS gain fiber; (b) Chaotic interference pattern in optical spectra of random FP resonator. 86
4-3. Experimental setup of the random fiber FP resonator based Brillouin fiber laser. 3→a: Conventional delayed self-heterodyne method; 3→b: Proposed linewidth measurement method. 87
4-4. Threshold (a) and linewidth measurement result (b) of the proposed BRFL. 88
4-5. Simulated (a) and experimental (b) statistical distribution of the resonating peak positions in 15MHz span; Inset of (a): Chaotic interference pattern in optical spectra of random FP resonator. 90
4-6. Laser linewidth measurements using conventional DSH method (a) and proposed method (b). 91
5-1. Configuration of BRFL with random grating based FP resonator and reflection spectra of random grating sample A and B. 95
5-2. Experimental setup of the BRFL with random grating based FP resonator; heterodyne method for linewidth characterization when Part A is replaced by Part B. 98
5-3. (a)Lasing thresholds of the BRFLs with random grating (red) and without random grating (black); Linewidths measured by the heterodyne method for cases with random grating (b) and without random grating (c). 99
5-4. RIN of the BRFLs with random grating (green) and without random grating (blue) and the reference fiber laser (red). 102
5-5. Frequency noise spectra of the BRFLs with random grating (green) and without random grating (blue) and the reference fiber laser (red). 104
6-1. The schematic experimental setup of the random grating based Erbium-doped fiber ring laser; the magnified figure is a schematic illustration of the backscattering within the random grating sample; EDFA: Erbium-doped fiber amplifier; PC: Polarization controller. 111
6-2. Simulated lasing output of the random grating based EDF ring laser with different input polarizations: (a) one lasing line, (b) two lasing lines, and (c) multiple lasing lines. 113
6-3. (a) Lasing thresholds indicated by the laser output power as a function of pump current for different numbers of emitted lasing lines. Experimental results of the lasing spectra with different input polarizations: (b) one lasing line, (c) two lasing lines, and (d) three lasing lines. 114
6-4. (a) Illustration of lasing line shifts as a result of temperature change; wavelength shift calibration results of temperature and strain measurements for Line 1(b) and Line 2 (c). 116

7-1. (a) Experimental setup of the fiber random grating based random laser sensor for ultrasound detection; (b) EDFA gain profile (Black) and reflected power spectrum from fiber random grating (Red); (c) Reflection spectrum of the fiber random grating; (d) Multi-wavelength lasing spectrum; (e) Single-wavelength lasing spectrum. 123
7-2. Radio frequency spectra of delayed self-heterodyne measurements for lasing output with mirror feedback (a) and random grating feedback (b). 125
7-3. (a) Normalized reflection spectrum of fiber random grating in the range between 1556nm and 1568nm; Selected lasing wavelengths at (b) 1558.024nm, (c) 1560.018nm, (d) 1562.014nm, and (e) 1565.026nm. 128
7-4. (a) Lasing thresholds of the proposed random fiber laser at the four selected lasing wavelengths; (b) Lasing spectra at the selected lasing wavelengths. 129
7-5. Temporal (a) and enlarged temporal (b) responses of the proposed random fiber laser ultrasound sensor; Spectral responses of the sensor for 0.5MHz ultrasonic wave (c) and ultrasound with different frequencies (d). 130
7-6. (a) SNR as a function of the ultrasound frequency at lasing wavelength of 1565.026nm and the corresponding smoothing curve; (b)-(d) Comparisons of the SNR curves among different lasing wavelengths. 132
7-7. Comparison of the SNR curves between the proposed random laser sensor and PZT sensor. 133
8-1. (a) Configuration of the laser diode subjected to fiber random grating feedback. OC: Optical Circulator; EDFA: Erbium Doped Fiber Amplifier; PC: Polarization Controller; Atn: Optical Attenuator; PD: Photo-detector; (b) Reflection spectrum of fiber random grating. Inset: enlarged reflection spectrum. 139
8-2. Simplified model of the randomly distributed scattering centers in fiber random grating. 140
8-3. Simulation results of (a) time domain series, (b) power spectra, and (c) ACFs for laser diode subjected to single reflection feedback (1) and random distributed feedback (2), respectively. 142
8-4. Computed TDS values of the chaotic laser subjected to single reflection feedback (black) and random distributed feedbacks from 10cm long random grating with 100 scattering centers (red), 10cm long random grating with 200 scattering centers (blue), 20cm long random grating with 100 scattering centers (dark cyan) as a function of feedback ratio. 143
8-5. Experimental results of (a) time domain series, (b) power spectra, and (c) ACFs for laser diode subjected to single mirror feedback (1) and random grating feedback (2), respectively. 144
8-6. Mutual information of simulated results for chaotic laser subjected to (a) single reflection feedback and (b) random distributed feedback with a feedback ratio of 0.09; Mutual information of experimental results for chaotic laser subjected to (c) single mirror feedback and (d) fiber random grating feedback with a feedback ratio of 0.22. 145
8-7. (a) TDS value of the chaotic laser subjected to the random grating feedback with the optimized input SOP to the fiber random grating sample; (b) Power spectra of the chaotic laser output with different input SOPs to the fiber random grating sample and the corresponding TDS values. 147

List of Tables

4-1. Simulation parameters 85

7-1. Sensitivities of the random laser sensor and PZT sensor.....134

List of Acronyms

ACF	Autocorrelation function
AFBG	Apodized fiber Bragg grating
AOM	Acousto-optic modulator
ASE	Amplified spontaneous emission
BRFL	Brillouin random fiber laser
CCD	Charge coupled device
CW	Continuous wave
DSH	Delayed self-heterodyne
EDF	Erbium-doped fiber
EDFA	Erbium-doped fiber amplifier
EDFRL	Erbium-doped fiber random laser
ESA	Electrical spectrum analyzer
FBG	Fiber Bragg grating
FFT	Fast Fourier transform
FP	Fabry-Perot
FPI	Fabry-Perot interference
FRM	Faraday rotator mirror
fs	Femtosecond
FWHM	Full width at half maximum

LPG	Long period grating
LUT	Laser under test
MZI	Mach-Zehnder interference/interferometer
OC	Optical fiber coupler
OSA	Optical spectrum analyzer
PC	Polarization controller
PD	Photodetector
PMF	Polarization-maintaining fiber
PSD	Power spectral density
PS-FBG	Phase-shifted fiber Bragg grating
PZT	Lead zirconate titanate
RIN	Relative intensity noise
SBS	Stimulated Brillouin scattering
SMF	Single mode fiber
SNR	Signal-to-noise ratio
SOP	State of polarization
SRS	Stimulated Raman scattering
TDS	Time delay signature
WDM	Wavelength-division-multiplexing

Chapter 1 Introduction

Over the past several decades, fiber-optic techniques have attracted intense attention and successfully found diverse applications including highly-sensitive optical fiber sensors, fiber lasers, high speed long distance optical communication systems, optical imaging and so on. This thesis aims to focus on a novel fiber random grating fabricated by the advanced femtosecond (fs) laser micromachining technique and characterizing the unique optical properties of the fiber random grating. It is for the first time that such an innovative fiber grating device could play important roles in a variety of photonic research areas and contribute to novel discoveries and advancements in fiber-optic sensing, random fiber lasers, and chaotic laser systems.

This chapter generally introduces the background, motivation, and contribution of the research work. In Section 1.1, a brief introduction of the fs laser micromachining technique for fiber grating fabrication, random lasers, and chaotic lasers is presented. Motivations on developing novel fiber-optic sensors, random fiber lasers and chaotic semiconductor lasers using the proposed fiber random grating are also clarified. Section 1.2 summarizes the contributions of our work to the above three areas. Section 1.3 gives the outline of the thesis.

1.1 Background and motivation

1.1.1 Femtosecond laser micromachining and fiber Bragg grating fabricated by fs laser

Femtosecond (fs) laser micromachining has been a useful technique either to modify and remove materials or to change the properties of a material, and can be applied to transparent

and absorptive substances. With the first demonstration in 1994 that micrometer-sized features were ablated by the fs laser on silica and silver surfaces [1, 2], this technology has rapidly advanced with an improved resolution of ablation in nanometer scale in less than ten years [3, 4]. The advantages of using fs laser micromachining technique include the spatially confined changes to the focal volume for manufacturing complex three dimension structures, independence of the material of the absorption process, and capability of fabricating interconnects in a single substrate separately [5]. The optical breakdown process induced by the fs laser pulses transfers the optical energy to the material, ionizing a large number of electrons, which in turn transfers energy to the lattice. The absorption of light in the transparent material is usually a nonlinear process as electronic transitions at the energy of the incident photon are not allowed. In order to trigger the nonlinear absorption, the electric field strength in the fs laser pulse must be approximately equal to the electric field that binds the valence electrons in the atoms as shown in Figure 1-1. When fs laser pulse with high peak power is focused into a material, in the absence of impurities, carriers will be generated by multiphoton absorption, exciting electrons from the valence to the conduction band. The nonlinear absorption process occurs with high probability as long as several photons are incident on an electron at the same time. Depending on the energy level of the fs pulses, the pulse duration and the focusing numerical aperture, different degrees of excitation would be expected with reversible modification, cracking, void formation or even localized melting occurring in the irradiated materials.

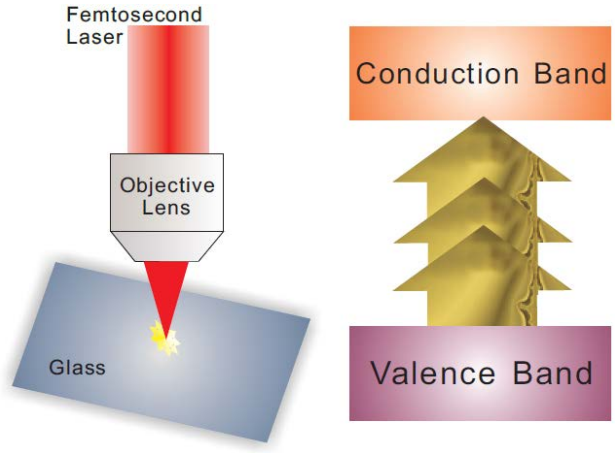

Figure 1-1. Schematic of the fs laser incident on glass and diagram of the excitation of electrons to the conduction band.

Recently ultrahigh-power fs laser radiation has drawn intensive attention for the induction of refractive index change in dielectric materials to fabricate waveguide structures [6]. One typical example of the fs laser radiation modified waveguides for optical fibers is the fiber Bragg grating (FBG), which is classified into two major categories, Type I-IR and Type II-IR gratings depending on their resistances to high-temperature annealing. The fs laser induced refractive index changes in bulk silica in the two regimes resemble that induced by the Type I and II FBG fabricated by the UV light [7]. The refractive index variations in Type I-IR FBG originates from modifications below the damage threshold of the fiber material, while Type II-IR FBG is often made with higher fs pulse power and the induced permanent index change is a result of multiphoton and avalanche ionization induced plasma formation. Each type of FBG can usually be produced (i) by irradiating a section of fiber simultaneously through a phase mask or (ii) by inducing index changes along the fiber in a sequential fashion through point-by-point, line-by-line or plane-by-plane and continuous writing techniques. The first successful demonstration for FBG fabrication using phase mask approach with fs radiation was in 2003 [8]. A specialty phase mask was precision etched to maximize coupling of the

incident fs laser radiation into the ±1 orders. The phase mask automatically matched path lengths of the generated orders when aligned at normal incidence to the inscription beam to within the dimensions of the spatial envelop of the fs pulses. The generated sinusoidal interference field leads to a non-sinusoidal modulated FBG in the fiber due to nonlinearity, giving rise to higher order Bragg resonances. In the point-by-point technique (line-by-line or plane-by-plane), single pulses from the fs laser are focused within the fiber core region using a powerful microscope objective. The highly localized refractive index changes induced by each pulse act as FBG planes, which are created in a one-by-one and repeat fashion by translating the beam with high-resolution translation stages [9]. Depending on the pulse intensities of the fs laser, FBG fabricated using this method has similar thermal properties to the gratings written with the fs laser and the phase mask. Figure 1-2 shows the schematic of a regular uniform FBG and its transmission and reflection spectrum. FBGs inscribed by fs laser have been increasingly used in sensing applications especially involving system monitoring in extreme high temperature environments and other applications such as optical communication systems and fiber lasers.

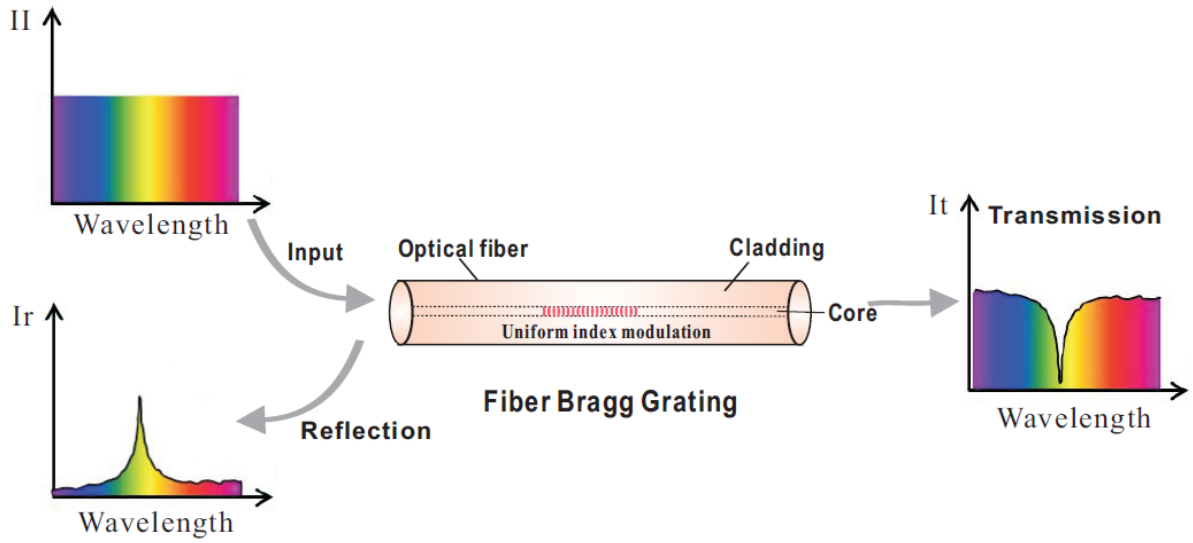

Figure 1-2. Schematic of a regular uniform FBG and its transmission and reflection spectra.

As a periodic modulation of the refractive index along a length of optical fiber results in the FBG which acts as a band-rejection optical filter and passes all wavelengths of light not in resonance with it, our motivation for fabricating the fiber random grating using the fs laser micromachining technique arises from the curiosity that what would the optical properties of a fiber random grating with randomly spaced refractive index modulations on one hand. On the other hand, it is more strongly desired to design and fabricate a compact fiber-based random medium to provide random distributed feedback for random fiber lasers as well as to explore and exploit the advantages and benefits brought to the random laser area by the fiber random grating.

1.1.2 Random lasers

With the invention of the laser in the late 1950s, a prosperous and continuous development of novel photonic devices and advanced optical engineering techniques has been on the way, which has a wide impact across many traditional and cutting-edge sectors of the world economy. Conventional lasers are mainly comprised of a resonant cavity with a gain medium for amplification inside. The resonant cavity provides positive feedback to the light trapped inside and the gain medium amplifies the feedback light. The lasing occurs when the gain in the cavity overcomes the total loss. Normally the material of the gain medium determines the scale of the photon amplification and the lasing wavelengths. The resonant cavity introduces cavity modes to the laser, which define the exact generated lasing frequency and determine the spatial structure of the output beam.

The initial discovery of random lasing was firstly conducted by Letokhov in 1966, when he was studying the interstellar radiation and found that the non-resonant feedback would lead to lasing at the frequency of the maximum gain [10, 11]. After three decades, the term

random lasers was coined by Wiersma *et al.* [12], based on the novel phenomenon of phase-coherent multiple scattering in the lasing action. Unlike conventional lasers, there is no traditional cavity in the random lasers, where the generated lasing light is mainly determined by multiple scattering of photons in the gain medium. The random multiple scattering of the photons further defines the properties of the random laser, such as the spectral and spatial mode structure, directionality/divergence, polarization, and output power. Therefore, the gain materials are important in random lasers. Up to now, various disordered materials have been utilized as the random laser gain media, including powders, granular materials, plastics, polymers, dye materials, porous glasses and so on.

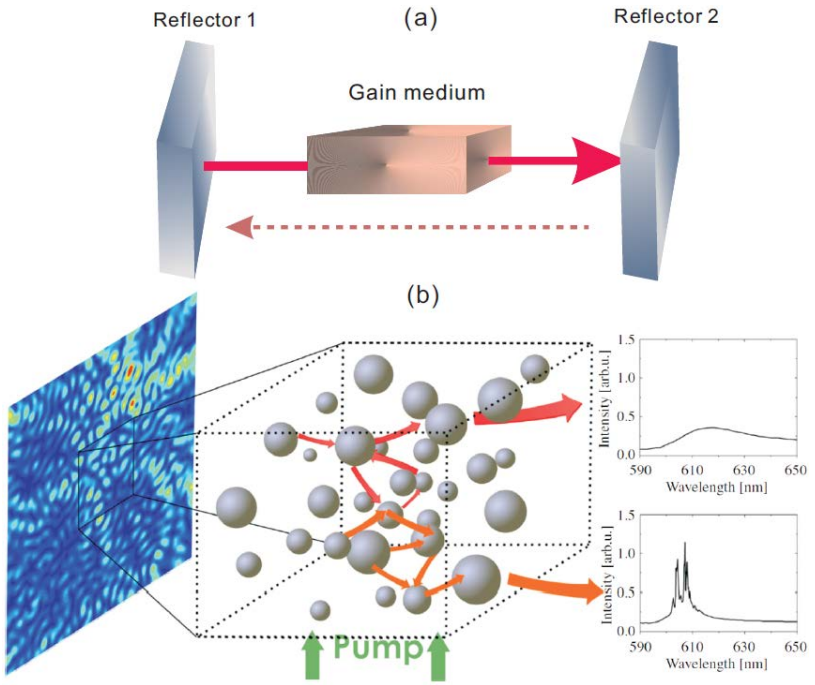

Figure 1-3. Schematics of (a) conventional Fabry-perot resonator and (b) random lasing in a disordered medium [13].

The difference between the conventional cavity-based lasers and random lasers could be clarified in more details as shown in Figure 1-3. In conventional cavity-based lasers, two key elements are required: a gain medium that provides amplification and an optical cavity that

traps the light inside by creating positive feedback. As shown in Figure 1-3(a), a conventional Fabry-Perot (FP) resonator consists of a gain medium sandwiched by two reflecting mirrors. In order to generate lasing, the gain in the cavity should overcome the total loss of the resonator, i.e. $R_1R_2\exp(2GL)$ should be met. Here R_1 and R_2 are the reflection ratios of the two reflectors, G is the gain provided by the gain medium, and L is the cavity length. In such a cavity, the coherent interference among lights with different round trip times lead to lasing at longitudinal mode frequencies with $v_N = Nc/(2Ln)$, where N is the order of the longitudinal mode, c is the speed of light in vacuum, n is the refractive index in the cavity. If no filtering mechanism is employed, multiple longitudinal mode lasing is expected and radio-frequency inter-mode beatings could be observed by an electrical spectrum analyzer.

In random lasers as shown in Figure 1-3(b), light no longer travels along multiple round trip paths determined by the two fixed reflectors as in the conventional laser cavity, but rather wanders in the disordered gain medium along complicated paths. Two criteria are usually used to define a random laser: (i) light is multiply scattered in the randomly disordered gain medium and amplified by the stimulated emission, and (ii) there is a threshold above which the total gain is larger than the loss. During the multiple-scattering process, there are two characteristic length scales for photons that are trapped in the random medium, which could be used to characterize the random lasing behavior. One is the generation length, which is the average distance a photon travels before generating a second photon through the stimulated emission. The other one is the mean path length, which is the distance a photon travels in the gain medium before escaping. When the generation length is smaller than the mean path length, every photon that travels inside the gain medium will generate another photon before it leaves the medium, which will trigger a chain reaction and

lead to lasing action. Note that stronger scattering will result in longer mean path length and higher probability for generating more photons through the interaction with the gain medium. Thus the case when the generation length is equal to the mean path length determines the threshold for the random lasing. The multiple-scattering process in random lasers defines spectral and spatial optical modes with a certain frequency and bandwidth and a complex spatial profile. In some sense, random lasers are mirror-less but not mode-less. In terms of types of feedback, random lasers could be categorized into two kinds, one with non-resonant feedback and the other one with resonant feedback. The non-resonant feedback in random lasers was firstly introduced by Ambartsumyan *et al*. in 1966 [14, 15]. They replaced one of the cavity reflectors in the conventional lasers with a highly scattering bulk medium. In this situation, the phase information of the photons was assumed lost due to numerous random scattering in the disordered medium. Thus light from different multiple-scattering paths cannot be coherently superimposed with each. As a result, the laser generation consists of a large number of broad and overlapping low-Q modes, which prevents the formation of distinct spatial optical modes. Such a non-resonant feedback imposes no spectral selectivity on the lasing output and is thought to be frequency independent. The generated random lasing spectrum is often featured with broad spectral width and centered on the frequency where the gain is maximum. It has been demonstrated that random lasers with non-resonant feedback also shows some similar properties as the key features of conventional lasers, such as spectrum narrowing, existence of the relaxation oscillation, and threshold behavior of the output lasing power [16, 17]. Different from the non-resonant feedback, random lasers with resonant feedback were also discovered by H. Cao in 1998, where coherent lasing was observed using ZnO powder and polycrystalline films [18, 19]. In this case, light after multiple scatterings can be coherently overlapped, which leads to interference effects in the

feedback. Such a resonant feedback contributes to the narrow lasing spikes on top of the gain profile, whose positions are randomly distributed over the spectrum. After these initial efforts, research has been focused on investigating and developing random lasers operating in different gain and scattering mediums. A tremendous number of novel random lasers has been reported so far, such as random lasers based on direct bandgap semiconductors [20], dye and polymer based random lasers [17, 21], plasmonic-enhanced random lasers [22], rare-earth doped powder based random lasers [23], random microchip lasers [24], biological tissue based random lasers [25] and so on.

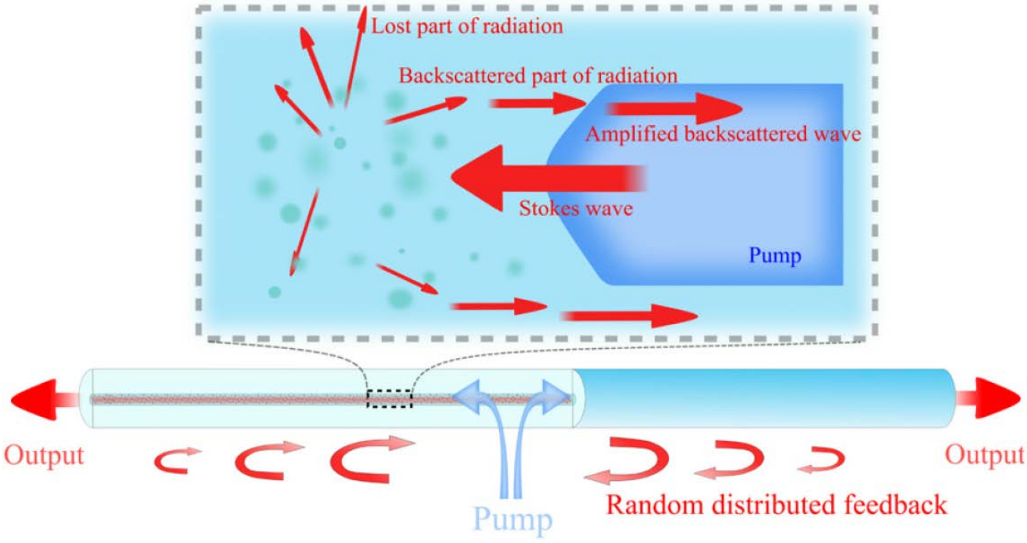

Figure 1-4. Schematic of Rayleigh scattering based random fiber laser [26].

However, there are still a number of technical and fundamental issues that make the utilization of random lasers challenging. Due to the three dimensional disordered materials and random multiple-scatterings, traditional random lasers often suffer from drawbacks of low contrast of lasing peaks, high lasing threshold values, lack of directionality, and random oscillations at multiple wavelengths. To overcome some of these drawbacks, random lasing occurring in optical fibers have been proposed and investigated intensively. In a single mode fiber (SMF), light is confined in a transverse direction and propagates as the fundamental

transverse mode in the fiber. Consequently, SMF could be regarded as a one-dimensional waveguide for random fiber lasers and only the longitudinal variations of the waveguide would impose influence on the lasing dynamics. The intrinsic disorder in the silica fibers originates from the sub-micron scale inhomogeneity in the refractive index along the fiber axis due to the fiber manufacturing process. This inhomogeneity induces the well-known Rayleigh scattering in the optical fiber as shown in Figure 1-4, which is very small and only corresponds to 5×10^{-5} km^{-1} of the input light. Rayleigh scattering is an elastic scattering process and in optical fibers it scatters light with random strengths and at random positions over the fiber length. If external disturbances are isolated from the optical fiber, this scattering process will remain unchanged in time and the density fluctuations in the fiber core are regarded to be frozen and static. Despite the small values of the Rayleigh scattering feedback, random lasing could still be triggered as long as high gain is initiated in the silica fiber and a long enough fiber is used to provide stronger feedback. The first effort to achieve random fiber laser using Rayleigh scattering is reported in 2010 [27], where an 83km long conventional telecom fiber acted as the Raman gain medium and provider of Rayleigh scattering feedback at the same time. A relative low-threshold, efficient, narrowband continuous wave (CW) lasing output was realized. Later on, a large number of random fiber lasers have been proposed and demonstrated by varying the fiber type, fiber based gain medium, gain mechanism in optical fibers and so on.

Our motivation for linking the fiber random grating and random fiber lasers is based on the aim for replacing the long optical fiber providing random distributed feedback with a short counterpart, which would improve the random fiber laser system in terms of laser noise and compactness. As most of the previously reported random fiber lasers are based on the Rayleigh distributed feedback from a relatively long fiber length (>1km), the long open

cavity formed by the long fiber naturally introduces large numbers of cavity modes to the laser, which would lead to intensified noise in the performance of the random fiber laser when external disturbances are not completely eliminated. By shortening the length of the random distributed feedback fiber and meanwhile enhancing the Rayleigh scattering with the inscription of random grating, a more compact random fiber laser with mitigated mode competition and mode hopping is expected. Other aspects concerning the properties of the random fiber lasers based on fiber random grating such as linewidth characterization, intensity and frequency noise measurement, lasing threshold, and the applications of the proposed lasers also give rise to our motivations for this research.

1.1.3 Chaotic semiconductor lasers

Lasing action in semiconductors was firstly reported in 1962. The device used consisted of a forward-biased GaAs p-n junction. The optical gain was provided by the electron-hole recombination in the depletion region of the p-n junction and the optical feedback was provided by the polished facets perpendicular to the junction plane, which forms a resonant cavity. Later works have developed semiconductor lasers at different wavelengths by employing p-n junctions of different direct-band-gap semiconductor materials. Up to now, semiconductor lasers have found numerous applications, including imaging, sensing, fiber-optic communications and spectroscopy.

Most practical semiconductor lasers operate with a constant output power or pulsing dynamics. However, it was also discovered that semiconductor lasers are able to emit chaotically if they are perturbed with increased number of dynamic dimensions. As usually the dynamics of semiconductor lasers is described using rate equations for the electric field and carrier inversion, which is a second-order nonlinear system yielding a driven damped

nonlinear oscillator, i.e. relaxation oscillations. This feature makes the semiconductor laser very sensitive to the external optical perturbations. The induced anti-guidance effect detunes the emission frequency of the semiconductor lasers from the gain spectrum peak, which results in refractive index variation with carrier density, leading to spectral broadening and lasing instabilities [28-30].

Many configurations have been proposed to overcome the damped relaxation oscillations in semiconductor lasers and to generate laser chaos. One of the effective methods is returning a small fraction of the laser emission in the laser cavity by using external feedback [31]. The chaotic dynamics of the perturbed semiconductor laser is determined by the competition between the laser's intrinsic relaxation oscillation and the introduced external cavity modes. When the frequency of the external cavity mode is much smaller than that of the intrinsic relaxation oscillation, such low frequency modulations will induce low frequency power fluctuation and coherence collapse dynamics [32, 33], which is attributed by the inclusion of higher dimensions of nonlinearities. It has been demonstrated that feedback provided in different ways, such as single mirror, double mirrors, phase-conjugate mirror, FP etalon, diffraction grating, polarizer and so on, is able to disturb the semiconductor lasers with chaotic output.

Chaotic lasers have been widely applied and utilized in the chaos communications, where synchronized chaotic lasers are used to perform digital communications and improve encryption security [34]. Random number generation is one of the important applications of the chaotic lasers in the chaos communication. Chaotic semiconductor lasers provide ideal physical source of random bits, which possesses outcome unpredictability and no dependence on any previous outcome. The currently achieved random bit generation rates have reached several gigahertz bit per second by directly employing the output of the chaotic

semiconductor laser [35] and hundreds of gigahertz bit per second by using signal post-processing methods, such as derivative calculations of the chaotic signal, multi-bit extraction [36, 37]. Other applications of chaotic lasers include chaotic optical sensing [38, 39], optical logic [40], and chaos computing [41].

Our motivation for applying the fiber random grating in the generation of the laser diode chaotic output is to investigate the dynamics of the semiconductor laser when it is subjected to the random distributed external feedback, which has never been studied or researched. Moreover, there are expectations that the random distributed feedback provided by the fiber random grating can effectively suppress the TDS in the chaotic semiconductor laser output, which is quite frequently encountered in the chaotic lasers induced by the external feedback.

1.2 Thesis contribution

This thesis has investigated the optical properties of a novel fiber random grating fabricated by fs laser micromachining technique and extended the applications of the fiber random grating from optical sensing to random fiber lasers and chaotic semiconductor laser based random bit generations. Major contributions of this thesis include:

Firstly, we conceived the novel idea of fabricating the fiber random grating using fs laser micromachining technique and introduced the manufacturing procedures in detail. Initial investigations revealed that the randomly varying spaced plane-by-plane writing technique brings novel physical properties to the fiber random grating, such as multiple-interfering reflection spectrum and induced random birefringence along the sample fiber. Based on the multiple interference feature of the fiber random grating, a novel multi-parameter fiber-optic sensor is proposed and demonstrated to realize simultaneous measurement of temperature, axial strain, and surrounding refractive index thanks to the extended index modification in

the fiber cladding layer. A wavelength-division spectral cross-correlation algorithm is adopted to extract the phase variation induced spectral shift responding to different external disturbances. Sensitivities of 10.32 pm/°C, 1.24 pm/με, and −1520.6 pm/RIU were achieved for temperature, axial strain, and surrounding refractive index, respectively. The developed sensor can be potentially applicable in areas of engineering, biomedical, biological, and environmental sensing with its robust physical strength and high sensitivities.

Secondly, novel BRFLs are proposed and demonstrated. The first work in this area proposed a novel BRFL based on a bi-directionally pumping scheme through the SBS in a 10-km-long optical fiber. Theoretical analysis predicts a random fiber FP resonator is built up through the pump depletion effects of SBS at both ends of the fiber with capability of narrow-linewidth lasing emission. The linewidth of the BRFL is measured to be ~860Hz, which can be successfully applied for linewidth characterization beyond 860 Hz of light source under test. Then the random grating-based FP resonator is introduced to build up another novel BRFL. Significantly enhanced random feedback from the fiber random grating overwhelms the Rayleigh backscattering from the standard single mode fiber, leading to efficient Brillouin gain for the lasing modes and reduced lasing threshold. The intensity and frequency noises of the proposed random laser are effectively suppressed due to the reduced resonating modes and mode competition resulting from the random grating-formed filters compared to those of the Rayleigh feedback resonator in single mode fibers. The linewidth of the coherent random lasing spike is measured to be ~45.8 Hz using the heterodyne technique. The proposed narrow-linewidth BRFL will pave the way for applications in high-resolution spectrometers, coherent light sources, and optical sensing.

Thirdly, novel EDFRLs are designed and demonstrated for optical sensing applications. The random feedback from the fiber random grating plays an important role in improving the

physical properties of the random fiber lasers and exploiting novel applications based on random fiber lasers. In the fiber random grating based EDFRLs, numerous polarization-dependent spectral filters are formed in the fiber random grating and they are superimposed to provide multiple lasing lines with high SNR up to 40dB, which gives an access for a high-fidelity multiple-static-parameter sensing scheme. The number of sensing parameters can be controlled by the number of the lasing lines via input polarizations and wavelength shifts of each peak can be explored for the simultaneous multi-parameter sensing with one sensing probe. The proposed random laser sensor has achieved simultaneous temperature and axial strain measurements with maximum errors of 2.3^{o}C and 15.2με, respectively. In addition, the random grating induced coupling between core and cladding modes can be potentially used for liquid medical sample sensing in medical diagnostics, biology and remote sensing in hostile environments. The fiber random grating based EDFRL is also able to detect the ultrasound waves. With a single mode lasing scenario, this random laser sensor offers linear and pure temporal responses to the broadband ultrasonic acoustic emission from 20kHz to 0.8MHz. The multiple-interfering reflection spectrum of the random grating provides large number of steep peak areas over a broad spectral range, which significantly enhances the sensitivity of the random laser sensor and makes it an ideal sensor in harsh environment with large temperature or strain variations. The proposed laser sensor offers SNR improvement up to 20dB and higher sensitivity compared with conventional piezoelectric acoustic sensors. It is believed that the proposed laser sensor is a truly practical ultrasonic sensor and would find important applications in many ultrasound-related areas, such as structural health monitoring, geophysical exploration, material testing, and biomedicine.

Finally, we demonstrate that the distributed feedback from a fiber random grating can perturb a semiconductor laser into chaotic emission without the TDS. A theoretical model is

developed by modifying the Lang-Kobayashi model in order to numerically explore the chaotic dynamics of the laser diode subjected to the random distributed feedback. It is predicted that the random distributed feedback is superior to the single reflection feedback in suppressing the TDS. In experiments, a massive number of feedbacks with randomly varied time delays induced by a fiber random grating introduce large numbers of external cavity modes into the semiconductor laser, leading to the high dimension of chaotic dynamics and thus the concealment of the TDS. The obtained TDS with the maximum suppression is 0.0088, which is the smallest to date. This effective and simple approach is easily applicable in the concealment of the encryption system parameters and could hence improve the security in optical chaos based communications.

1.3 Thesis outline

This thesis contains nine chapters and is organized as follows:

Chapter 1 reviews the background of the fs laser micromachining technique and fs laser fabricated FBG, random lasers, and chaotic semiconductor lasers. Thesis contribution and outline are also given in this chapter.

Chapter 2 presents the fabrication procedure of the fiber random grating by fs IR laser micromachining technique and the optical properties of the fiber random grating. A novel multi-parameter point fiber-optic sensor based on fiber random grating is proposed and demonstrated to realize simultaneous measurement of temperature, axial strain, and surrounding refractive index.

Chapter 3 reviews various random fiber lasers employing different gain mechanisms, including Raman gain, Brillouin gain, and Erbium-doped fiber gain. Different configurations for random fiber lasers are presented and compared. The properties of random fiber lasers,

including linewidth characterization, lasing mode, intensity and frequency noise are discussed and summarized.

Chapter 4 investigates the physics and presents experimental results of a novel BRFL based on the bi-directionally pumped SBS in a 10-km-long optical fiber.

Chapter 5 investigates the physics and presents experimental results of a novel BRFL with the fiber random grating based FP resonator. The linewidth, threshold, intensity and frequency noise of the proposed random laser are measured and displayed.

Chapter 6 proposes a fiber random grating based EDFRL sensor for multiple static parameters measurement. The lasing characteristics is investigated and demonstrated through theoretical modeling and experiments. Simultaneous measurement for temperature and strain is performed and the measurement error is analyzed and calculated.

Chapter 7 proposes a fiber random grating based EDFRL sensor for ultrasound detection. By utilizing the multiple-interfering reflection spectrum of the fiber random grating, ultrasound signals with frequencies from 20kHz to 0.8MHz could be detected with high sensitivity.

Chapter 8 studies and investigates the suppression of the TDS of the chaotic output of a semiconductor laser subjected to the random distributed feedback from the fiber random grating. Theoretical modeling and experimental results are presented, demonstrating the effectiveness of the fiber random grating feedback for the TDS suppression.

Chapter 9 concludes all the work in this thesis and proposes possible directions for future research.

Chapter 2 Fiber random grating and its application in fiber-optic sensing

This chapter presents the fabrication and optical properties of fiber random grating using femtosecond (fs) laser micromachining technique. A novel multi-parameter fiber-optic sensor based on the fabricated fiber random grating is proposed and demonstrated to realize simultaneous measurement of temperature, axial strain, and surrounding refractive index. We proposed a wavelength-division spectral cross-correlation algorithm to extract the phase variation induced spectral shift responding to different external disturbances. Sensitivities of 10.32 pm/°C, 1.24 pm/με, and −1520.6 pm/RIU were achieved for temperature, axial strain, and surrounding refractive index, respectively. Section 2.1 gives the background of the previously reported fiber random gratings. Section 2.2 introduces the fabrication of the novel fiber random grating. Section 2.3 shows the optical properties of the fiber random grating through both theoretical modeling and experiments. Section 2.4 describes the optical sensing application of fiber random grating. Section 2.5 draws the final conclusion.

2.1 Background

There has been a long history of studying the influence of the noise in the fabrication system on the quality of fabricated fiber Bragg gratings (FBGs). Conventional FBGs are manufactured by periodically modulating the refractive index of an optical fiber along the fiber axis. Noise induced in the fabrication process is usually considered an undesirable factor that could disrupt the periodicity of the refractive index modulation, and thus it makes

detrimental impacts on the optical properties of the fabricated FBG. Previously, the influence of random phase and index errors on FBGs have been studied in [42], where the effects of the excess crosstalk induced in apodized gratings used in wavelength-division-multiplexing (WDM) systems and the time delay fluctuations in chirped gratings are analyzed. Other related studies include the grating reconstruction from noisy reflection data via inverse scattering method [43, 44]. However, these works mainly focus on elimination of the noise impacts. It was not shown until recently that the noise could play a positive role in fabricating fiber gratings either for improving their spectral responses with better filtering effect or for novel applications in random fiber lasers. Such gratings fabricated with random phases and refractive indexes as well as wavelength-scale periods are called random FBG.

In 2008, Derevyanko theoretically proposed a method utilizing some specific distributions of noise in the reflection coefficient inside the bandgap as well as the distribution of time delays of the grating to realize the flat-top random FBG [45]. The simulation results predict that the averaged spectrum is flat within the bandgap of the fabricated random FBG and the sidelobes are significantly suppressed compared to the regular uniform gratings. Later work further investigated the impacts of different statistics of noise in the refractive index modification on the properties of the random FBG [46]. Random FBGs with top-hat spectral response have also been successfully fabricated with noisy modulation in the refractive index and other pseudo-random designs. Such a top-hat random FBG has important applications in WDM networks, optical switching, and high power fiber lasers. Another group of random FBG was proposed by Kashyap in 2009 for providing random distributed feedback for random fiber lasers, where a long FBG fabrication technique was employed by insertion of a large number of randomly distributed phase errors in the grating structure [47]. The fabrication technique was based on a push/pull phase shifting interferometry [48]. As the

fiber was held by a vacuum v-groove mount, irregularities in the grating spectrum were induced by the friction between the fiber and the mount. The fabricated random FBG could be regarded as a superposition of a large number of short length gratings with different lengths and random phase shifts between them. The resultant reflection spectrum showed a combination of a conventional profile of the regular FBG and many random spectral spikes. The novel random FBG exhibits a typical light localization behavior which is beneficial for the build-up of random fiber lasers. A continuous work later proposed another alternative method for fabricating high-quality ultra-long random FBGs [49]. A piezomounted phase mask placed on a conventional Talbot interferometer was used to generate a moving fringe pattern. Random phase shifts could be added to the inscription process by applying a random DC bias on the ramp signal that controls the piezomounted phase mask to be synchronized with the moving fiber. One-meter long random FBG was obtained by introducing a large number of random phase shifts following the Poisson distribution, which was then used as a random coherent feedback medium in a Raman random fiber laser [50].

However, these previously reported random FBGs do not possess truly random spectral responses. Random FBGs with top-hat reflection spectrum are obviously a perfect spectral filter for single wavelength, which is not suitable for random fiber laser applications. While random FBGs proposed by Kashyap, although showing some improvements in the spectral randomness as multiple resonant spikes are observed on top of the reflection spectrum envelope, still somehow have a dominant peak envelope at a single wavelength, which could not be regarded as an ideal random medium for random fiber lasers. To optimize the spectral randomness of the random FBGs, we will show in the next section that a completely novel technique and design will be adopted for the fabrication of fiber random gratings.

2.2 Fabrication of fiber random grating

The fiber random grating we proposed was fabricated employing the direct writing method, i.e. plane-by-plane writing technique. The plane-by-plane writing technique uses single pulses from the fs laser that are focused within the core region of the fiber using a powerful microscope objective. Each pulse makes highly localized changes to the refractive index that act as FBG planes. Planes are created sequentially in a step and repeat fashion by translating the beam using high-resolution mechanical translation stages. Depending on the pulse intensities, the resulting grating structures could be fabricated with thermal stability either similar to Type-I grating or Type-II grating.

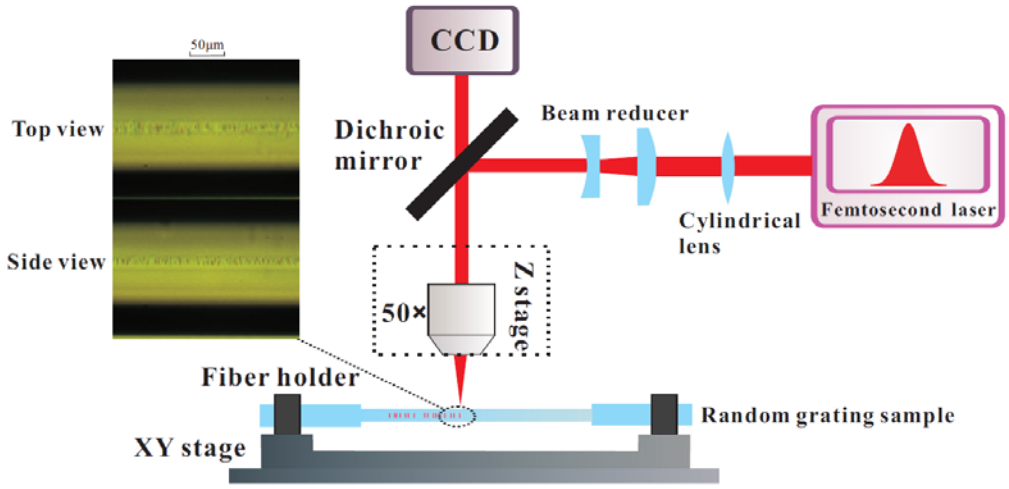

Figure 2-1. Experimental setup of the plane-by-plane fs laser micromachining system with microscopic images of the fiber random grating sample.

For the inscription of the fiber random gratings, a fs Ti:sapphire regenerative amplifier (Spitfire, Coherent) operating at a wavelength of 800 nm with a repetition rate of 100 Hz and a pulse duration of 80 fs was used in the experiments as shown schematically in Figure 2-1. A beam reducer consisting of one plano-convex lens and one plano-concave lens was used to reduce the beam width to match the open aperture of the objective (50×/0.6, Nikon). The

dichroic mirror was used to guide the laser beam into the objective which was fixed on a translation stage driven by a piezo positioning system, this allows Z-direction focusing and random dithering along the fiber axis with a maximum displacement of 2.5 μm. A standard single-mode fiber (Corning SMF-28) was clamped at two ends by a fiber holder that is mounted on an air-bear stage with ±10 nm position accuracy, moving along the fiber axis with a speed of 100 μm/s. A charge coupled device (CCD) camera after the dichroic mirror was used to monitor the fiber alignment and the micro-machining process during the fabrication of the optical fiber random gratings.

In order to increase the volume of the index change in the fiber core for higher mode coupling efficiency, a cylindrical lens with focal length of 1 meter was placed at a distance of ~94 cm in front of the objective so that the focal points of the cylindrical lens and the objective overlap at the same spot. A grating plane normal to the fiber axis of induced index change with a diameter of ~10 μm and a thickness of sub-micron across the fiber core was produced by a single pulse with the combination of the cylindrical lens and the objective. The optical images of the fiber random grating sample are shown in the inset of Figure 2-1. The index modification was processed spot by spot with random variations of the spot spacing between 0 μm and 3.5 μm with a pulse energy of 1.0 μJ. The spacing randomness was predetermined by the random number generated by a computer and stored for repeatable uses afterwards. Around 50000 index modification planes were made along the 10 cm long fiber sample. Note that the coating layer was removed before executing index modification along the optical fiber and part of input light in the fiber core can be coupled to the cladding because the laser induced index change is not uniform across the fiber, which allows for the enhanced sensor sensitivities especially for refractive index measurement.

2.3 Optical properties of fiber random grating

To investigate the optical properties of the fiber random grating, we built up the experimental setup for monitoring the fiber random grating spectra as shown in Figure 2-2. A broadband light source (NKT Photonics) ranging from 1400nm to 1600nm was used and launched to the input port 1 of the circulator. The optical fiber random grating was mounted on two micro-stages. One end of the random grating was connected to port 2 of the circulator, while the other end was cut with non-perpendicular cleave. The reflected light spectrum comprising 50000 data points was collected by an Optical Spectrum Analyzer (OSA) with a wavelength resolution of 20 pm through port 3 of the circulator. The inset spectrum shows an example of the reflection (blue) and transmission (red) spectra of the random grating. The incident light would be divided into two parts when refracted by the random grating planes, one of which is coupled into the cladding region being transmitted or reflected in the form of cladding modes due to the non-uniform index modification induced by fs laser across the fiber while the other one remains being transmitted or reflected as core mode. It is illustrated that only a small proportion of the incident light is reflected backward at the spots with localized changes in the refractive indices. High attenuation in transmission spectrum is due to the significant refraction loss and absorption loss at the non-uniform index modification regions. It is also noted that an interference pattern is hardly observed in the transmission spectrum as the energies of the transmitted cladding modes are relatively small compared to that of the transmitted core mode, leading to a minimum visibility in the transmitted interference spectrum.

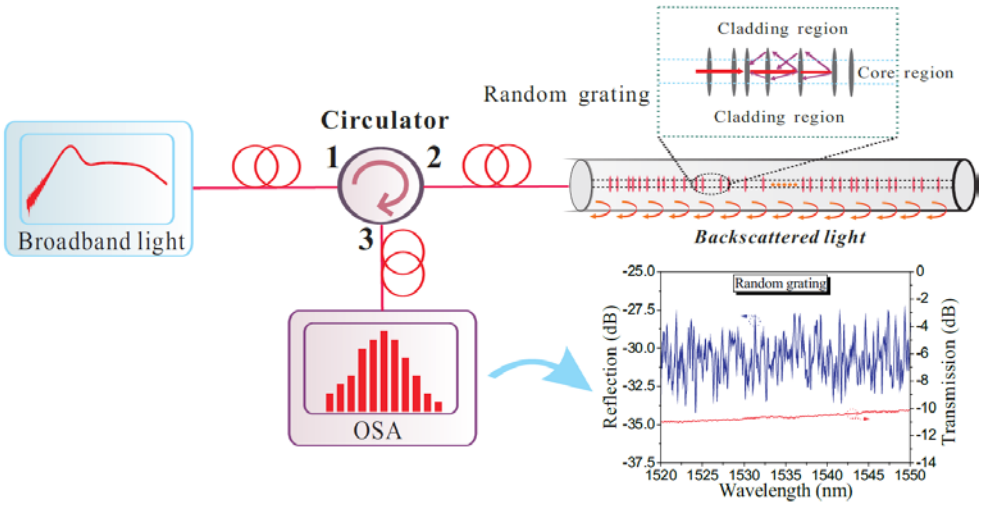

Figure 2-2. Experimental setup for monitoring the reflection and transmission spectra of random grating.

The distinct interference fringes exhibited in the reflection spectrum are the result of both a Mach-Zehnder interference (MZI) scheme via core-cladding mode coupling and a Fabry-Perot interference (FPI) scheme via multiply reflected core-core mode coupling. In the MZI scheme, numerous pairs of the index modified spots act as light steering elements to pilot split-merge propagation of the backscattered fundamental core mode and cladding modes along the random grating region, leading to the normal core-cladding coupling effect. The FPI scheme is formed by the coupling among the core modes that are multiply reflected inside the FPI sub-cavities comprised by any two spots. To establish the theoretical model of the random grating, it is assumed that the FPI scheme is mainly contributed by the core mode that is reflected only once from the index modified spots as energies of reflected core modes after multiple reflections are significantly attenuated, which are too weak to account for the reflection interference pattern. Thus the FPI scheme is simplified to the case with only one round trip. Given that the optical fiber random gratings are fabricated with a random variation of spacing between neighbouring index modified spots along the grating length,

each MZI or FPI formed by any two spots possesses a unique interference pattern. Therefore the irregular reflection spectrum is expected as a result of the superposition of the numerous MZIs and FPIs. The interference field of the reflected light from the random grating could be expressed as

$$\vec{E}_r = \vec{E}_r^{core} + \vec{E}_{r,c}^{clad} = E_0\left(\sum_{k=1}^{M} e^{-\alpha L_k} r_k^{core} e^{i\varphi_k^{core}} + \bar{c}\sum_{k=1}^{M} e^{-\alpha L_k} r_k^{clad} e^{i\varphi_k^{clad}}\right) \tag{2.1}$$

where E_r^{core} and $E_{r,c}^{clad}$ are the total electrical fields of the reflected core mode and coupled-back cladding modes, respectively, E_0 is the input electric field, α is the averaged attenuation of the unit-length random grating, L_k is the fiber length at kth spot, r_k^{core} and r_k^{clad} are the reflection coefficients of the core mode and cladding modes at the kth spot, φ_k^{core} and φ_k^{clad} are the phase of core mode and cladding modes at the kth spot, c is the averaged coupling-back coefficient for the cladding modes, M is the total number of the inscription spots. The intensity of the interference pattern is obtained by multiplying the above reflected light field with the conjugate of itself:

$$\begin{aligned} I_r = I_0[&\sum_{k=1}^{M}\sum_{k'=1}^{M} e^{-\alpha(L_k+L_{k'})} r_k^{core} r_{k'}^{core} e^{i(\varphi_k^{core}-\varphi_{k'}^{core})} \\ &+ 2\bar{c}\sum_{k=1}^{M}\sum_{k'=1}^{M} e^{-\alpha(L_k+L_{k'})} r_k^{core} r_{k'}^{clad} \cos(\varphi_k^{core}-\varphi_{k'}^{clad}) \\ &+ \bar{c}^2\sum_{k=1}^{M}\sum_{k'=1}^{M} e^{-\alpha(L_k+L_{k'})} r_k^{clad} r_{k'}^{clad} e^{i(\varphi_k^{clad}-\varphi_{k'}^{clad})}] \end{aligned} \tag{2.2}$$

The first term in the above equation gives the core-core mode coupling, the second term gives the core-cladding mode coupling and the third term could be neglected due to the weak energy of cladding modes. The phase differences in either core-core mode coupling case or core-cladding mode coupling case are easily extracted for a single FPI and a single MZI using Eq. (2.2),

$$\Delta\varphi_{core-core} = \varphi_{core} - \varphi'_{core} = \frac{4\pi l'}{\lambda} n_{core} \tag{2.3}$$

$$\Delta\varphi_{core-clad} = \varphi_{core} - \varphi_{clad} = \frac{2\pi l}{\lambda}(n_{core} - n_{clad}) \tag{2.4}$$

where *l'* and *l* are the interferometer lengths in the core-core mode coupling scheme and core-cladding mode coupling scheme, respectively, n_{core} and n_{clad} are the effective refractive indices for the core mode and cladding modes, respectively. It is noted that the above equations do not distinguish different cladding modes as in fact several cladding modes could be excited to share the energy of light which is coupled into the cladding region from core mode.

2.4 Comparison with regular FBG and random FBG

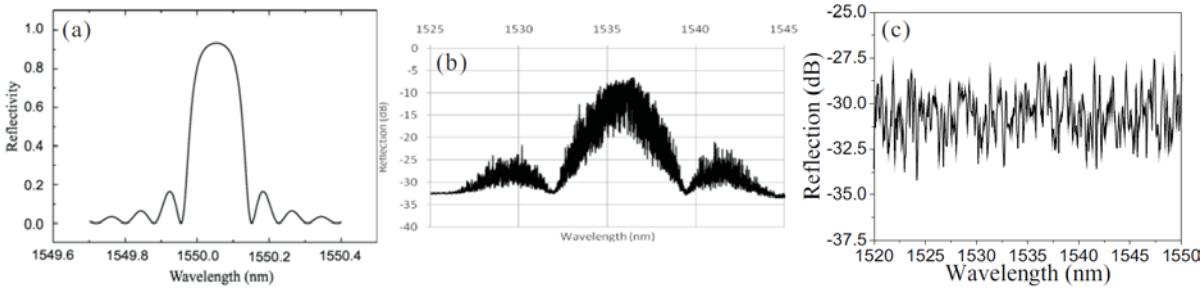

Figure 2-3. Reflection spectra of (a) regular FBG, (b) random FBG, and (c) fiber random grating.

The reflection spectrum of the proposed fiber random grating is compared with those of a regular FBG and a random FBG. In a regular FBG, the index modulation along the fiber core takes the form of a phase and amplitude-modulated periodic waveform:

$$\delta n(z) = \delta n_0(z)[1 + m\cos(\frac{2\pi z}{\Lambda} + \phi(z))] \tag{2.5}$$

Where δn is the index perturbation, z is the position along the fiber, Λ is the grating period, $\phi(z)$ is the phase term, m is the contrast of the modulation determined by the visibility of the writing laser fringe pattern. The grating filter characteristics can be analyzed through the coupled-mode theory. The simplest form of this analysis leads to a single Ricatti differential

equation for a modified local reflectivity $\rho(z)$, which could be easily integrated by standard numerical methods. The reflectivity of the grating at the line center is expressed as

$$R=\rho\rho^{*}=\frac{\kappa^{2}\sinh^{2}(\alpha L)}{\kappa^{2}\cosh^{2}(\alpha L)-\hat{\sigma}^{2}} \tag{2.6}$$

with

$$\begin{cases} \alpha=\sqrt{\kappa^{2}-\hat{\sigma}^{2}} \\ \hat{\sigma}=\delta+\sigma \\ \kappa=\dfrac{\pi}{\lambda}m\delta n \\ \delta=\dfrac{2\pi n}{\lambda}-\dfrac{\pi}{\Lambda} \\ \sigma=\dfrac{2\pi}{\lambda}\delta n \end{cases} \tag{2.7}$$

The above equations give the analytical solution of the reflection spectrum of a regular FBG and the corresponding reflection spectrum is shown in Figure 2-3(a). The maximum reflectivity of the FBG increases with the total grating length L and the index modification depth δn. The bandwidth decreases with the grating length and increases with the index modification depth. A Bragg grating is able to couple different modes in reflection and transmission direction as long as two conditions are satisfied: 1) phase matching condition and 2) sufficient mode overlapping condition. The phase matching condition is given by

$$n_{eff}-\frac{\lambda}{\Lambda}=n'_{eff} \tag{2.8}$$

where n_{eff} is the effective refractive index of the incident fundamental core mode; n'_{eff} is the effective refractive index of grating-coupled reflected (which is a negative value) or transmitted mode. Following this phase matching condition, with a sufficient fine pitch that satisfies the Bragg condition:

$$\lambda_{B}=2n_{eff}\Lambda \tag{2.9}$$

the forward-propagating bound-mode will be reflected as backward-propagating bound-mode with the same order. It should be noted that other modes at shorter wavelengths could also be excited from the incident fundamental mode, most of which however will be reflected or absorbed, or radiated away from the fiber. Cladding modes can be excited interacting with the forward-propagating fundamental core mode, leading to a series of transmission dips in the spectrum at wavelengths shorter than the Bragg wavelength.

In the random FBG, phase errors are introduced randomly and continuously along the grating profile by the friction between the fiber and the mount when the fiber is pulled for grating inscription. Note that the introduced phase noises in the phase term of Eq. (2.5) are small and the grating periods are only slightly modified, leading to quasi-periodical index modulations. Thus the random FBG could be regarded as a succession of a great number of short length gratings of slightly different lengths and small random phase shifts between them. The reflection spectrum of this random FBG is shown in Figure 2-3(b), where dense small ripples are superimposed with a typical general FBG reflection spectrum. The general envelope of the reflection spectrum originates from the quasi-periodical index modulations, which still constitute an FBG structure having similar spectral characteristics as the regular FBGs. The small ripples arise from the light coupling among the large number of short sub-gratings with different spacing, which forms many random Fabry-Perot etalons. Due to the large number of the grating pairs, the collective reflection spectrum loses the individual Fabry-Perot characteristic and shows noisy interference patterns.

The case in the proposed fiber random grating is completely different from the above two cases as shown in Figure 2-3(c), where no periodicity in the index modulation is maintained. Every index modification plane in the fiber random grating is inscribed independently without using a phase mask, which eliminates the phase correlation between the neighboring

planes. Moreover, the plane spacing is randomly controlled by dithering the objective lens used for focusing the fs laser pulse. The index modification depth is also different with planes, as one plane is made by using a single laser pulse, and the laser power varies for each individual pulse, which is opposed to the case where the index modification discrepancy is reduced by using multiple laser pulses for inscription at one region in the fabrication of FBG or random FBG. Consequently, such a fiber random grating with random periods and random index modulations loses the general spectral characteristic of FBG and displays a noisy multiple-interference reflection spectrum resulting from the superposition of many low-finesse FPIs and MZIs.

2.5 Fiber random grating based multi-parameter sensor

Optical fiber based sensors have received a great deal of attention over the past several decades for increased sensitivity over existing techniques, geometric versatility, immunity to harsh environments, and inherent compatibility with optical fiber communication systems. In particular, multi-parameter optical fiber sensors that monitor physical, chemical, and biological parameters are of relevant importance in numerous areas including structural health monitoring, environmental pollution control, biomedical applications and so on [51-53]. The measurands of temperature, axial strain and surrounding refractive index are among the most important parameters in the above applications however they usually exert crosstalk effects on the response of sensors making it difficult to discriminate the individual measurand. Thus, it is essential to investigate these parameters simultaneously in order to eliminate the dependence of one parameter upon another [54-56]. Discrimination between temperature and surrounding refractive index has been published in earlier works including using a slanted multimode FBG [57], a tapered single mode fiber based Mach-Zehnder

interferometer (MZI) [58], a cascaded optical fiber device of long period grating (LPG) and photonic crystal fiber modal interferometer [59], a surface LPG inscribed in a D-shaped photonic crystal fiber [60], and a tapered bend-insensitive fiber interferometer [61] etc. To make a step forward, simultaneous three parameter sensing, especially the measurement of temperature, axial strain, and surrounding refractive index has also been reported using an etched-core FBG [62], a tilted FBG [63], polymer-coated FBGs [64], and a cascaded fiber long period and Bragg gratings [65]. However, these FBG or LPG based devices using either phase mask or etching/coating techniques and requiring critical alignment and vibration control make themselves more complex and costly. Our group also presented a work using tapered bend-insensitive fiber for the discrimination of the three parameters [66]. However, the fragile tapered structure deteriorates the physical strength and durability of the sensing device and makes it vulnerable to the external physical disturbances. In this work, a novel random grating fiber-optic sensor is proposed and fabricated for multi-parameter discrimination measurement based on a wavelength-division cross-correlation method. Temperature, axial strain, and refractive index are calibrated by monitoring the linear peak wavelength shift in different wavelength regions. A sensor character matrix composed of different rates of wavelength shifts provides the access for the simultaneous measurements for all three parameters.

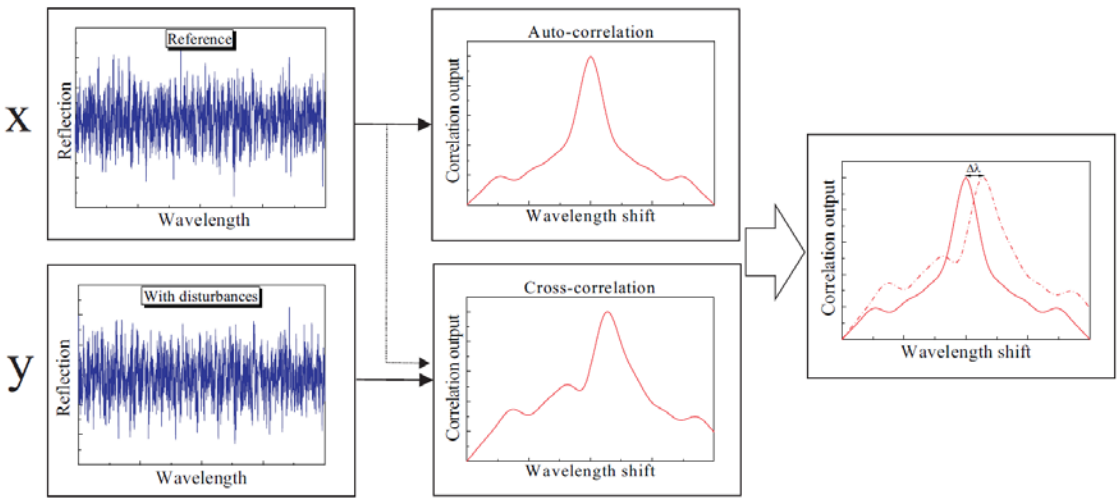

Figure 2-4. Correlation analysis flow chart for simulated reflection spectra.

Prior to the experiments, simulations of the influence of the measurands on the fiber random grating spectrum were conducted. The measurands, such as temperature, axial strain, or surrounding refractive index variations may cause changes in the interferometer length and effective refractive indices of the core mode and cladding modes in both the core-core mode coupling and core-cladding mode coupling of the FPIs and the MZIs in the fiber random grating. According to Eq. (2.3) and (2.4), such changes will accordingly result in a phase shift that leads to a spectral shift in the corresponding reflection spectrum as compared to the case without disturbances. A linear peak wavelength shift response could be found for any specific MZI or FPI so that the superimposed spectral shift from all of the MZIs and FPIs along the random grating sensor is expected to be linear as well. However, it is impossible to observe the spectral responses from the entire random grating length by conventional peak wavelength inspection methods typically used in FBG or LPG sensors. Thus the spectrum correlation analysis is instead employed to extract the spectral shift information, and the flow chart is shown in Figure 2-4. Two simulated reflection spectra spreading over a 200 nm range are presented, one as a reference and the other with an

interferometer length and effective refractive indices of the core and cladding modes linearly varied. The cross-correlation *Rxy(n)* is obtained by performing the cross-correlation calculation for the two reflection spectra using the following equation,

$$Rxy(n) = \frac{1}{N}\sum_{k=0}^{N-1} x(k)\cdot y(n+k) \tag{2.10}$$

for n = -(N-1), -(N-2), …, -1, 0, 1, …, N-2, N-1, where N is the total sampling data points, $x(n)$ and $y(n)$ represent two spectral data sequences. The elements whose indices are either negative or larger than N-1 in $x(n)$ and $y(n)$ are equal to zero. It is seen that a correlation peak emerges, deviating slightly from the center of the spectral range in the cross-correlation spectrum. For comparison, the autocorrelation of the simulated reference spectrum shows that the correlation peak locates exactly at the center of the spectral range. The shift of the correlation peak could be converted to the random grating spectral shift information for the quantification of the parameter variations.

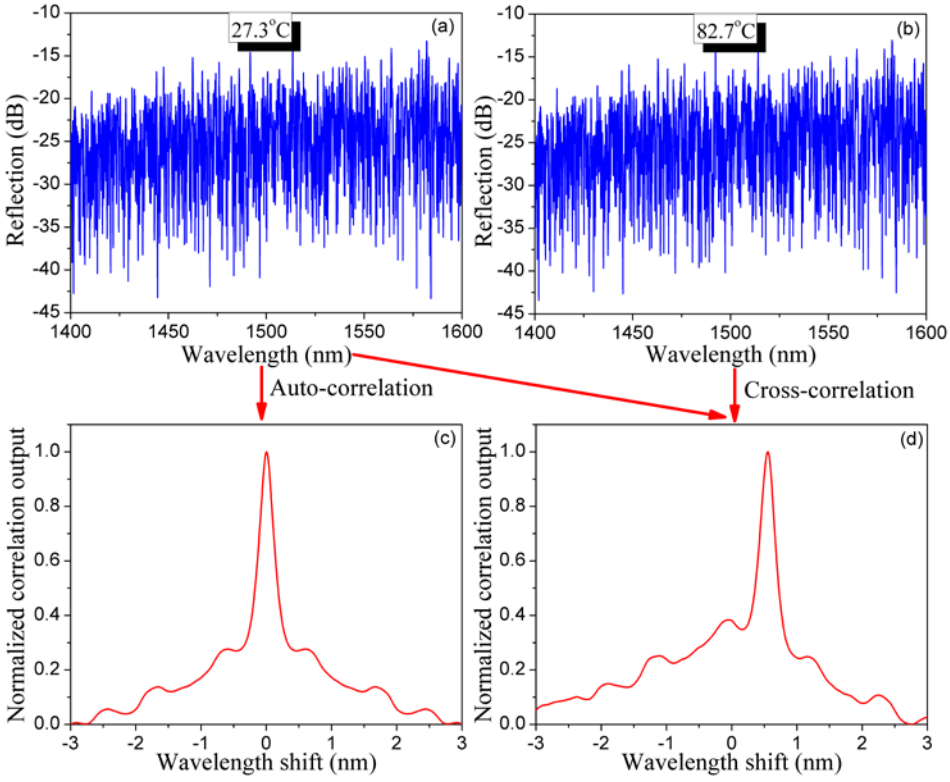

Figure 2-5. Measured reflection spectra of the random grating at reference temperature (a) and changed temperature (b); (c) Auto-correlation spectrum of (a); (d) Cross-correlation spectrum of (a) and (b).

In experiments, temperature measurements were conducted by placing the random grating sensor into an oven with a temperature increase step of around 5 ^{o}C. Reflection spectra at each temperature was recorded when the temperature inside the oven remained stable. To characterize the strain sensitivity of the random grating sensor, the two ends of the sensor were anchored horizontally between a motorized translational stage and a stationary stage using super glue. The system is capable of stretching the sensor longitudinally by manipulating the motorized stage along the axis of the random grating sensor with a sequential strain step of 100 με. The immersion liquids used in the refractive index measurements were glycerol solutions at different concentrations. The percent by weight of glycerol in these solutions could be utilized to determine the solution refractive index, which provides a refractive index range from 1.332 to 1.384. The recorded reflection spectra of the fiber random grating under different environmental condition would be processed by using the spectral correlation method following the flow chart as shown in Figure 2-4. For example, two reflection spectra that one at 27.3 ^{o}C and the other one at 82.7 ^{o}C, are shown in Figure 2-5(a) and (b). The auto-correlation and cross-correlation calculations were performed respectively, as illustrated in Figure 2-5(c) and (d). Cross-correlation peak wavelength shift in Figure 2-5(d) demonstrates that the temperature variation indeed exerts an impact on the reflection spectrum of the sensor and is in accordance with the simulation outcome.

To simultaneously measure the temperature, axial strain, and refractive index using the random grating sensor, a wavelength-division cross-correlation method is employed to extract the responses of the random grating sensor to each of the environmental parameters

investigated in the experiment as shown in Figure 2-6(a). It is based on the fact that the spectral response is highly dependent on the dispersion effects of the effective refractive indices of the core mode and cladding modes when the broadband light source is employed. The mode field cross-sectional intensity distributions of both core mode and cladding modes vary with the input light wavelength and are impacted by the external disturbances with different extents at different wavelengths. Thus the effective refractive indices of core mode and cladding modes at different wavelength regions vary with different levels, leading to distinct phase changes in Eq. (2.3) and Eq. (2.4) and different resultant spectral shifts. The reference reflection spectrum of the random grating at 27.3 ^{o}C and with zero strain was recorded with a spectral range from 1400 nm to 1600 nm. On the one hand, the separation between the selected wavelength sub-regions is required to be large enough to lead to a sharp distinction in wavelength shift related sensitivities for different spectral sub-regions. On the other hand, a wavelength region with a wide spectral range is preferred to ensure better sensing resolution owing to the increased data points used for cross-correlation. Given the limited spectral range and finite data points a broadband light source could provide, as well as the number of desired measurands, the appropriate selection of wavelength sub-regions is critical to multi-parameter sensing with discrimination capabilities. The whole spectrum is then divided into three subsections, 1400 nm-1450 nm (short-wavelength), 1475 nm-1525 nm (middle-wavelength) and 1550 nm-1600 nm (long-wavelength), each of which covers 50 nm wide range. The same division is applied to the following reflection spectra measured with varied temperature, axial strain, and surrounding refractive index. The cross-correlation algorithm is performed in each of the corresponding spectrum subsections between the reference reflection spectrum and the measured one with changed parameters. Due to the wavelength dependent response of the random grating sensor, correlation calculations using

different spectrum subsections would result in distinct responses of central peak shift in the cross-correlation outcome spectra.

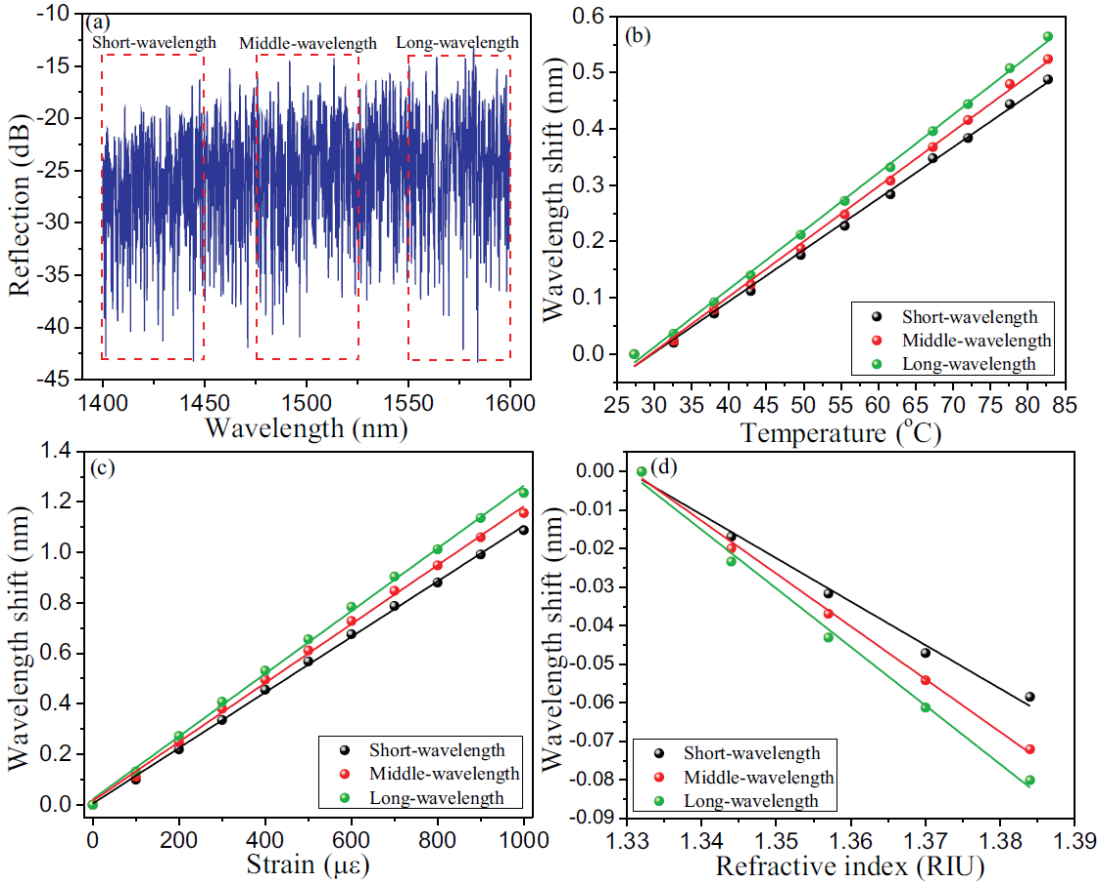

Figure 2-6. (a) Three spectrum subsections selected in the reflection spectrum of fiber-optic random grating; cross-correlation peak wavelength shift calibration results for (b) temperature, (c) strain, and (d) refractive index.

Figure 2-6(b)(c)(d) present the cross-correlation peak wavelength shift based calibration plots for each of the three sensing parameters. The temperature measurement results yielded the cross-correlation peak wavelength shift related temperature coefficients of 9.12 pm/^{o}C, 9.78 pm/^{o}C, and 10.32 pm/^{o}C for the short-wavelength, middle-wavelength and long-wavelength subsections, respectively, as shown in Figure 2-6(b). Then the spectral shift related axial strain coefficients for the three subsections are 1.10 pm/με, 1.17 pm/με, and

1.24 pm/με, respectively, and are plotted in Figure 2-6(c). The spectral shift related refractive index coefficients are -1129.2 pm/RIU, -1369.7 pm/RIU, and -1520.6 pm/RIU for the three subsections, respectively, as shown in Figure 2-6(d). The cross-correlation results in the three spectral ranges exhibit distinctive dependences in temperature, axial strain and refractive index, and thus enable the multi-parameter sensing application.

The temperature, strain and refractive index coefficients calibrated above give an access to construct a character matrix of the proposed random grating sensor, which could facilitate the discrimination among the temperature, the axial strain and the refractive index, achieving simultaneous multi-parameter measurements. Defining the cross-correlation peak wavelength shift related temperature, axial strain and refractive index coefficients of the *i*th subsection of the whole spectrum range respectively as C_T^i, C_ε^i, and C_{RI}^i, the spectral shift related character matrix $M_{T,\varepsilon,RI}$ is obtained to retrieve the temperature, axial strain and refractive index information as follows:

$$\begin{pmatrix} \Delta\lambda_c^1 \\ \Delta\lambda_c^2 \\ \Delta\lambda_c^3 \end{pmatrix} = M_{T,\varepsilon,RI} \begin{pmatrix} \Delta T \\ \Delta\varepsilon \\ \Delta RI \end{pmatrix} = \begin{pmatrix} C_T^1 & C_\varepsilon^1 & C_{RI}^1 \\ C_T^2 & C_\varepsilon^2 & C_{RI}^2 \\ C_T^3 & C_\varepsilon^3 & C_{RI}^3 \end{pmatrix} \begin{pmatrix} \Delta T \\ \Delta\varepsilon \\ \Delta RI \end{pmatrix}, \tag{2.11}$$

where $\Delta\lambda_c^i$ are the cross-correlation peak wavelength shifts associated with the *i*th subsection of spectral range, and ΔT, $\Delta\varepsilon$, and ΔRI are the temperature, axial strain and refractive index changes. Error analysis for the simultaneous multi-parameter measurements is given by [67]:

$$\begin{pmatrix} \delta T \\ \delta\varepsilon \\ \delta RI \end{pmatrix} = \frac{M'_{T,\varepsilon,RI}}{\Delta} \begin{pmatrix} \delta\lambda_c^1 \\ \delta\lambda_c^2 \\ \delta\lambda_c^3 \end{pmatrix}, \tag{2.12}$$

where δT, $\delta\varepsilon$, and δRI denote the errors of temperature, axial strain, and refractive index, respectively, Δ is the determinant of $M_{T,\varepsilon,RI}$, $M'_{T,\varepsilon,RI}$ is the adjugate matrix and $\delta\lambda_c^i$ are the errors in cross-correlation peak wavelength shift associated with the *i*th wavelength

subsection. The maximum errors of temperature measurements are 0.16 pm/^{o}C, 0.16 pm/^{o}C, and 0.12 pm/^{o}C, and the axial strain measurement errors are 0.01 pm/με, 0.02 pm/με, and 0.02 pm/με, and the refractive index measurement errors are 59.0 pm/RIU, 39.7 pm/RIU, and 65.8 pm/RIU, for the three subsections respectively.

2.6 Conclusion

In conclusion, a novel sensor based on the fs laser fabricated random gratings in SMF has been proposed to realize the discrimination of temperature, axial strain and refractive index by monitoring the cross-correlation peak wavelength shift in different spectral ranges. The spectral shift induced by the aggregated responses of numerous MZIs and FPIs integrated in the random grating to different measurands is inspected by the spectrum correlation method. The significant wavelength-dependent spectral shifts in the cross-correlation algorithm provide an excellent opportunity for simultaneous three and even more parameter measurements. The developed sensor can be potentially applicable in areas of engineering, biomedical, biological, and environmental sensing with its robust physical strength and high sensitivities.

Chapter 3 Introduction of random fiber lasers

This chapter presents comprehensive introduction of the current state-of-art development of random fiber lasers. Different random fiber lasers are categorized and reviewed. The lasing feature and properties, linewidth characterization, laser noise measurement, and important applications of random fiber laser are described and summarized, respectively. Section 3.1 categorizes different random feedback mechanisms in optical fibers. Section 3.2 studies random fiber lasers based on various gain mechanisms. Section 3.3 introduces lasing characteristics and mode selection in random fiber lasers as well as linewidth characterization technique for random fiber lasers. Section 3.4 describes intensity noise measurement technique for random fiber lasers. Section 3.5 introduces frequency noise measurement technique for random fiber lasers. Section 3.6 summarizes important applications of random fiber lasers.

3.1 Random feedback mechanisms in optical fibers

As been discussed in Chapter 1, traditional random lasers are realized by pumping and utilizing the disordered structures of 3D materials and media, such as powders, polymers, dye material, porous glasses and so on. However, the control of the laser output performance in these 3D random lasers is challenging and the lasing efficiency is low. One effective way to overcome these problems of 3D random lasers is to use lower-dimension random systems. Optical fibers, being a typical one-dimension waveguide, draw the first attention to make

low-dimension random lasers come true. An initial work demonstrated pulsed random lasing in a few-millimeter-long photonic crystal fiber with hollow core filled with random material consisting of Rhodamine 6G dye solution with TiO_2 particles [68]. This pioneering work, however, lacks the advantages of simplicity and practicability. It was soon realized that the optical fiber itself is able to act as gain and scattering medium at the same time, which significantly improves the directionality of random lasing and lasing efficiency. The first work realizing random fiber laser was proposed in 2010 by S.K. Turitsyn [27], where a stable lasing at 1550nm was demonstrated in a conventional telecom optical fiber with Raman gain distributed along an 83-km long span. By pumping the long telecom fiber, stimulated Raman scattering (SRS) was triggered to provide gain in the open cavity. The random inhomogeneity of the refractive index along the fiber results in numerous scattering centers that randomly reflect incoming light waves back, providing random distributed feedback. Following this work, various gain mechanisms and random feedback mechanisms in optical fibers have been investigated and employed to achieve random fiber lasers. The following sections will describe the physical fundamentals of the feedback mechanisms in optical fibers and introduce various enhanced feedbacks by using different techniques.

3.1.1 Intrinsic Rayleigh scattering

Rayleigh scattering is the elastic scattering of light or other electromagnetic radiation by particles much smaller than the wavelength of the radiation. The amplitude of light scattered from within any transparent dielectric is inversely related to its wavelength. The wavelength dependence is characteristic of the dipole scattering. The electric dipole in the dielectric is oscillating in time, which can be considered as a harmonically oscillating electric dipole with angular frequency ω and a dipole moment p_0 along the z-direction of the form

$$p(r,t) = p(r)e^{-i\omega t} = p_0 \hat{z} e^{-i\omega t} \tag{3.1}$$

In vacuum, the exact field produced by this oscillating dipole can be derived using the retarded potential formulation as:

$$\begin{aligned} E &= \frac{1}{4\pi\varepsilon_0}\left\{\frac{\omega^2}{c^2 r}(\hat{r}\times p)\times\hat{r} + \left(\frac{1}{r^3} - \frac{i\omega}{cr^2}\right)\left[3\hat{r}(\hat{r}\cdot p) - p\right]\right\} e^{i\omega r/c} e^{-i\omega t} \\ B &= \frac{\omega^2}{4\pi\varepsilon_0 c^3}\hat{r}\times p\left(1 - \frac{c}{i\omega r}\right)\frac{e^{i\omega r/c}}{r} e^{-i\omega t} \end{aligned} \tag{3.2}$$

After calculating the time-averaged Poynting vector, the total time-average power radiated by the field can be obtained as

$$P = \frac{\mu_0 \omega^4 p_0^2}{12\pi c} \tag{3.3}$$

The above equation reveals that the radiation power from the dipole oscillation is dependent on the fourth power of the frequency of the radiation, which is in accordance with the Rayleigh scattering.

In optical fibers, Rayleigh scattering is one of the effective scattering mechanisms that provide one-dimensional random feedback. A large percentage of reported random fiber lasers so far are realized based on the intrinsic Rayleigh scattering in standard telecom optical fibers. The intrinsic Rayleigh scattering in optical fibers is fundamentally a loss mechanism that originates from the density variations frozen into the fused silica fiber during the manufacture process. This density fluctuation, unlike to the optical phonons generated in Raman scattering or acoustic phonons generated in Brillouin scattering, is non-propagating and static. Thus Rayleigh scattering is a quasi-elastic scattering process that induces no frequency shift between incoming wave and scattered waves. Although the nature of Rayleigh scattering allows the incoming light to be scattered from the local density fluctuations in all directions, the optical fiber waveguide only supports the scattered lights

that can be totally reflected counter-propagating respect to the incoming light. The Rayleigh scattering coefficient varies with the wavelength of the light wave and is dominant at short wavelengths:

$$\alpha_R = \frac{C_R}{\lambda^4} \tag{3.4}$$

where C_R is in the range 0.7-0.9dB/(km-μm^4) depending on the constituents of the fiber core. In the standard telecommunication fiber, the Rayleigh scattering has weak reflection coefficient $r \approx 7.3\times10^{-8}$/m along the whole fiber. However, the one-dimensional waveguide structure of optical fibers can facilitate the accumulative effect of backscattered photons in spite of such small r.

In standard telecom SMFs, Rayleigh backscattered light can be modeled as a collection of lights reflected from a sequence of scattering centers. These scattering centers can be seen as multiple reflectors with weak reflectivity. The fiber can be divided into N small sections and the length for each section is ΔL=L/N. Each section has one scattering center, which is randomly located within the section with uniform distribution and assumed to have random varying reflection coefficients. So when an input light with a coherence length covering the fiber length L, the electric field of Rayleigh backscattered light can be written as:

$$E_R = E_0 \sum_{k=1}^{N} \exp(-2\alpha L_k) r_k \exp(-i\frac{4\pi n L_k}{\lambda}) \tag{3.5}$$

where α is the attenuation coefficient of the optical fiber, L_k is the length of the kth scattering center of the fiber, r_k is the reflection coefficient of the kth scattering center. Note that this is a simplified model for the intrinsic Rayleigh scattering in fiber and its accuracy depends on the density of the scattering centers set along the fiber. In reality, these scattering centers are densely distributed along the fiber length and their spacing is so small that dense resonant

modes would be present when Rayleigh scattering is used as feedback in random fiber lasers. In this case, the large number of resonant modes with extremely small free spectral range would induce strong mode competition and mode hopping effect in the lasing system, which can further be intensified by external disturbances such as temperature variation and vibrations in the surrounding environment. As a result, the relative intensity noise of the Rayleigh scattering based random fiber lasers is relatively high although single-mode operation can be achieved.

It was also found that the Raleigh backscattered light has similar spectral properties with the input light. By measuring the frequency information of the Rayleigh backscattering light, the linewidth of input light source can be recovered. The mean reflected light intensity is independent of the source light coherence, while its variance is influenced by the input light polarization states [69]. In low-birefringence fibers, like standard SMF, the state of polarization of the incoming light is preserved in Rayleigh backscattering light [70], which is beneficial for the polarization matching induced lasing efficiency improvement.

3.1.2 Enhanced Rayleigh scattering

Due to the weakness and accumulation nature of the intrinsic Rayleigh scattering in the standard telecom SMFs, long fiber length is usually required for random fiber lasers based on the intrinsic Rayleigh scattering to provide enough feedback strength and increase lasing efficiency. An effective way is to use optical fibers that have higher loss than the standard SMF, which is able to provide enhanced Rayleigh backscattering and thus decrease the required fiber length. For example, a 300-m SMF with high Rayleigh loss (~17dB/km) was utilized in a single-end Brillouin random fiber laser (BRFL) proposed in [71]. In a later work, a novel non-uniform fiber was employed with enhanced Rayleigh feedback to achieve a

tunable Erbium-doped fiber random laser (EDFRL) with a 3dB linewidth of less than 2kHz [72]. The non-uniform fiber was fabricated with the mode field diameter from 5μm at one end to 7μm at the other end and consequently with a stronger refractive index inhomogeneity along the fiber axis [73]. It was demonstrated that the Rayleigh scattering coefficient is enhanced to ~-34dB/km, which is 2 orders higher than standard telecom SMFs. Another alternative with enhanced Rayleigh scattering is the polarization-maintaining fiber (PMF). The two-dimensional stress from Baron-doped-silica rods in the fiber introduces additional transverse non-uniformity into fiber core to increase the Rayleigh scattering coefficient. However, compared with the high-loss Rayleigh fiber and non-uniform fiber, the improvement of Rayleigh scattering strength in PMF is still limited.

It has to be noted that although the above-mentioned optical fibers somehow show enhanced Rayleigh scattering effect due to the increased structural non-uniformity, long fiber length is still required when they are applied in random fiber lasers, which could introduce a large density of random modes with strong mode competitions. In addition, long Rayleigh fibers would be more sensitive to the external disturbances, which makes the laser cavity unstable and intensifies the mode-hopping effects. Therefore, a more compact fiber structure with uncompromised feedback strength is highly preferred. Various modification techniques have been implemented in fibers to enhance the Rayleigh scattering. One typical method is to inscribe random grating along the optical fiber core regions. An early work inscribed a series of FBGs along an erbium-doped SMF [74]. FBGs with same index modulation periods were randomly spaced with separations within 4.2-5.8mm. In another work, a random FBG with randomly distributed phase shifts was fabricated along one meter long fiber [50]. A ramp signal was applied to the piezomounted phase mask, to which a DC bias was applied during the writing process to introduce random phase shifts to the grating. The resultant random

FBG has a quasi-periodic index modulation and much higher reflection strength, which eliminate the needs of tens of kilometer long fibers for Raman random fiber lasers. CO_2 laser has also been used to inscribe random gratings along SMFs. The CO_2 laser operates at wavelength of 10.6μm that overlaps with an OH absorption band in fused silica, which leads to a quick thermal response to a sharp temperature rise in the fiber. The refractive index of the irradiated points was modulated through the localized residual thermal stress induced by the thermal gradients. 100 randomly spaced refractive index modulation regions over 10 cm SMF were fabricated with significant enhancement in Rayleigh scattering [75]. Other methods to make compact and enhanced Rayleigh feedback fiber structures include making a series of abrupt tapers along the SMF using stretching stages and oxyhydrogen flame. 21 tapers with taper length of 2cm and waist diameter of 112.09μm were made along a 110m SMF in [76].

3.2 Random fiber lasers with different gain mechanisms

Optical gain is another key factor that builds up a laser. Different gain mechanisms in optical fibers have been employed to achieve random fiber lasers. Thanks to the compact one-dimensional waveguide structure in optical fibers, these nonlinear gain processes usually possess high efficiency and amplification magnitude, which is crucial to compensate the high loss induced by the open cavities in random fiber lasers. The following sections will describe the physical fundamentals of common gain mechanisms in optical fibers and random fiber lasers that have been reported based on these gains in details.

3.2.1 Raman random fiber laser

Stimulated Raman scattering (SRS) is an important nonlinear process occurring in optical

fibers, which could be utilized to realize broadband Raman amplifiers and tunable Raman lasers. In telecommunication systems, it is usually negatively regarded as one factor that severely limits the performance of multichannel lightwave systems by transferring energy from one channel to the neighboring channels. The Raman effect was first discovered by Raman in 1928 in the form of spontaneous Raman scattering. This process can transfer part of power from one optical field to another field with a frequency downshift that is determined by the vibrational modes of the molecular medium. The incident light acts as pump light and the generated frequency-downshifted radiation is called Stokes light. Later it was found that with intense pump power, SRS can occur inside the medium with a nonlinear behavior in which most energy of the pump light is transferred to the Stokes light. Figure 3-1 shows a schematic diagram for Raman scattering from a quantum mechanical viewpoint. It can be described as conversion of a photon of energy $\hbar\omega_p$ by a molecule to a lower-frequency photon with energy $\hbar\omega_s$ when the molecule transits to a vibrational excited state.

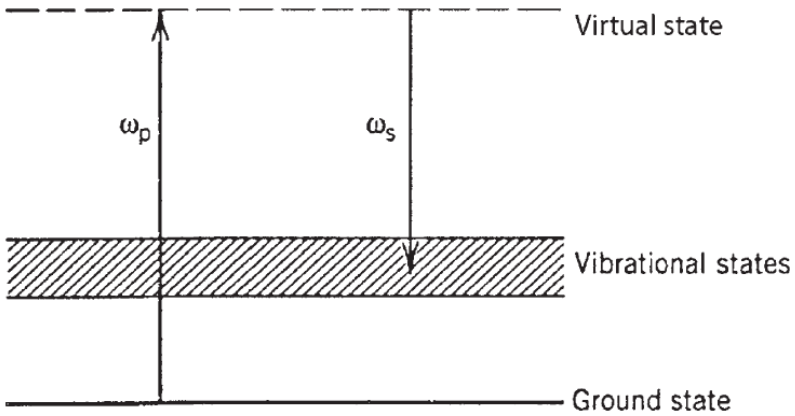

Figure 3-1. Schematic diagram of Raman scattering from a quantum mechanical viewpoint [77].

When CW pump light is launched into an optical fiber with a power value above the SRS threshold, the pump light will interact with the generated Raman Stokes light nonlinearly through SRS process. If the fiber losses are included, the SRS process is governed by the following coupled equations:

$$\frac{dI_s}{dz} = g_R I_p I_s - \alpha_s I_s \tag{3.6}$$

$$\frac{dI_p}{dz} = -\frac{\omega_p}{\omega_s} g_R I_p I_s - \alpha_p I_p \tag{3.7}$$

where α_s and α_p are fiber losses for Stokes and pump lights, respectively; I_s and I_p are Stokes and pump intensities; ω_s and ω_p are Stokes and pump frequencies. g_R is the Raman-gain coefficient, which is a function of the frequency difference between the pump and Stokes waves, i.e. $\Omega=\omega_p-\omega_s$. In general, this coefficient depends on the composition of the fiber core and varies significantly with the fiber core dopants. Figure 3-2 shows the spectrum of the Raman-gain coefficient for fused silica as a function of the frequency shift. It is illustrated that the Raman gain in silica fibers extends over a large frequency range (up to 40THz) with a broad peak located near 13THz, which is due to the noncrystalline nature of silica fiber. With this broadband gain spectrum, optical fibers can act as broadband Raman amplifier.

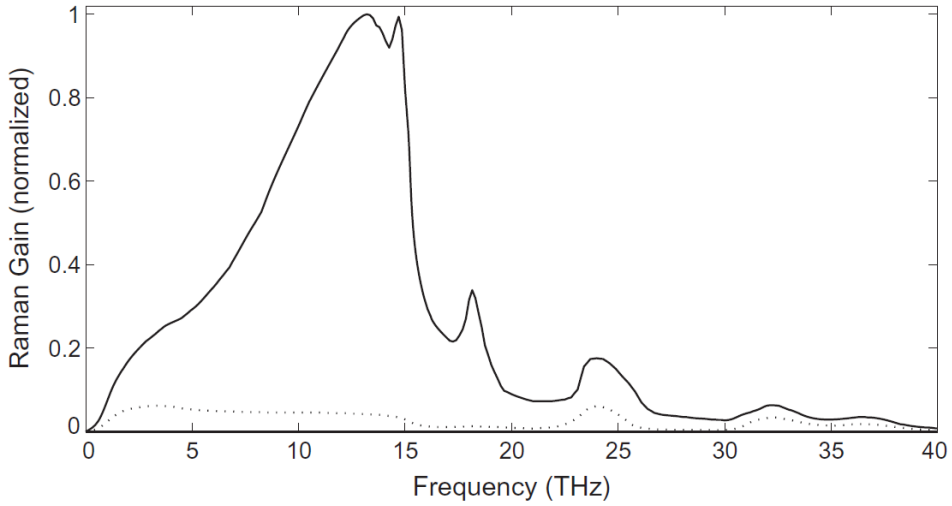

Figure 3-2. Normalized Raman gain spectrum for a fused silica fiber when pump and Stokes waves are copolarized (solid curve). The dotted curve shows the spectrum when the pump and Stokes waves are orthogonally polarized [77].

The SRS threshold is relatively high in optical fibers compared with other nonlinear processes. Assuming a Lorentzian shape for the Raman gain spectrum, the threshold power

of the SRS could be estimated using the equation below:

$$\frac{g_R P_0^{cr} L_{eff}}{A_{eff}} \approx 16 \tag{3.8}$$

where L_{eff} is the effective fiber length; A_{eff} is the effective core area. With a pump wavelength of 1550nm, an effective fiber length of 20km, and an effective core area of 50μm^2, the estimated Raman threshold P_0^{cr} is around 600mW. This indicates that SRS is of higher probability to occur in multichannel systems than in an isolated channel which typically has a power level below 10mW. However, when a high power pump laser is used to pump the optical fiber, the SRS can be triggered, which results in the development of conventional Raman fiber lasers with a tunable frequency range of 10THz as well as Raman fiber amplifier for weak signals.

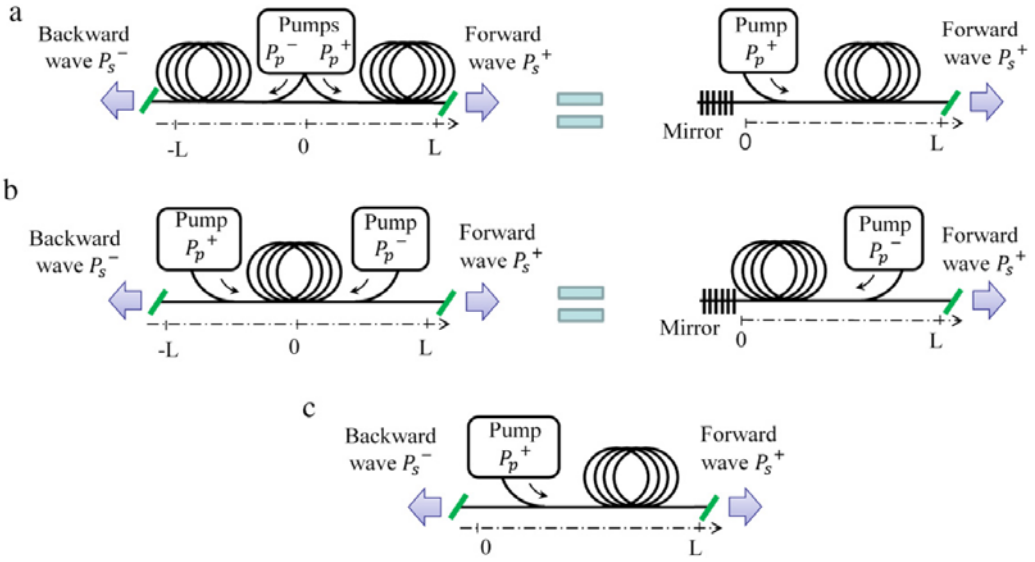

Figure 3-3. Different configurations of Raman random fiber lasers: (a) forward-pumped laser, (b) backward-pumped laser and (c) single-arm configuration. [26]

Different from conventional Raman fiber lasers where fixed cavities are formed by using mirrors or FBGs, Raman random fiber lasers emerged in recently years employ cavity-free structure based on random distributed feedback from Rayleigh backscattering in optical

fibers. The concept of Raman random fiber laser can be treated as a convergence of two distinct types of lasers, namely traditional 3D random lasers and distributed feedback fiber laser. The optical fibers provide one-dimensional waveguide for improving the lasing efficiency and directionality in 3D random lasers; the Rayleigh distributed feedback provides disordered reflection from different scattering centers along the fiber. The first scheme of the Raman random fiber laser was proposed in [27] as shown in Figure 3-3(a). The laser is made up of two equal spans of SMF with a total length of 83km. The total Rayleigh scattering renders reflection ratio up to 0.1%. Two high-power pumps at 1455nm are used to trigger the SRS, providing Raman gain for the laser. In the forward-pumped configuration, the generated Stokes wave is co-propagating with the pump wave. Figure 3-3(b) shows the backward-pumped configuration where the generated Stokes wave is counter-propagating with the pump wave. Both configurations can be regarded equally as shown in the right configurations in Figure 3-3(a) and (b), where one fiber span, one pump source and an additional point-based highly reflecting mirror form the random fiber laser system. Figure 3-3(c) shows another scheme which is operated via the random distributed feedback only. The generation properties of the Raman random fiber lasers are shown in Figure 3-4. The generation threshold, which is a key feature of lasers, is observed in the forward-pumped Raman random fiber laser as shown in Figure 3-4(a). The measured threshold power is relatively large with a value of 0.8W in this kind of random laser due to the high threshold for SRS and low feedback from Rayleigh scattering. It is illustrated in Figure 3-4(b) that below the threshold value, the Raman random fiber laser shows a broadband emission spectrum, which corresponds to the amplified spontaneous emission spectrum of SRS. The lasing spectra experience abrupt narrowing when the pump power increases above the lasing threshold and finally stabilize with a well-confined spectral envelope with a bandwidth of

1nm. As opposed to the conventional fiber laser with well-defined cavity modes, the Raman random fiber laser can be effectively treated as single-mode laser with a continuous spectrum of the width and central frequency defined by the Raman gain profile. As the Raman gain profile has a double-peak structure with two maxima at 1555nm and 1565nm, lasing could be achieved in these two wavelength regions as shown in Figure 3-4(b).

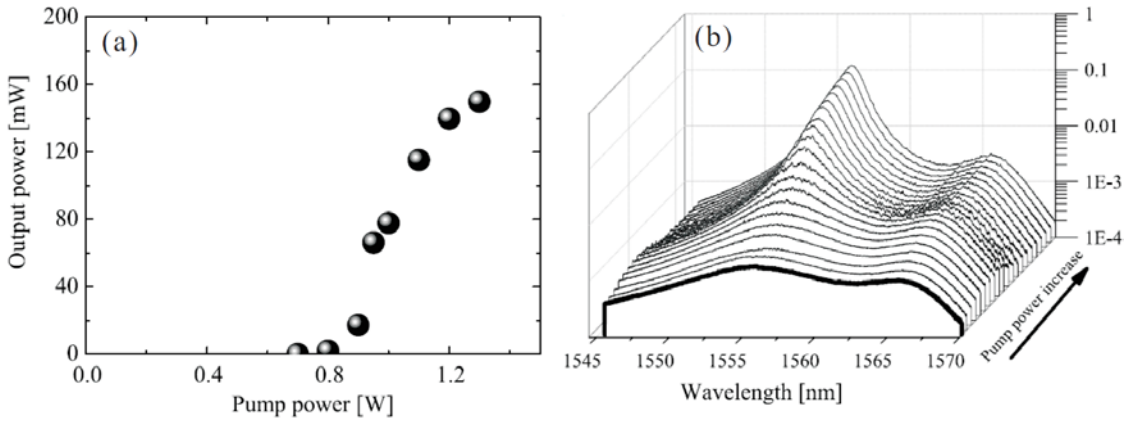

Figure 3-4. (a) Measured output power of Raman random fiber laser [27]; (b) Lasing spectra of Raman random fiber laser as a function of pump power [26].

Besides the emission spectrum centered at 1550nm using 1455nm pump lasers, Raman random fiber lasers operating in other spectral bands are also realized. For instance, Raman random fiber lasers generated at 1455nm [78], 1200nm [79], and 1115nm [80] were reported, which extends the operating spectral bands of the random fiber lasers and are beneficial for applications in telecommunication systems. Multiwavelength Raman random fiber lasers have also been proposed and achieved by using multiple spectral filters such as an array of 22 FBGs [81], all-fiber Lyot filter [82], a Sagnac loop mirror with a high-birefringence photonic crystal fiber [83, 84] and so on.

3.2.2 Brillouin random fiber laser

Contrary to the SRS in optical fibers, the stimulated Brillouin scattering (SBS) is a

nonlinear process that can occur at much lower input power levels. In this process, backward Brillouin Stokes wave is generated, carrying most of the input light energy when the SBS threshold is reached. The nonlinear phenomenon of SBS was firstly observed in 1964 and has been intensively studied after that. The major differences between SBS and SRS lie in that 1) the Stokes wave mainly counter-propagates with respect to the pump light in SBS, while the Stokes wave can propagate in both directions in optical fibers for SRS process; 2) the frequency shift of the Brillouin Stokes light is in the order of 10GHz, which is three orders smaller than that of the Raman Stokes wave; 3) the threshold of SBS can be as low as milli-watt level for a CW pump case, which is much lower than that of SRS.

The process of SBS is usually described as a nonlinear interaction among the pump and Stokes fields and an acoustic wave through the process of electrostriction. The acoustic wave produces density modulations that modulate the refractive index of the medium. This pump-induced index grating scatters the pump light through Bragg diffraction. Scattered light is downshifted in frequency because of the Doppler shift associated with a grating moving at the acoustic velocity V_A. The same scattering process can be viewed quantum mechanically as if annihilation of a pump photon creates a Stokes photon and an acoustic phonon simultaneously. As both the energy and the momentum must be conserved during each scattering event, the frequencies and the wave vectors of the three waves are related by

$$\Omega_B = \omega_p - \omega_s, \quad k_A = k_p - k_s \tag{3.9}$$

where ω_p and ω_s are the frequencies of the pump and Stokes light; k_p and k_s are wave numbers of the pump and Stokes light; Ω_B is the Brillouin frequency. In a SMF, the only possible propagating directions are the forward and backward directions. The conservation of momentum determines that the SBS occurs mainly in the backward direction respect to the

pump light with Brillouin frequency shift given by

$$\upsilon_B = \Omega_B / 2\pi = 2nV_A / \lambda_p \tag{3.10}$$

where n is the effective mode index of the pump light; λ_p is the pump wavelength.

Similar to SRS, the SBS process is also associated with its Brillouin-gain spectrum, which is centered at the Brillouin frequency Ω_B. The bandwidth of the Brillouin gain spectrum is around 10MHz in optical fibers, which is related to the damping time of the acoustic waves generated through the electrostriction. The Brillouin gain has a Lorentzian spectral shape as described as follows

$$g_B(\Omega) = \frac{g_p(\Gamma_B / 2)^2}{(\Omega - \Omega_B)^2 + (\Gamma_B / 2)^2} \tag{3.11}$$

Where Γ_B is the full width at half maximum (FWHM) of the gain spectrum, g_p is the peak value of the Brillouin gain given by

$$g_p = g_B(\Omega_B) = \frac{4\pi^2 \gamma_e^2 f_A}{nc\lambda_p^2 \rho_0 V_A \Gamma_B} \tag{3.12}$$

Where ρ_0 is the material density; γ_e is the electrostrictive constant of silica; and f_A is the fraction by which the SBS gain is reduced of the acoustic and optical modes do not fully overlap inside the fiber. Figure 3-5 shows the gain spectra measured for three different fibers with different structures and doping levels of germania in their cores. All of them show a Brillouin frequency shift in the level of 10GHz and gain spectra with narrow bandwidths in the order of tens of MHz.

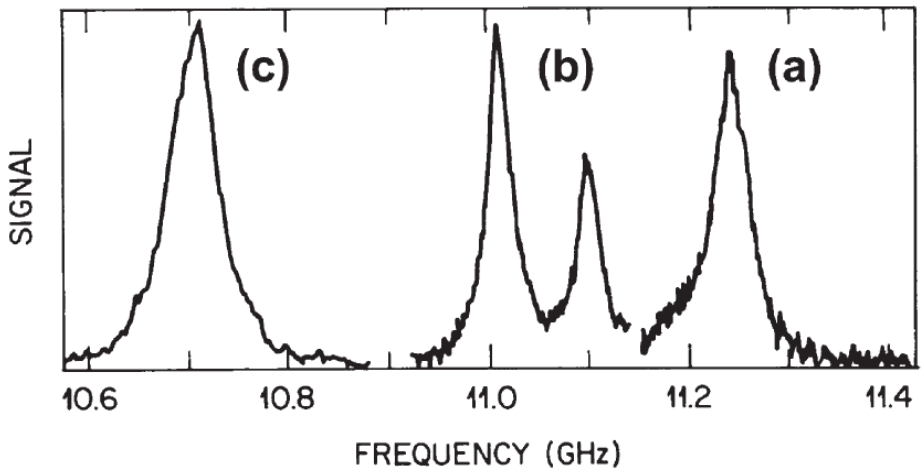

Figure 3-5. Brillouin gain spectra of three fibers: (a) silica-core fiber, (b) depressed-cladding fiber, and (c) dispersion-shifted fiber. [85]

If CW pump light with a power above the SBS threshold is launched into an optical fiber, in the steady-state conditions, the evolution of pump and Stokes waves along the optical fiber could be described as follows

$$\frac{dI_p}{dz} = -g_B I_p I_s - \alpha I_p \tag{3.13}$$

$$-\frac{dI_s}{dz} = g_B I_p I_s - \alpha I_s \tag{3.14}$$

The Brillouin threshold could be estimated using the following relation

$$\frac{g_B(\Omega_B) P_0^{cr} L_{eff}}{A_{eff}} \approx 21 \tag{3.15}$$

Since g_B is much higher than that of the SRS process, in a long fiber section with an effective core area of 80μm^2, fiber loss of 0.2dB/km, and g_B of 5×10^{-11}m/W, the SBS threshold is estimated in the order of 1mW. If the fiber length is shortened, the threshold would increase accordingly. With such a high gain coefficient and low power threshold, SBS could also be utilized in optical fibers to achieve Brillouin fiber lasers and amplifiers.

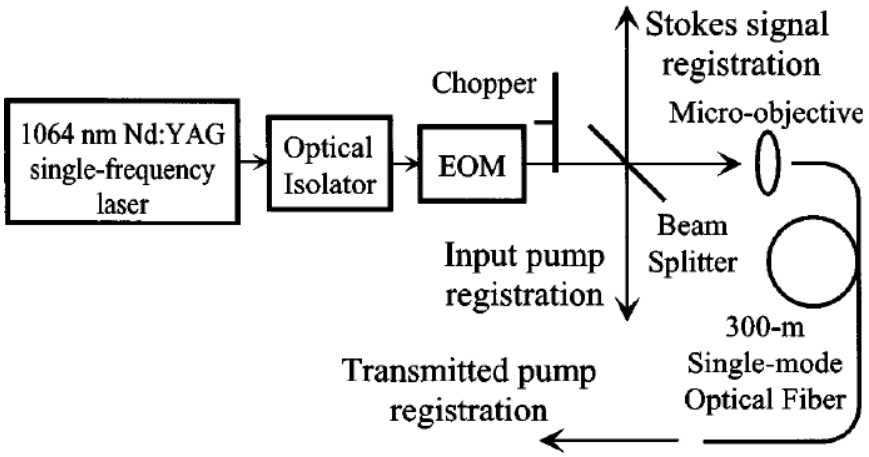

Figure 3-6. Experimental setup of first demonstration of BRFL [71].

Similar to SRS based random fiber lasers, SBS is also an effective gain mechanism to realize Brillouin random fiber lasers (BRFLs). The first BRFL was proposed and demonstrated in 1998 by Fotiadi [71], where a narrow spectrum of Stokes lasing was observed for the SBS process in a 300m single mode fiber with high Rayleigh scattering coefficient. The setup is based on one-end pumping configuration with open laser cavity as shown in Figure 3-6. As the pump light with power above the SBS threshold was launched into the highly-scattering fiber, the Brillouin Stokes wave was generated and counter-propagated along the fiber with respect to the pump light. The doubly-scattered Brillouin Stokes lights would then act as the seed of the new SBS amplification processes. As long as the gain provided by the SBS process compensates the total cavity loss in the system, the Brillouin Stokes lasing would be obtained. It was theoretically shown in [71] that the contribution of Rayleigh scattering makes the distribution of the Stokes output in the form of Gaussian statistics, being completely different from that of normal SBS process, which indeed demonstrates the existence of Brillouin lasing in such a high loss system.

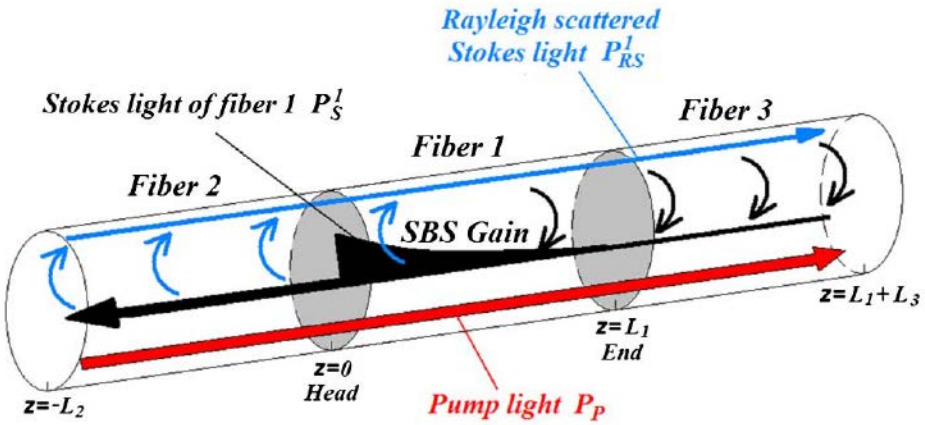

Figure 3-7. Cascaded fiber composed of three types of fibers with different Brillouin frequencies [86].

Later works put many efforts into realizing the BRFL in standard telecom optical fibers. A typical work was published in 2012 by Pang [86], where a cascaded fiber composed of three types of low-loss communication fibers was used as the Brillouin gain medium and distributed feedback medium as shown in Figure 3-7. The Rayleigh scattering of the Brillouin Stokes light created in the middle fiber section along both directions is enhanced by the other two fiber sections. When the Brillouin gain of the middle fiber exceeds the effective loss of the Brillouin stokes light in a round-trip, a narrow linewidth lasing is observed on the top of the Brillouin spectrum line of the middle fiber. The linewidth of this BRFL was measured to be ~3.4kHz, which is much narrower than that of conventional SBS generation spectrum. An improved BRFL based on half-open ring cavity was proposed later [87], where a 25km long SMF was used as SBS gain fiber and another 5.4km non-uniform fiber was used to provide Rayleigh feedback as shown in Figure 3-8. Above the lasing threshold, an ultra-narrow linewidth of 10Hz was obtained for the coherent random lasing spikes on the top of the Brillouin gain spectrum. To improve the laser noises and frequency jitter of the BRFL, a high finesse narrow-band Fabry-Perot interferometer was inserted to the ring cavity to select the lasing frequency [88]. A single-wavelength, narrow-linewidth of 50Hz, and high

frequency stability (<40kHz frequency jitter) coherent BRFL was then achieved.

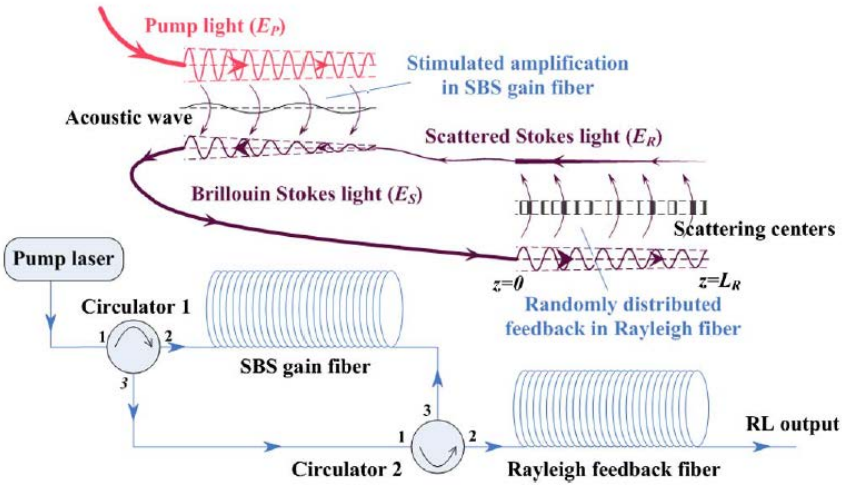

Figure 3-8. Schematic of BRFL with half-open ring cavity [87].

3.2.3 Erbium-doped fiber random laser

Erbium (Er) is a chemical element belonging to the group of rare earth metals. It is widely used in the form of the trivalent ion Er^{3+} as the laser-active dopant of gain media based on various host materials, including both crystals and glasses. The fabrication of the erbium-doped fiber (EDF), similar to that of regular SMF, is processed by delivering the rare earth vapor species to the reaction/deposition zone of a fiber preform through the Modified chemical vapor deposition (MCVD). Such optical fibers doped with the rare earth elements can be used as gain medium of a fiber laser or optical amplifier. The EDF based amplifiers have attracted the most attention because they operate in the wavelength region near 1.55 μm. Their deployment in WDM systems after 1995 revolutionized the field of fiber-optic communications and led to lightwave systems with capacities exceeding 1 Tb/s.

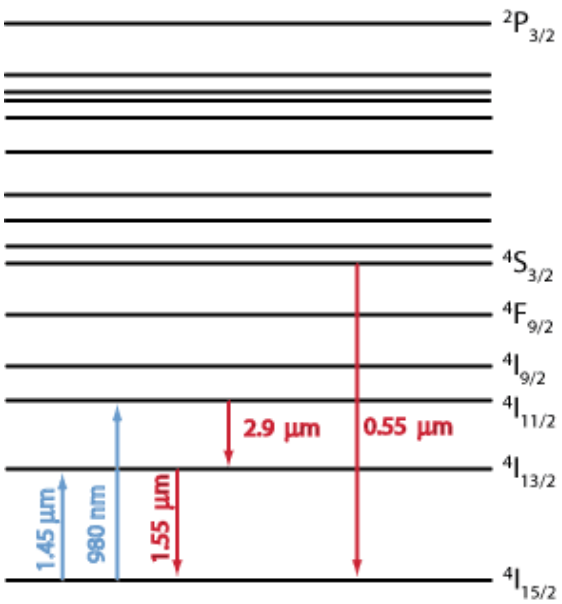

Figure 3-9. Energy level structure of the erbium ion and some common optical transitions.

In order to make EDF provide gain to the lightwave systems, pumping at a suitable wavelength is required to achieve population inversion. The gain spectrum of EDF depends on the pumping scheme as well as on the presence of other dopants in fiber core, such as germania and alumina. The energy levels of the Er^{3+} are broadened by the amorphous nature of silica. Figure 3-9 shows a few energy levels of Er^{3+} in silica fibers. The most common laser transition is that from the $^4I_{13/2}$ manifold to the ground state manifold $^4I_{15/2}$. Depending on the fiber core composition, the transition wavelength is usually between 1.53 and 1.6µm. Due to the quasi-three-level transition, a significant excitation density of the erbium ions is required in order to decrease the threshold pump power for EDF based amplifiers and lasers.

Many transitions can be used to pump the EDF. Efficient EDF pumping uses semiconductor lasers operating near 0.98- and 1.48-µm wavelengths. In the 0.98µm pumping scheme, pump photons at 0.98µm are able to excite ground state carriers to the excited state and create population inversion. Note that the carriers only stay in the excited state for about 1µs, after which they decay into a metastable state through a non-radiative transition. The

energy band of the metastable state corresponds to a wavelength band from 1480nm to 1550nm. Intraband relaxation occurs within the metastable energy band, where the carriers move down from the top of the band to somewhere near the bottom. Finally, when the carriers step down from the bottom of the metastable state to the ground state through radiative recombination, photons in the 1550nm wavelength region are emitted. The carrier lifetime in the metastable state is on the order of 10ms, which is much longer than that in the excited state. Another pumping scheme at 1480nm is usually more efficient than 980nm pumping as it does not involve the nonradiative transition from the 980nm to the 1480nm band. In this case, the 1480nm pump photons directly excite carriers from the ground state to the top of the metastable state and then these carriers transit down to the bottom of the metastable band. Thus the highly efficient 1480nm pumping is more suitable for high-power EDF amplifiers.

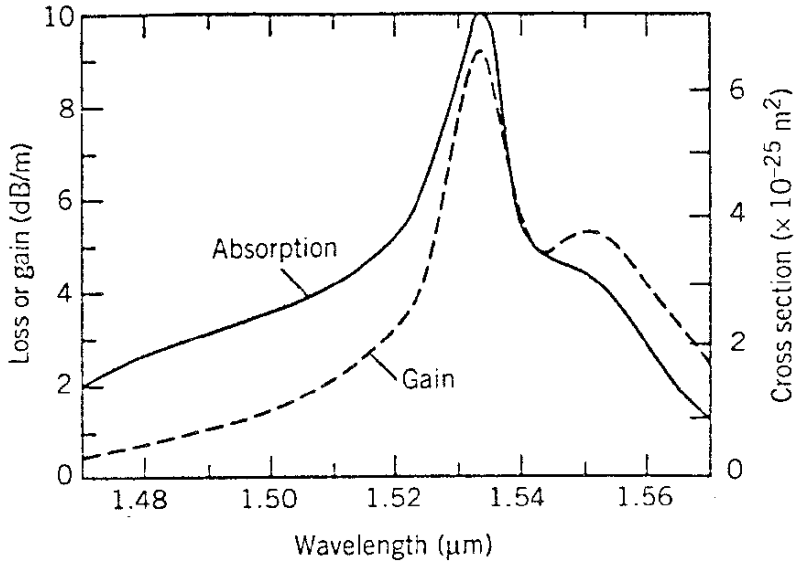

Figure 3-10. Absorption and gain spectra of an EDF amplifier with core doped with germania [89].

Figure 3-10 shows the absorption and gain spectra of an EDF amplifier with the fiber core doped with germania. The shape of the gain spectrum is influenced by the amorphous nature of silica and also depends on other codopants within the fiber core such as germania and

alumina. The gain spectrum of erbium ions alone is homogeneously broadened, whose bandwidth is determined by the dipole relaxation time. Moreover, the Stark splitting of the energy levels further broadens the gain spectrum homogeneously. In addition, the spectrum could be considerably broadened in the presence of randomly located silica molecules, which leads to inhomogeneous broadening of the gain spectrum. When the EDF is pumped for optical amplification within the gain spectrum, the weak signal photon can stimulate the excited erbium ions to emit photons with exactly the same wavelength and phase as the incident photon, leading to the amplification of the incident signal.

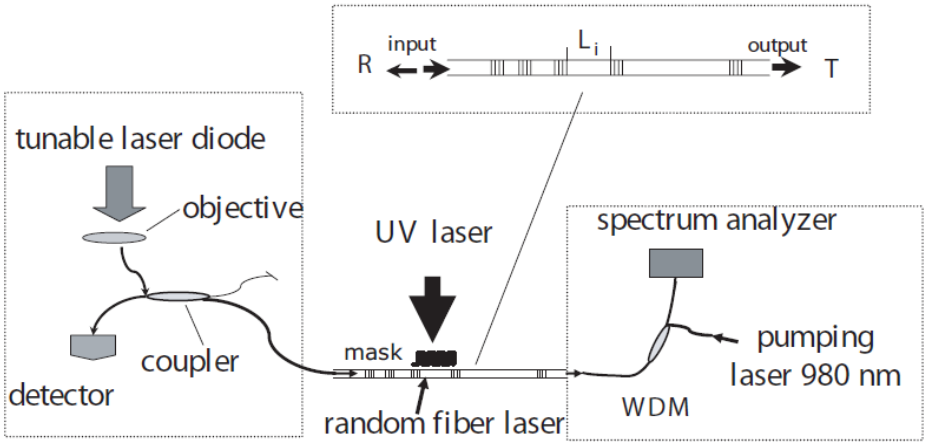

Figure 3-11. Experimental setup of inscribing FBGs with random spacing along a Er/Ge co-doped fiber [74].

The EDFRLs could be generally divided into two categories based on the laser configurations. In the first category, the gain and random distributed feedback are both provided by the EDF. This is commonly achieved by inscribing gratings along the EDF core region. The pioneering work is proposed in 2009, where FBGs were written along an Er/Ge co-doped SMF with random spacing [74] as shown in Figure 3-11. A complex cavity with high quality factor resonances in the range of gain wavelengths centered around 1535.5nm was formed by the random FBG array. The lasing behaviors, such as laser threshold, were

also observed in experiments. Shortly after this work, the Kashyap group proposed a novel random FBG fabrication technique by inserting a large number of randomly distributed phase errors in the grating structures [47]. These errors were introduced by controlling the frictions between the fiber and the mount during the manufacturing process. Such a grating was written in a polarization-maintaining EDF and random lasers were demonstrated by using 976nm and 1480nm pump lasers.

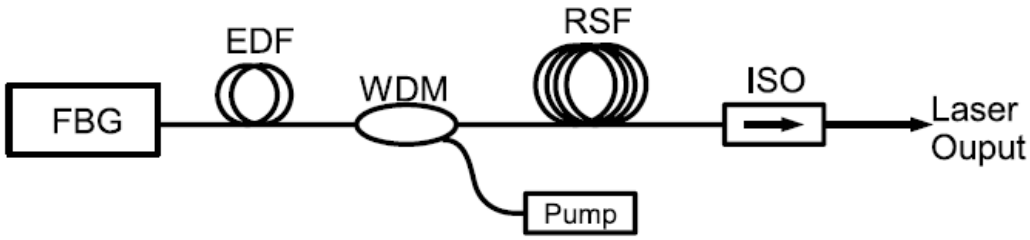

Figure 3-12. Experimental setup of half-open linear cavity RDF based random fiber laser [90].

In the other category of EDFRLs, gain and random feedback are provided separately from different fibers. EDF provides the gain and a separate fiber structure provides random feedback. A typical work of this kind of random fiber laser was presented in 2014, where a half-open linear cavity was formed by enclosing the EDF between an FBG and a long section of Rayleigh scattering fiber [90] as shown in Figure 3-12. The FBG was used to reflect a narrow wavelength band centered at 1539.4nm and with a 3 dB bandwidth of 0.03nm from the amplified spontaneous emission of the EDF. With sufficient length for the Rayleigh scattering fiber, the accumulated distributed feedback can be large enough to overcome the loss induced by the half-open cavity. The proposed random fiber laser is superior to the commercially available narrow-linewidth lasers with suppressed intensity and frequency noises. Another work of this category was realized by constructing a ring cavity with the gain from the EDF and random distributed feedback from a fiber random grating fabricated using CO_2 laser [75]. Around 100 randomly spaced refractive index modulation regions were

written over a 10cm SMF with modifications in both longitudinal and transverse directions. The configuration achieved a tunable EDF based random fiber laser with narrow linewidth of 2.4kHz and low relative intensity noise as well as mitigated frequency jitters.

3.3 Lasing mode and linewidth characterization

As the strength of random distributed feedback from either the intrinsic Rayleigh scattering in long standard telecom SMFs or enhanced scattering in modified fiber structures is large enough to be amplified by the optical gain to overcome the loss in the cavity, random lasing would build up with unique resonance properties. The random distributed scattering centers in the random fiber medium will constitute numerous random resonant cavities, which gives rise to large numbers of resonant modes. Thanks to the elastic nature of Rayleigh scattering, the scattered light waves from the scattering centers could be coherently interfered with each other. With specific gain spectral profile, such process is of high probability to operate with single-mode emission and narrow linewidth.

3.3.1 Lasing mode

In conventional lasers, the resonance frequencies, i.e. lasing modes, are determined by the eigen-modes of the fixed laser cavity. Typically, in a fiber ring laser with fixed ring length of l, the cavity mode spacing can be calculated by c/nl, where c is the light velocity in vacuum and n is the refractive index of the fiber. Provided that a specific gain profile is given, lasing would occur at fixed cavity modes where the gain overcomes the loss. In general, such a fixed cavity laser would support multiple longitudinal lasing modes as long as gain is high enough and no filtering techniques with narrow bandwidth are implemented.

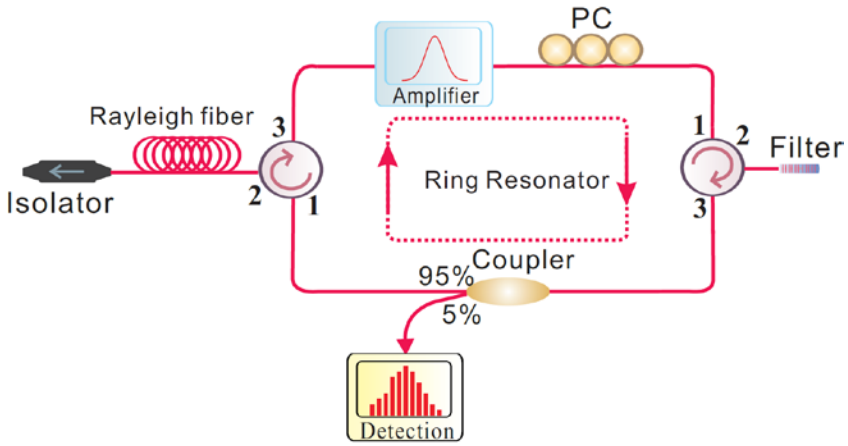

Figure 3-13. Schematic of a random fiber ring laser with Rayleigh feedback.

Situations are different in random fiber lasers with random distributed feedback from numerous disordered scattering centers. Figure 3-13 shows a schematic of a random fiber ring laser with Rayleigh feedback. An optical fiber amplifier provides the gain, which could be based on the SBS process, SRS process and EDF with spectral profile tailored by a filter. Random distributed feedback is provided by the long Rayleigh fiber, which could be regarded as a collection of scattering centers randomly distributed along the fiber. The elastic Rayleigh scattering feedback, which preserves the phase coherence between the incoming and scattered light waves, leads to coherent random feedback with constructive interference. The random lasing builds up through the combination of the coherent Rayleigh scattering in the Rayleigh fiber and round-trip amplification by the optical gain. Note that the intra-cavity light in the lasing system experiences the coherent Rayleigh backscattering from different ensembles of scattering centers in the Rayleigh fiber every round-trip during the lasing build-up process. Hence the effective laser cavity length is not constant for the random fiber resonator every round-trip, which physically means that the photons recaptured in the open cavity follow complex and various trajectories, while the phase correlation among them results in multiple and complex interference peaks. Therefore, non-periodic interference

patterns and randomly resonant spikes in the lasing spectra are expected due to the random distribution of the optical path length for arbitrary backscattered lights. If the polarization effect and the phase noise terms are omitted, the lasing output from the proposed random fiber laser could be expressed as

$$E_{out} = \sum_{m=1}^{M} E_S \prod_{u=1}^{m} \exp(-\alpha L - i\frac{2\pi \upsilon n L}{c}) \sum_{k=1}^{N(u)} G_{u,k} A_{u,k} \exp(-2\alpha z_{u,k} - i\frac{4\pi \upsilon n z_{u,k}}{c}). \qquad (3.16)$$

where E_S is the seed light from the amplifier, which could be Brillouin Stokes light, Raman Stokes light or amplified spontaneous emission from EDF; L is the length of the loop excluding the length of Rayleigh fiber; α and n are the mean loss coefficient and refractive index, respectively; M is the total number of round-trips; $G_{u,k}$ is the gain experienced by the backscattered light from kth scattering center in uth round-trip; $A_{u,k}$ and $z_{u,k}$ are the backscattering coefficient and position of kth scattering center in uth round-trip, respectively; $N(u)$ is the total number of effective scattering centers in uth round-trip and increases with the number of round-trip times; v is the frequency of the light.

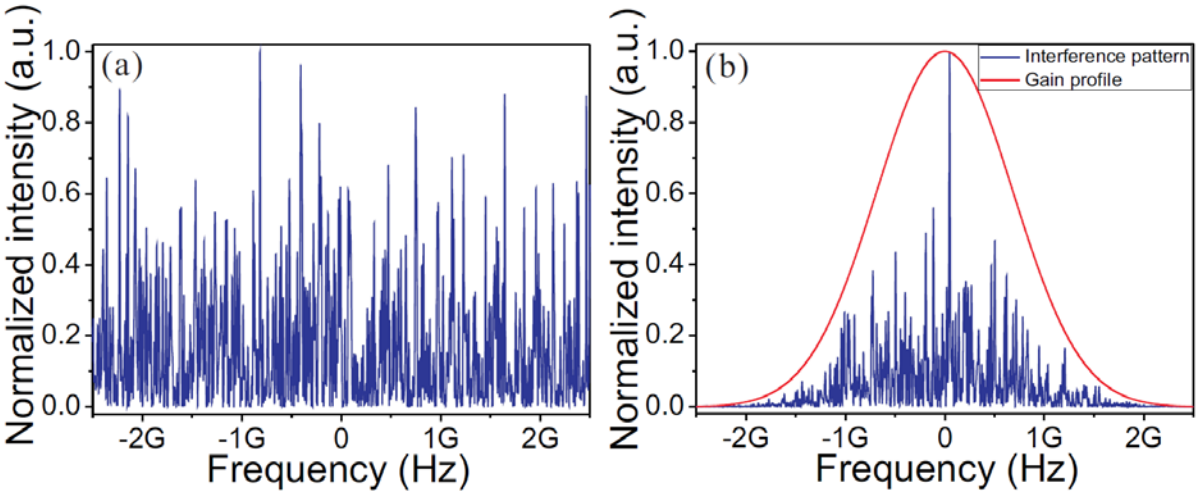

Figure 3-14. Resonance properties of random fiber ring laser with (a) flattened gain and (b) un-flattened gain.

Assume there are 1000 scattering centers in a 5km long Rayleigh fiber and the locations of

these reflectors are uniformly distributed along the fiber, the resonance properties of the random fiber ring laser with flattened gain profile and un-flattened gain profile are calculated using Eq. (3.16) as shown in Figure 3-14. When a flattened gain profile is adopted for the random fiber laser, the resonant mode structure introduced by the random distributed reflectors is shown in Figure 3-14 (a). It is clearly illustrated that unlike the periodically spaced resonant modes in fixed cavity ring lasers, the random fiber ring laser presents quasi-continuous mode structure, which is attributed to the densely and randomly spaced reflectors in the Rayleigh fiber. When numerous scattering centers along the Rayleigh fiber were considered, the number of random resonant modes is so huge that mode-less resonant outcome could be expected. The dense resonant modes would result in severe mode competition and mode hopping effect in the presence of a flattened gain profile. If an un-flattened gain curve is applied in the laser cavity, resonances will preferably occur at frequency positions where gain overcomes the loss as shown in Figure 3-14 (b). Other cavity modes at frequencies where the gain is not enough to compensate the loss will be suppressed for lasing. Thus such a random fiber ring laser could operate, with high probability, in single mode emission. It should also be noted that the frequency location of the dominant resonant mode depends on the distribution of the random reflectors along the Rayleigh fiber as well as the reflection coefficient of each reflector. Once the external disturbances impinge the Rayleigh fiber, both the distribution and reflection level of the scattering centers will be influenced and changed, leading to the drift of the dominant resonant frequency. Therefore it is crucial to protect the Rayleigh fiber from the external disturbances with careful packaging in soundproof box to mitigate the mode hopping effect. Another effective method is replacing the long Rayleigh fiber with the random fiber media with enhanced Rayleigh feedback, in which the scattering centers are more stable and less sensitive to the

environment changes. Thus, the intensity and frequency noises are alleviated, ensuring high-efficiency and linewidth narrowing laser output.

3.3.2 Linewidth characterization

Linewidth characterization of random fiber lasers could be conducted by employing the delayed self-heterodyne (DSH) method. The DSH technique was firstly proposed by T. Okoshi in 1980, in which a part of the laser output itself was frequency-shifted and used as the local oscillator power combined with the other part of laser output after time delay [91]. This technique has afterwards been widely and extensively applied in linewidth characterization of semiconductor lasers. Modifications and optimizations for simplifying the experimental configurations and improving the measurement resolutions are also made on this technique later, which include reflection-type DSH technique [92] and DSH technique with recirculating delay [93]. Here we will focus on the conventional DSH technique and clarify its operation principles.

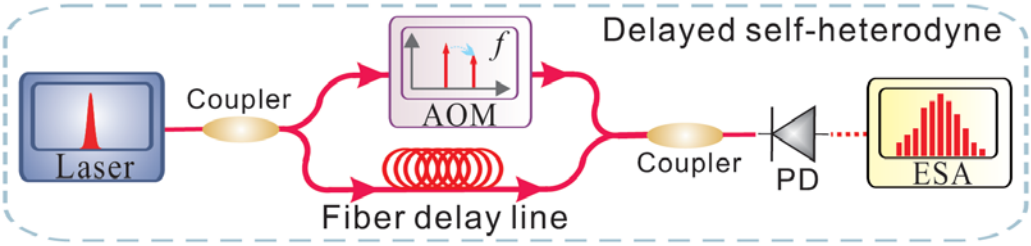

Figure 3-15. Schematic of the delayed self-heterodyne technique for laser linewidth measurement.

The conventional DSH technique is based on the Mach-Zehnder interferometer (MZI) as shown in Figure 3-15. Light from the laser under test is unequally split into two parts with different powers and launched into the two beams of the MZI. As a long fiber delay line is usually required for characterization of narrow-linewidth lasers, the part of light with higher power should be sent through the beam with fiber delay and the other part of light with lower

power launched to the beam with frequency shifter. In this way, the two beam lights could be combined with almost equal powers at the second optical coupler. The mixed signal would therefore be detected by the photo-detector and electrical spectrum analyzer (ESA) with an optimized contrast. In practical operations, an optical attenuator could be inserted into either beam of the MZI for fine control of the transmitted light powers.

The optical field from the laser under test could be modeled as a quasi-monochromatic amplitude-stabilized field with a phase variation as follows:

$$E(t) = Ee^{j[\omega t+\phi(t)]}. \tag{3.17}$$

When the two light beams combine at the output of the MZI, the detected total field is a superposition of the laser fields as expressed in Eq. (3.17) with a time delay for one and frequency shift of itself for the other:

$$E_T(t) = E_1 e^{j[(\omega_0+\Omega)t+\phi(t)]} + E_2 e^{j[\omega_0(t+\tau_d)+\phi(t+\tau_d)]}. \tag{3.18}$$

where E_1 and E_2 are the field amplitude for each light beam, respectively; ω_0 is the center angular optical frequency; Ω is the frequency shift; τ_d is the time delay induced by the long fiber delay line; $\phi(t)$ and $\phi(t+\tau_d)$ are the initial and time-delayed phase fluctuations, respectively. Because of the square law of optical detectors, these interferometric systems are able to convert the quantum phase noise of the laser field E_T into intensity noise and then give a spectral spread of photocurrent $I(t)$. For stationary fields, the autocorrelation function $R_I(\tau)$ of the photocurrent depends only on the intensity correlation function of the detected total field [94, 95]:

$$R_I(\tau) = qRG_E^{(1)}(0)\delta(\tau) + R^2 G_E^{(2)}(\tau). \tag{3.19}$$

with

$$G_E^{(1)}(0) = \left\langle E_T(t)E_T^*(t)\right\rangle. \tag{3.20}$$

$$G_E^{(2)}(\tau) = \left\langle E_T(t)E_T^*(t)E_T(t+\tau)E_T^*(t+\tau)\right\rangle. \tag{3.21}$$

where q is the electron charge; R is the detector sensitivity; $\delta(\tau)$ is the Dirac delta function. $G_E^{(1)}(0)$ and $G_E^{(2)}(\tau)$ are the first-order and second-order optical intensity correlation function, respectively. By combining Eq. (3.18) and Eq. (3.21), we have

$$G_E^{(2)}(\tau) = \left\langle \begin{array}{l} (E_1 e^{j[(\omega_0+\Omega)t+\phi(t)]} + E_2 e^{j[\omega_0(t+\tau_d)+\phi(t+\tau_d)]})\bullet \\ (E_1 e^{-j[(\omega_0+\Omega)t+\phi(t)]} + E_2 e^{-j[\omega_0(t+\tau_d)+\phi(t+\tau_d)]})\bullet \\ (E_1 e^{j[(\omega_0+\Omega)(t+\tau)+\phi(t)]} + E_2 e^{j[\omega_0(t+\tau_d+\tau)+\phi(t+\tau_d+\tau)]})\bullet \\ (E_1 e^{-j[(\omega_0+\Omega)(t+\tau)+\phi(t)]} + E_2 e^{-j[\omega_0(t+\tau_d+\tau)+\phi(t+\tau_d+\tau)]}) \end{array} \right\rangle. \tag{3.22}$$

The above equation could be simplified as

$$\begin{aligned} G_E^{(2)}(\tau) &= (E_1^2+E_2^2)^2 + E_1^2E_2^2 e^{j\Omega\tau}\left\langle e^{j[\phi(t+\tau_d+\tau)-\phi(t+\tau_d)]}\right\rangle + E_1^2E_2^2 e^{-j\Omega\tau}\left\langle e^{j[\phi(t+\tau_d+\tau)-\phi(t+\tau_d)]}\right\rangle \\ &= (E_1^2+E_2^2)^2 + 2E_1^2E_2^2\cos(\Omega\tau)\left\langle e^{j[\phi(t+\tau_d+\tau)-\phi(t+\tau_d)]}\right\rangle \end{aligned}. \tag{3.23}$$

By using the following well-known relation [96]:

$$\left\langle e^{\pm j\Delta\phi(t,\tau)}\right\rangle = e^{-\frac{1}{2}\left\langle\Delta\phi^2(\tau)\right\rangle}. \tag{3.24}$$

Eq. (3.23) could be expressed as

$$G_E^{(2)}(\tau) = (E_1^2+E_2^2)^2 + 2E_1^2E_2^2\cos(\Omega\tau)e^{-\frac{1}{2}\left\langle\Delta\phi^2(\tau)\right\rangle}. \tag{3.25}$$

where

$$\Delta\phi(\tau) = \phi(t+\tau_d+\tau) - \phi(t+\tau_d). \tag{3.26}$$

By assuming the mean-square phase jitter in Eq. (3.25) increases linearly with the time delay as

$$\left\langle\Delta\phi^2(\tau)\right\rangle = 2\gamma|\tau|. \tag{3.27}$$

where 2γ is the angular full linewidth at half maximum of the Lorentzian laser field spectrum. Eq. (3.25) could thus be written as

$$G_E^{(2)}(\tau) = (E_1^2 + E_2^2)^2 + 2E_1^2E_2^2\cos(\Omega\tau)\bullet\begin{cases} e^{-\gamma\tau}, |\tau| < \tau_d \\ e^{-\gamma\tau_d}, |\tau| > \tau_d \end{cases}. \tag{3.28}$$

By virtue of the Wiener-Khintchine theorem, the spectrum of the detected photocurrent is given by performing a Fourier transform of Eq. (3.19):

$$S_I(\omega) = \int_{-\infty}^{\infty} R_I(\tau)e^{-j\omega\tau}d\tau\,. \tag{3.29}$$

If the shot noise term of Eq. (3.19) is omitted, the two-sided spectrum is written as

$$S_I(\omega) = R^2\left\{\begin{array}{l}(E_1^2 + E_2^2)^2\delta(\frac{\omega}{2\gamma}) + E_1^2E_2^2e^{-2\gamma\tau_d}\delta(\frac{\omega-\Omega}{2\gamma}) + E_1^2E_2^2e^{-2\gamma\tau_d}\dfrac{1/\pi}{1+(\frac{\omega-\Omega}{2\gamma})^2} \\ \bullet[e^{2\gamma\tau_d} - \dfrac{\sin(\frac{\omega-\Omega}{2\gamma})2\gamma\tau_d}{\frac{\omega-\Omega}{2\gamma}} - \cos(\frac{\omega-\Omega}{2\gamma})2\gamma\tau_d]\end{array}\right\}. \tag{3.30}$$

If the time delay meets the following relation that the two beam lights are not coherent

$$\tau_d \gg \frac{2\pi}{\gamma}\,. \tag{3.31}$$

Eq. (3.30) could be written as

$$\begin{aligned} S_I(\omega) &= R^2\left\{(E_1^2 + E_2^2)^2\delta(\frac{\omega}{2\gamma}) + E_1^2E_2^2\frac{1/\pi}{1+(\frac{\omega-\Omega}{2\gamma})^2}\right\} \\ &= R^2\left\{(E_1^2 + E_2^2)^2\delta(\frac{\omega}{2\gamma}) + E_1^2E_2^2\frac{(4\gamma/2)^2/\pi}{(4\gamma/2)^2 + (\omega-\Omega)^2}\right\} \end{aligned}. \tag{3.32}$$

In this case, the beat spectrum has a Lorentzian shape and its FWHM (=4γ) is twice the laser's FWHM (=2γ). Eq. (3.31) requires the delay line long enough in order to obtain the FWHM of the laser under test from a Lorentzian spectrum. However, it is difficult to meet this requirement especially for narrow-linewidth lasers in practical as the delay line should be at least longer than 200km for a 1kHz linewidth laser. In this case, the obtained beat

spectrum is not exactly a Lorentzian shape, leading to some measurement errors. For the linewidth characterization of random fiber lasers, due to the instability of the lasing modes, the beat spectrum from the DSH technique is actually an averaged result over the long delay time induced by the fiber delay line. As a result, the instantaneous linewidth of the random fiber laser cannot be observed and would be smaller than that obtained from the DSH method. This could be improved by employing the heterodyne detection method, which no longer utilizes the beating between the laser output and itself, but rather builds up two identical lasers under test and mixes them together with frequency shift. In this way, as long as the two lasers are independently operating and have no phase correlation, the instantaneous linewidth could be determined directly without using long fiber delay lines.

3.4 Intensity noise measurement

Intensity noise is a key parameter for evaluating the performance of a laser. Laser intensity noise originates from both the quantum noise and technical noise sources. Quantum noises are associated with laser gain and resonator losses. Technical noise sources include the vibration of resonator mirrors, noise of pump lasers, thermal variations in gain medium. A fundamental limit to the intensity noise is given by shot noise, which is related to the discreteness of photons and electrons. It was originally thought to arise from the random occurrence of photon absorption events in a photo-detector. However, it was proved later that shot noise is also closely related to the light field itself. Shot noise level can be approached by most lasers at high noise frequencies well above the relaxation oscillation frequencies. The technical issue induced intensity noises usually dominate in the relatively low frequency region, which could be characterized by recording the power variations of the laser in the time domain.

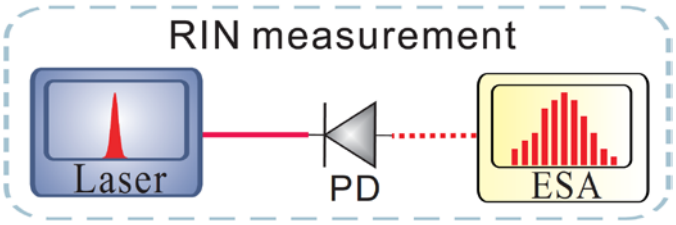

Figure 3-16. Schematic of the RIN measurement setup.

Since the laser intensity noise is usually linearly proportional to signal optical power, it is more precise to normalize the intensity noise by the total laser output power. Thus the parameter, relative intensity noise (RIN), is defined as the ratio between the noise power spectral density and the total output power. Figure 3-16 shows the block diagram of a RIN measurement setup. Output from the laser under test is directly detected by a wideband DC-coupled photo-detector and the detected signal is analyzed in an ESA. Alternatively an oscilloscope could be used to record the time series of laser output and the data can be processed manually. Without intensity noise in the laser under test, there is obviously only a DC component on the ESA spectrum. When the intensity noise is present, the power fluctuation of the laser induces the variations of detected photocurrent, the spectral density of which is measured by the ESA. Because of the square-law detection principle of the photo-detector, the electrical power P_{PD} generated at the output of a photo-detector is proportional to the square of the received laser power P_{out}. Therefore, the RIN can be defined as the ratio between noise power spectral density and the signal power in the electrical domain as follows:

$$RIN(\omega)=\frac{1}{P_{out,ave}^2}\int_{-\infty}^{+\infty}\left\langle (P_{out}(t)-P_{out,ave})\bullet(P_{out}(t+\tau)-P_{out,ave})\right\rangle e^{-j\omega\tau}d\tau\,. \qquad (3.33)$$

where $P_{out,ave}$ is the averaged output power of the laser under test. In practice, the ESA directly measures the photocurrent spectral density, which is denoted as $S_P(\omega)$. If the detector

responsivity is *R*, the measured RIN can be obtained as

$$RIN(\omega) = \frac{S_P(\omega)}{R^2 P_{out,ave}^2}. \tag{3.34}$$

The unit of RIN is Hz^{-1} or dB/Hz as a relative measurement.

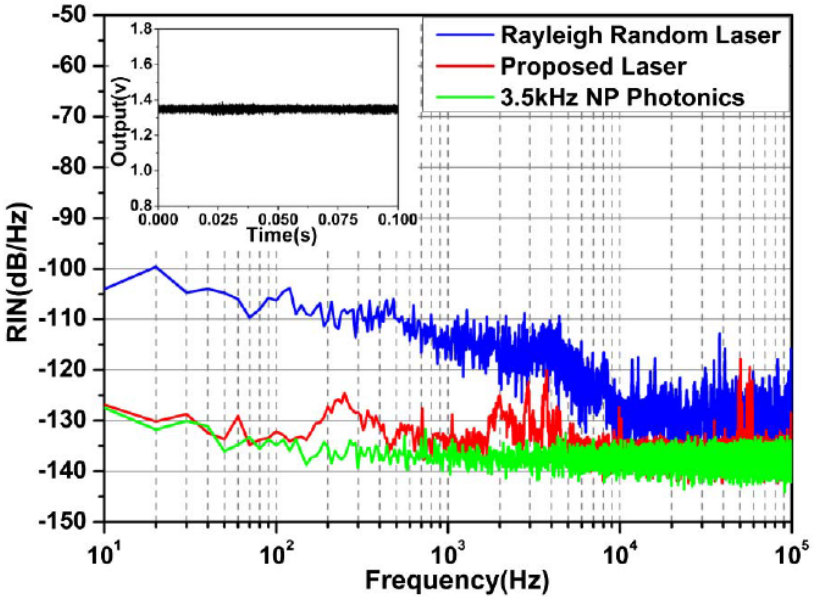

Figure 3-17. RIN comparison between half-open linear cavity Rayleigh random fiber laser (blue), half-open ring cavity random fiber laser with random grating feedback induced by CO_2 laser (red), and commercial fiber laser (green). [75]

Stable single-mode semiconductor lasers usually have very low RIN level below -155dB/Hz in the low frequency spectral range, which is mainly attributed to the stable cavity with thermal feedback control, single-mode operation without mode competition and mode hopping effect as well as high frequency feature of gain dynamics. However, in random fiber lasers, due to several negative factors, the RINs are relatively higher than the conventional semiconductor or fiber lasers. Figure 3-17 shows previously reported RIN measurement results comparing random fiber lasers and commercial fiber laser. The higher RIN in random fiber lasers is mainly due to the random distributed feedback mechanism based on Rayleigh

scattering or enhanced Rayleigh scattering, which does not support a fixed cavity mode but rather large numbers of quasi-continuous modes. This introduces severe mode competition and mode hopping in the laser system when mode locking mechanism is not available. In addition, the gain dynamics plays an important role in influencing the RIN. As EDF gain with a decay time in the order of millisecond was used in that work, the relaxation oscillation noises were intensified by the strong mode competition, leading to distinct RIN peaks around kHz range. For Brillouin random fiber lasers, this gain dynamics induced RIN is also observed, which will be discussed in later chapters.

3.5 Frequency noise measurement

Another key parameter for evaluating laser performance is the frequency noise and its measurement has been one of the most attractive subjects of researches in laser and photonics field. An ideal single-frequency laser has stable and unchanged lasing frequency with low frequency noise, which is only subject to quantum noise and exhibits the Schawlow-Townes linewidth. However, due to the laser cavity change and gain variations induced by the external disturbances, in practice lasing frequency will suffer from shift respect to the original resonant frequency. The frequency noise measurement of a laser is used to describe the level of random fluctuations of the instantaneous lasing frequency. A laser with lower frequency noise is more stable with lasing frequency and is usually associated with narrow linewidth.

The optical field from an ideal laser could be modeled as a monochromatic amplitude-stabilized field with a phase variation as follows:

$$E(t) = E_0 \cos(2\pi \upsilon_0 t) . \tag{3.35}$$

If the time-dependent phase fluctuations are considered, the above equation should be modified as

$$E(t) = E_0 \cos(2\pi\upsilon_0 t + \phi(t)) = E_0 \cos(\Phi(t)). \tag{3.36}$$

The instantaneous optical frequency of the laser could be obtained by calculating the time derivative of the total phase $\Phi(t)$ in Eq. (3.36) as follows:

$$\upsilon = \frac{1}{2\pi}\frac{d\Phi(t)}{dt} = \upsilon_0 + \frac{1}{2\pi}\frac{d\phi(t)}{dt} = \upsilon_0 + \Delta\upsilon(t). \tag{3.37}$$

where $\Delta v(t)$ is the time-dependent frequency fluctuation. The frequency noise could be obtained by computing the power spectral density of the time-dependent frequency fluctuation:

$$S_\upsilon(f) = \Im(\langle \Delta\upsilon(t)\Delta\upsilon(t+\tau)\rangle) = \int_{-\infty}^{\infty} \langle \Delta\upsilon(t)\Delta\upsilon(t+\tau)\rangle e^{-j2\pi f\tau} d\tau. \tag{3.38}$$

The fundamental limit to the frequency noise is determined by the spontaneous emission in the laser gain medium, which also gives rise to the limitation to the laser linewidth, namely, the Schawlow-Townes noise limit. The two-sided frequency noise power spectral density of this limitation is expressed as [97]

$$S_{\upsilon,sp}(f) = (1+\alpha^2) n_{sp} \frac{h\nu_0^3}{Q^2 P}. \tag{3.39}$$

where n_{sp} is the normalized inversion, h is Planck's constant, v_0 is the laser frequency, P is the output power, α is the linewidth enhancement factor, and Q is the quality factor, given by the ratio of the laser frequency and cavity linewidth. An increase in cavity Q and/or laser power P would result in a reduction in $S_{v,sp}(f)$. However, this limit cannot be reached by most of laser sources, particularly at low frequencies, due to other noise sources induced by the cavity variations and thermal variations in gain medium.

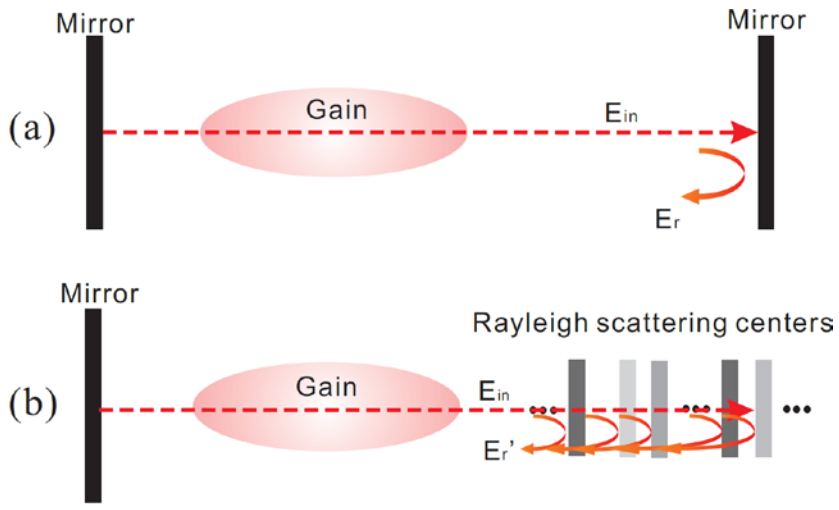

Figure 3-18. (a) Conventional Fabry-Perot resonator with fixed cavity; (b) random fiber laser with random distributed feedback.

In random fiber lasers, the expression of power spectral density of the frequency noise could be derived using the model shown in Figure 3-18. For a conventional FP resonator with fixed cavity as shown in Figure 3-18(a), if the intra-cavity light is E_{in} with optical frequency of v_0, its reflection from the mirror could be written as

$$E_r(t) = E_{in}(t) R_0 e^{j\phi(t-\tau_0)}. \tag{3.40}$$

The frequency noise for the FP cavity can be determined from the delayed phase perturbations contributed by the single reflector and hence can be written as:

$$S_{FP}(\omega) = \Im(\langle \dot{\phi}(t-\tau_0)\dot{\phi}(t-\tau_0+\tau)\rangle). \tag{3.41}$$

Similarly, the reflected light field in random fiber laser with random feedback from N Rayleigh scattering centers as shown in Figure 3-18(b) could be written as

$$E_r'(t) = E_{in}(t)\sum_{i=1}^{N} R_i e^{j\phi(t-\tau_i)}. \tag{3.42}$$

where τ_i and R_i are the delay time and reflection coefficient at ith scattering center. By performing the approximation of $e^x \approx 1+x$ on Eq. (3.42), we have

$$E_r^{'}(t) = E_{in}(t)\sum_{i=1}^{N} R_i[1+ j\phi(t-\tau_i)] = E_{in}(t)\sum_{i=1}^{N} R_i[1+ j\frac{\sum_{i=1}^{N} R_i\phi(t-\tau_i)}{\sum_{i=1}^{N} R_i}] \quad . \qquad (3.43)$$
$$= E_{in}(t)\sum_{i=1}^{N} R_i[1+ j\Phi(t)]$$

Hence, if the phase introduced by the scattering centers is small, we can claim the net phase shift for the random laser to be a statistical average of all the phase shift terms, where each term is weighted by the normalized reflectivity R_i/N. In this case, the frequency noise for the random laser is:

$$S_R(\omega) = \Im(\langle \dot{\Phi}(t)\dot{\Phi}(t+\tau)\rangle) = \frac{\sum_{i=1}^{N}\sum_{k=1}^{N} R_i R_k \Im(\langle \dot{\phi}(t-\tau_i)\dot{\phi}(t-\tau_k+\tau)\rangle)}{\sum_{i=1}^{N} R_i \sum_{k=1}^{N} R_k}. \qquad (3.44)$$

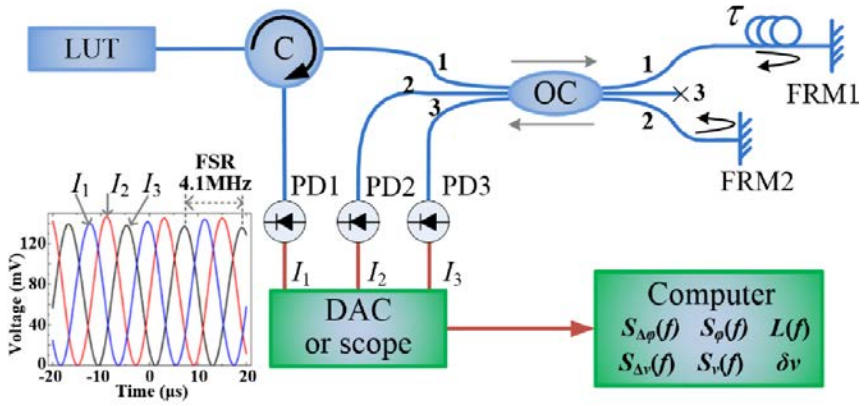

Figure 3-19. Experimental setup used to measure the laser phase and frequency noise [98].

The frequency noise of a laser could be measured using phase demodulation method based on an imbalanced symmetric 3×3 coupler Michelson interferometer (MI) with a delay line in one arm as shown in Figure 3-19. It consists of a commercially available 3×3 optical fiber coupler (OC), a circulator (C), two Faraday rotator mirrors (FRMs), three photodetectors (PDs), a data acquisition board (DAC) or a digital oscilloscope, and a computer. An unbalanced Michelson interferometer is composed of the 3×3 coupler and the FRMs. The

FRM will remove the polarization fading of interferometer, caused by external disturbance on its two beam fibers. The laser under test (LUT) injects the left port 1 of the 3×3 optical fiber coupler through a circulator and then splits into 3 parts by the coupler. Two of them interfere mutually in the coupler after reflected by Faraday mirrors and with different delay times, and the third part of them is made reflection-free. Then the interference fringes are obtained from the left port 1, 2, 3 of the coupler, and read by a DAC or a digital oscilloscope. Following the derivation in [99], the differential phase fluctuation $\Delta\varphi(t)$ of the laser under test accumulated in the delay time τ could be obtained through measuring the three intensity outputs in Fig. 3-19:

$$\Delta\varphi(t)=\varphi(t)-\varphi(t-\tau)=\arctan(\frac{X_2^{'}(t)}{X_1^{'}(t)})-\overline{\arctan(\frac{X_2^{'}(t)}{X_1^{'}(t)})}\quad . \tag{3.45}$$

where $\varphi(t)$ is the instantaneous phase fluctuation of LUT at time t, $X_1'(t)$ and $X_2'(t)$ are expressed as:

$$\begin{pmatrix} X_1^{'}(t) \\ X_2^{'}(t) \\ X_3^{'}(t) \end{pmatrix}=\begin{pmatrix} \eta_1 & \varsigma_1 & \xi_1 \\ \eta_2 & \varsigma_2 & \xi_2 \\ \eta_3 & \varsigma_3 & \xi_3 \end{pmatrix}^{-1}\begin{pmatrix} I_1(t) \\ I_2(t) \\ I_3(t) \end{pmatrix}. \tag{3.46}$$

where $\eta_n=2r_nc_{n1}c_{n2}\cos(\theta'_{n2}+\theta_{21}-\theta'_{n1}-\theta_{11})$, $\varsigma_n=2r_nc_{n1}c_{n2}\sin(\theta'_{n2}+\theta_{21}-\theta'_{n1}-\theta_{11})$, $\xi_n=r_n[(c_{n1})^2+(c_{n2})^2]$, $c_{nm}=p_{mm}b'_{nm}b_{m1}$, n=1, 2, 3 is the output port number of MI, and m=1, 2 is the interference arm port number. p_{mm} is the transmission loss of the interference arm, b_{mn} and θ_{mn} are the splitting ratio and phase delay from the port n to port m of coupler, b'_{mn} and θ'_{mn} are the splitting ratio and phase delay from the port m to port n of coupler, r_n is the responsivity of PDs. So the parameters η_n, ς_n, ξ_n are constant for the setup once the devices and structure are determined. The power spectral density (PSD) of differential phase fluctuation $\Delta\varphi(t)$ and differential frequency fluctuation $\Delta\nu(t)$ can be calculated respectively in the computer by

PSD estimation method [100]. If the calculated phase and frequency noises are denoted as $S_{\Delta\varphi}(f)$ and $S_{\Delta\nu}(f)$, respectively, through the following fixed relations:

$$S_{\Delta\upsilon}(f)=\left(\frac{1}{2\pi\tau}\right)^2 S_{\Delta\varphi}(f). \tag{3.47}$$

$$S_{\upsilon}(f)=\frac{f^2}{4(\sin(\pi f\tau))^2}S_{\Delta\varphi}(f)=\frac{1}{(\sin c(\pi f\tau))^2}S_{\Delta\upsilon}(f). \tag{3.48}$$

The instantaneous frequency fluctuations, i.e. frequency noise, can be expressed as

$$S_{\upsilon}(f)=\frac{1}{(\sin c(\pi f\tau))^2}\left(\frac{1}{2\pi\tau}\right)^2 S_{\Delta\varphi}(f). \tag{3.49}$$

3.6 Applications of random fiber lasers

So far, with the unique lasing feature and simple configurations, random fiber lasers, especially Raman random fiber lasers, have found applications widely extending to various areas including fiber telecommunication applications, remote fiber-optic point sensing systems, and distributed amplification in distributed sensing systems.

In fiber telecommunication applications, the Raman random fiber lasers could be utilized to provide distributed Raman amplification in a long-haul fiber span. The stable lasing output and simple design make the Raman random fiber laser an ideal source for the amplification of ultra-long telecommunication systems without undesired impairment induced by nonlinear effects or compromised signal-noise-ratio with inconstant gain distribution along the fiber length. The forward pumping Raman random fiber lasers have even shown lower effective noise figure than that of bi-directional 1st-order and 2nd-order pumping [101], which provide a new approach to enhance the performance of the amplified signals in long-haul systems with less noise figures.

As a fact, the Raman random fiber lasers have shown stable lasing spectrum with different environmental conditions [102]. In order to apply the Raman random fiber laser in a sensing system, a device with parameter dependence should be introduced into the system as the sensing head. In [102], a remote fiber-optic point sensing system was built up based on Raman random lasing in a half-open cavity composed of a 100km long fiber span and an FBG as point reflector. Meanwhile, the FBG reflector acted as a spectral filter, ensuring the random lasing at a specific wavelength regardless the broad gain spectrum of the Raman scattering. Since FBG is a temperature sensitive device and its Bragg wavelength is shifted as a function of temperature, the lasing wavelength of such a Raman random fiber laser would shift accordingly. By calibrating the lasing wavelength shift with the temperature variation, real temperature at remote end of the long fiber could be quantified. This remote point sensing system is purely passive and far (>100km) from the interrogator, which is an ideal alternative for sensing in harsh environments. Later another remote point sensing system with even longer fiber length (~200km) was reported [103]. Quasi-distributed remote sensing is also available by concatenating a number of FBGs with different Bragg wavelengths [81], which is also possible for simultaneous multi-parameter sensing.

The Raman random fiber laser could also be incorporated into a Brillouin optical time domain analysis system to provide distributed amplification to increase the SNR of the signal for sensing [104]. The reported system allows continuous sensing of temperature over a 122 km fiber span with 2 m spatial resolution and 14°C temperature accuracy. Furthermore, Raman random fiber laser can be incorporated into other types of distributed fiber-optic sensing systems such as the phase-sensitive optical time domain reflectometry. In [105], the sensing range of the system is extended to 175km with the assistance of Raman amplification.

The ultra-long random fiber lasers have led to new promising applications in

telecommunications and distributed sensing as described above. A disordered lasing medium of several hundred kilometers may be also very interesting for potential applications in secure communications, which would give rise to a new type of classical key distribution system that might overcome the practical challenges faced by quantum key distribution systems. The previously reported high-quality Brillouin [86-88] and EDF [75, 106] based random fiber lasers with low noise feature and narrow linewidth could find promising applications in high-resolution spectroscopy, coherent communication, optical sensing, and optical imaging.

Chapter 4 Random Fabry–Perot resonator-based sub-kHz Brillouin random fiber laser and its application in linewidth measurement

This chapter presents the physics, experimental realization, and application of a novel Brillouin random fiber laser. The novel Brillouin random fiber laser is based on the bi-directionally pumped stimulated Brillouin scattering (SBS) in a 10-km-long optical fiber. A random fiber Fabry–Perot (FP) resonator is built up through the pump depletion effects of SBS at both ends of the fiber. A theoretical model is developed to reveal the physics behind the unique random FP resonator that enables narrow random lasing emission. The novel laser is successfully applied for linewidth characterization beyond 860 Hz of light source under test. Section 4.1 gives the background of random lasers, the previously reported Brillouin random fiber lasers and laser linewidth characterization. Section 4.2 introduces the theoretical model of the novel Brillouin random fiber laser. Section 4.3 shows the experimental realization of the Brillouin random fiber laser and its application in laser linewidth measurement. Section 4.4 draws the final conclusion.

4.1 Introduction

Conventional lasers consist of a gain medium that amplifies light and a resonant feedback mechanism, which traps the light to obtain efficient amplification, and determines the

eigenmodes of the laser. As the gain exceeds loss, the active resonator starts to lase. Convention was broken when Ambartsumyan et al. proposed a novel laser with the non-resonant feedback [15] in 1966, where the resonant frequency is only determined by the frequency of the maximum gain. Three decades later the term random lasers, a novel kind of laser action based on phase-coherent multiple scattering and amplification of radiations [17, 107-110], was coined by Wiersma et al. [12]. Light rays penetrating into disordered materials are multiply scattered by wavelength-scale inhomogeneities and follow a random walk, resembling the Brownian motion of particles suspended in a liquid. Meanwhile the light rays are still subject to interference effects thanks to the coherent phase feedback [111], leading to determining emission properties of random lasers such as the central frequency, bandwidth, lifetime and a complex spatial profile. The narrow spikes on the top of an overall narrow emission spectrum have been demonstrated by using a powdered semiconductor such as zinc oxide [19]. Different types of random lasers have been reported using various three dimension (3D) materials such as rare-earth powders [112], human tissues [25], and polymer films with silver nanoparticles [113]. In order to improve the random lasing directionality and efficiency, several types of random fiber lasers were demonstrated recently. An organic dye with nanoparticles was filled into the hollow core of the photonic crystal fiber to form the diffusive random fiber laser [68]. Coherent RFLs were also created by combining Er-doped fiber working as gain medium and distributed Bragg gratings providing random phase feedback [47, 74]. Another random fiber laser based on the Raman amplification and Rayleigh distributed feedback was also reported in [27].

Recently, a Brillouin-gain-based random fiber laser has been demonstrated [86]. The laser is pumped from one end and consists of three different fiber spans that were spliced together. The middle fiber provides high Brillouin gain for the Stokes wave amplification, which is

created by the 3rd section fiber, and the 1st section of the fiber is used to enhance random feedback via the Rayleigh backscattering. Above SBS generation threshold, the Stokes wave starts to lase with spectral width of 3.4 kHz that is 3 orders of magnitude smaller than that of the Brillouin gain profile.

Linewidth characterization has been extensively studied and investigated as narrow-linewidth lasers are massively designed and proposed in many fields such as telecommunications, atomic physics, microwave generations and metrology recently [114-116]. As one of the most important parameters of a laser, laser spectra contain most of the information about the intrinsic laser properties and are commonly regarded as a benchmark for the lasing performance. Conventional diffraction grating based or FPI based optical spectrum analyzers [117, 118] have been found with strong limitations in high-resolution and high dynamic range measurements. Other conventional techniques which transform frequency fluctuations to intensity information based on heterodyne and homodyne detections using MZIs [119, 120] have realized high resolution up to kHz. However, prerequisite conditions such as uncorrelation between the signal and a replica of itself with a modulated frequency or not must be met in order to obtain a precise beating signal without any contributions from coherence. Technical difficulties emerge when a long delay line is inserted for this purpose. This problem worsens especially for narrower lasers where much longer delay line and complex interpretations for delay times become necessary. To overcome the drawbacks of high loss and technical difficulties brought by extremely long fiber delay line, the loss-compensated recirculating delayed self-heterodyne interferometer [121, 122] whose delay line is not required to be longer than the coherence length of the laser under test was developed for narrow linewidth measurement. However, the resultant beating signals are inevitably degraded by the multi-interferences due to the recirculation, and

complicated signal processing methods must be adopted to remove the negative effects. Newly proposed techniques include spectrum analysis based on the SBS effects by either characterizing the amplified Stokes light or utilizing the beating between the amplified narrow Stoke light and the signal under test [123, 124]. They have been reported to achieve a high frequency resolution up to 10MHz limited by the Brillouin gain bandwidth over the whole C and L telecommunication bands. However, cost is raised as extra scanning tunable laser source is needed to reconstruct the spectrum of signal under test. A novel method based of the Brillouin fiber laser (BFL) is later proposed to get rid of the extra laser source [125], which only employs the laser under test itself. The beating spectrum of the build-up BFL and part of the light from laser under test was analyzed with a finer resolution up to kHz which is restricted by the properties of the constructed BFL. The main drawback of possible multi-mode lasing, however, deteriorates the stability of the BFL.

In this chapter, we propose for the first time a novel Brillouin random fiber laser (BRFL) based on bi-directional pumping scheme, which has achieved a lasing output with narrow linewidth of ~860 Hz. A new model of random fiber FP resonator that is built up through the pump depletion effects of SBS and the feedback of Rayleigh backscattering is developed to understand the physics behind the bi-directionally pumped BRFL. Compared with traditional linewidth characterization based on the delayed self-heterodyne (DSH) technique, where 200-km fiber must be used in order to achieve 1-kHz resolution of the linewidth measurement, the proposed extremely simple and compact narrow-linewidth laser provides a new tool for narrow linewidth characterization of less than 1 kHz by using only 10-km fiber.

4.2 Theoretical model

The configuration of the random fiber FP resonator is shown in Fig. 4-1. Two pump lights

$E_{P,A}$ and $E_{P,B}$ with equal power from the same source are launched into the two ends of the optical fiber respectively, which would be scattered from the refractive index fluctuation associated with an acoustic wave of frequency Ω_B, leading to the generation of Brillouin Stokes light that propagates opposite to the pump light and has a frequency downshift of Ω_B with respect to the pump light due to the Doppler effect. The Stokes light $E_{S,A}$ (or $E_{S,B}$) is amplified through the nonlinear electrostriction mechanism along the Brillouin gain fiber. Once pump depletion is triggered with high pump power as the gain parameter $G=gI_P(0)L$ is well above the threshold for SBS, the effective amplification length is no longer the length of optical fiber L but rather determined by $I_s(L_{eff})=I_s(0)/e$ which only accounts for a relatively short length due to the high pump intensity. As a result, most energy of Brillouin Stokes light is stored in both ends of the gain fiber. It is noticed that due to the short interaction length between the first-order Stokes light and the acoustic wave, higher-order Stokes light generation in cascaded SBS process is significantly suppressed. Another co-existing scattering mechanism is the Rayleigh scattering which provides the random phase feedback, leading to the formation of distributed Rayleigh mirrors along the fiber. However, only the Rayleigh mirrors located within the pump depletion regions where Stokes light dominates are capable of offering effective Brillouin Stokes feedback and form two “mirror clouds” at both ends of the fiber as shown in Figure 4-1. Although the reflection coefficient of the distributed Rayleigh mirrors is extremely small (~7.3×10^{-5}/km), the Rayleigh scattered Stokes light at one end is then re-amplified by the pump with a great gain at the other end, leading to the loss compensation. Consequently, the two Rayleigh mirror clouds located at both ends of the optical fiber constitute the random FP resonator.

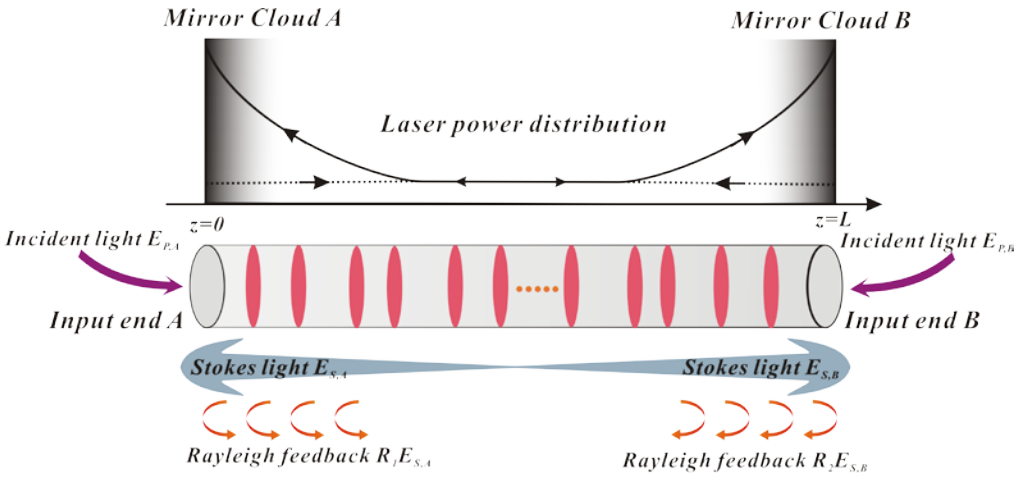

Figure 4-1. Configuration of random fiber FP resonator based Brillouin fiber laser.

Note that the cavity length L_{Ray} is not constant for the random fiber FP resonator and follows a random process statistically with the expected value L_0 which is approximately equal to $2L$ and the standard deviation σ_L. Therefore, non-periodic interference patterns in spectra are expected due to a random distribution of the optical path length for arbitrary round-trip, leading to lasing for some spectral components inside the SBS gain profile. If the polarization effect is omitted, the optical field emitted from the output port A is given by Eq. (4.1):

$$E_{out,A} = \sum_{k=1}^{N} E_{S,A} \prod_{m=1}^{k} e^{-\alpha L_{Ray,m}} G_{A,m} R_{2m} G_{B,m} R_{2m-1} e^{-i2\pi \frac{\nu}{c} n L_{Ray,m}} \tag{4.1}$$

where $L_{Ray,m}$ is the optical path length of m-th round-trip; α and n are the mean loss coefficient and refractive index respectively; $G_{A,m}$ and $G_{B,m}$ are the SBS amplification coefficients for m-th round-trip induced by pump light $E_{P,A}$ and $E_{P,B}$ respectively; R_{2m-1} and R_{2m} are the distributed Rayleigh reflection coefficients in energy-stored regions near port A and port B respectively; ν is the optical frequency and c is the speed of light in vacuum.

The power evolutions of the pump light $P_{P,A}$ and $P_{P,B}$, SBS Stokes light $P_{S,A}$ and $P_{S,B}$ in the gain fiber are given in Eq. (4.2):

$$\begin{cases} \dfrac{\partial P_{P,A}}{\partial z} = -g_B P_{P,A}(P_{S,A} + rP_{S,B} + 2\sqrt{rP_{S,A}P_{S,B}}) - \alpha P_{P,A} + rP_{P,B} \\ \dfrac{\partial P_{S,A}}{\partial z} = -g_B P_{S,A}(P_{P,A} + rP_{P,B} + 2\sqrt{rP_{P,A}P_{P,B}}) + \alpha P_{S,A} \\ \dfrac{\partial P_{P,B}}{\partial z} = g_B P_{P,B}(P_{S,B} + rP_{S,A} + 2\sqrt{rP_{S,A}P_{S,B}}) + \alpha P_{P,B} - rP_{P,A} \\ \dfrac{\partial P_{S,B}}{\partial z} = g_B P_{S,B}(P_{P,B} + rP_{P,A} + 2\sqrt{rP_{P,A}P_{P,B}}) - \alpha P_{S,B} \end{cases} \tag{4.2}$$

where g_B is the Brillouin gain factor; α is the linear loss coefficient and r is the Rayleigh backscattered coefficient.

Table 4-1. Simulation parameters

SBS gain fiber	
Fiber type	SMF28
L (km)	10
g_B ($m^{-1}W^{-1}$)	0.21
α (m^{-1})	$4.4 \cdot 10^{-5}$
r (m^{-1})	$7.3 \cdot 10^{-8}$
$P_{P,A}\|_{z=0}$, $P_{P,B}\|_{z=L}$ (W)	0.035
$P_{S,A}\|_{z=L}$, $P_{S,B}\|_{z=0}$ (W)	$0.66 \cdot 10^{-9}$

Using Eq. (4.2) and simulation parameters listed in Table 4-1, the power distributions of $P_{P,A}$, $P_{P,B}$, $P_{S,A}$ and $P_{S,B}$ along the SBS gain fiber were simulated. As shown in Figure 4-2(a), P_S experiences an exponential growth only in a relatively short length at both ends of the fiber, accompanying with strong depletion effects of P_P. The effective amplification length is calculated around 0.25 km which offers estimations for $L_0 \approx 19.5$ km and $\sigma_L \approx 0.5$ km.

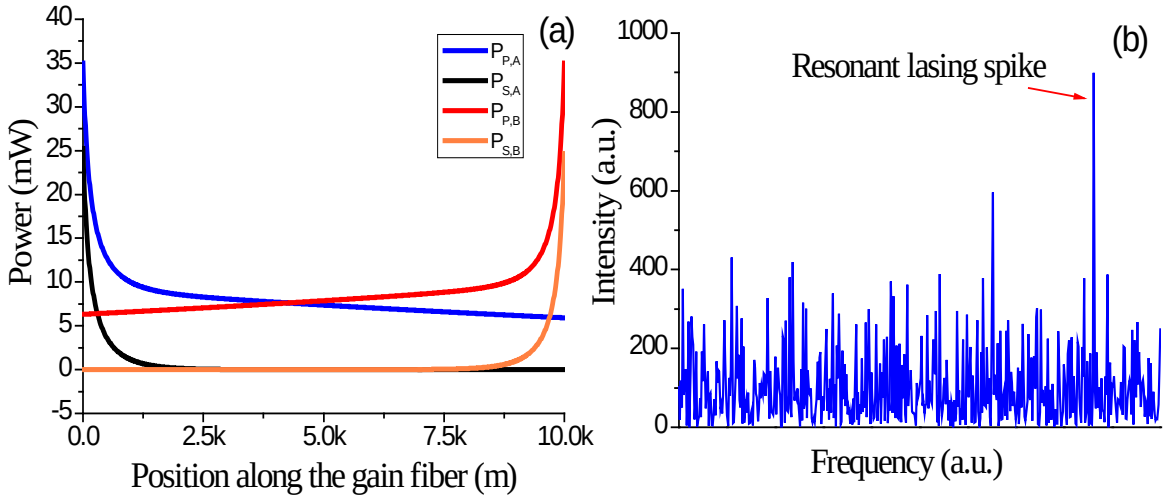

Figure 4-2. (a) Power evolution of pump and Stokes light in SBS gain fiber; (b) Chaotic interference pattern in optical spectra of random FP resonator.

Conventional FP resonators are made of two distinct mirrors with a fixed cavity length, thus resulting with a periodic interference pattern in spectra, while random FP resonators are composed of two “Rayleigh mirror clouds”, that is, the position of each Rayleigh mirror is randomized along time within the pump depletion regions. Figure 4-2(b) shows an example of numerically simulated spectral of a superposition of 100 round trips with random optical path lengths. The simulated spectrum exhibits a chaotic interference pattern and the resonant lasing spike appearing at stochastic positions, indicating the random FP resonator operates in the modeless state. However, if an unflattened SBS gain profile is adopted, the resonant lasing spikes would preferably occur in the frequency region where the Brillouin gain could overcome the total cavity loss, leading to the generation of random lasing behaviour.

4.3 Experimental results

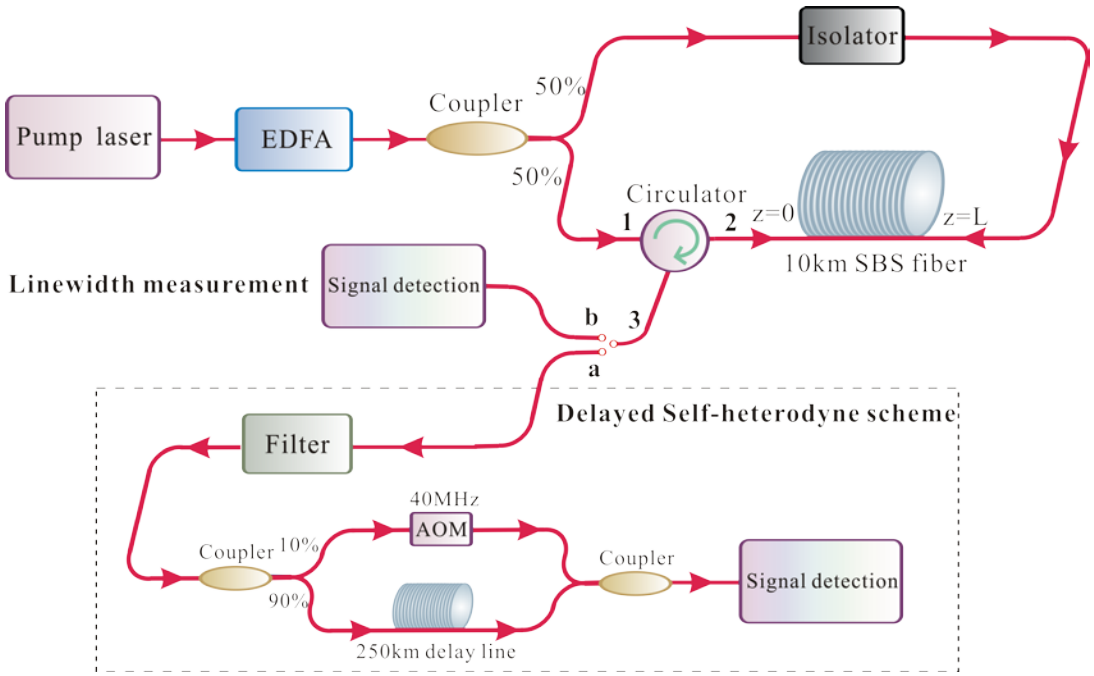

Figure 4-3. Experimental setup of the random fiber FP resonator based Brillouin fiber laser. 3→a: Conventional delayed self-heterodyne method; 3→b: Proposed linewidth measurement method.

The experimental setup of the BRFL is shown in the upper part of Figure 4-3. Light from a 1550nm fiber laser (NP Photonics) with a linewidth of ~3 kHz was firstly amplified by an erbium-doped fiber amplifier (EDFA) and then split into two equal parts by a 50/50 coupler. The bi-direction pumping scheme was built up by launching each part of the light to each end of a 10km long single mode fiber (SMF28) inside an aluminous soundproof box isolating from external disturbance. An isolator was inserted in the upper light path to protect the EDFA from the backward scattered Stokes light. To guarantee a highly pure Stokes lasing output, a narrow optical filter (~3GHz) was used to remove the un-depleted pump light from the output at port 3 of the circulator. The threshold power of the proposed laser was measured to be 10mW for each pump light by varying the amplification magnitude of the EDFA as shown in Figure 4-4(a).

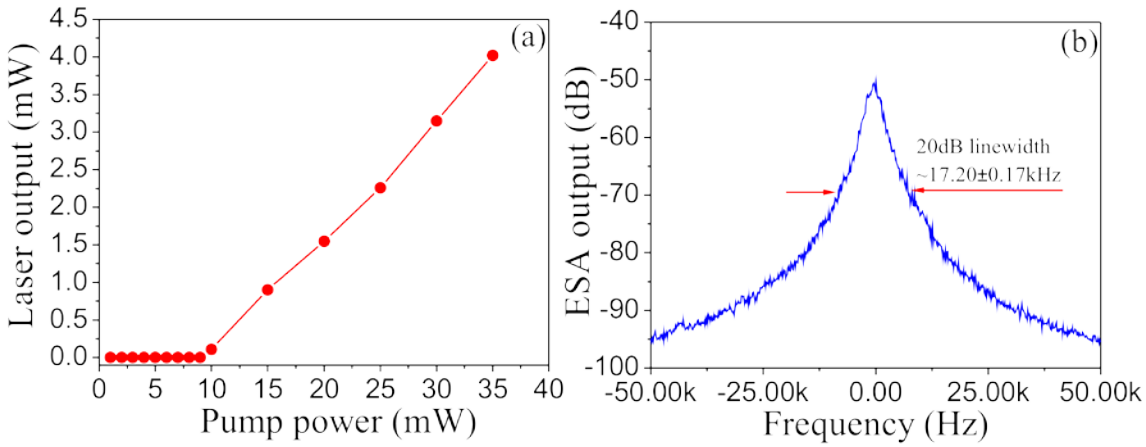

Figure 4-4. Threshold (a) and linewidth measurement result (b) of the proposed BRFL.

It is necessary to characterize the linewidth of the proposed BRFL itself before being applied in linewidth measurement for other light sources. A conventional DSH method was employed by connecting port 3 of the circulator with port a in Figure 4-3. The laser output was divided into two parts by a 90/10 coupler with the larger part launched into the fiber delay line and the smaller part through an acousto-optic modulator (AOM) which downshifted the optical frequency of laser light by 40MHz. A photo detector was put after the recombination of the two light beams to detect the beat spectrum centered at 40MHz, which was observed in an electrical spectrum analyzer (ESA).

The length of the delay fiber is selected with 250km in the linewidth measurement and experimental result is given in Figure 4-4(b). It is illustrated that the 20-dB linewidths of the measurement result is ~17.2±0.17 kHz, which corresponds to 860.0±8.5 Hz for 3-dB linewidth. The resultant narrower linewidth was due to the narrowing effects induced by the random fiber FP resonator that was built up through bi-direction pumped SBS processes at both ends of 10km fiber cavity. Note that the lasing threshold varies with the fiber cavity length which however has little influence on the linewidth of the proposed random laser once the lasing is initiated. Based on aforementioned facts, the proposed BRFLs could be utilized

as an effective reference for measuring linewidth beyond 860 Hz.

Characterizing the linewidth of the pump laser is carried out by connecting port 3 of the circulator with port b in Figure 4-3. Thus the detected signal is the beating spectrum between the depleted pump light and Stoke lasing light centered at 10.87GHz. The powers of depleted pump light and Stokes lasing light are adjusted approximately equally in order to obtain the beat signal with optimal visibility. Due to the unique feature of the random FP resonator induced by pump depletion effect of SBS, the output beat spectrum drifts within a range of several Megahertz, which could be attributed to the following two reasons: 1). The random FP resonator is built up through pump depletion at both ends of the 10km fiber with each mirror cloud extending 250m long within which Brillouin gain could overcome the loss due to Rayleigh backscattering. The pump depletion regions contribute the Rayleigh scattering of the Stokes light dominantly compared with other regions of the fiber. As the Rayleigh mirrors are randomly distributed within the two 250m fiber regions, the phase shift $2\pi nL_{Ray,m}\nu/c$ in Eq. (4.1) induced by any two Rayleigh mirrors located at each end of the fiber varies with time. As a result, the resonance frequency keeps changing as different resonance occurs at different times. 2). The thermally fluctuating refractive index of optical fiber would force the Brillouin gain profile to drift slowly from its original center, which results in the occurrence of coherent resonance at different frequency within drifting range. The thermal drift is estimated within a 2MHz range given that the temperature fluctuation is normally $\pm 1^{o}$C in the lab environment [126].

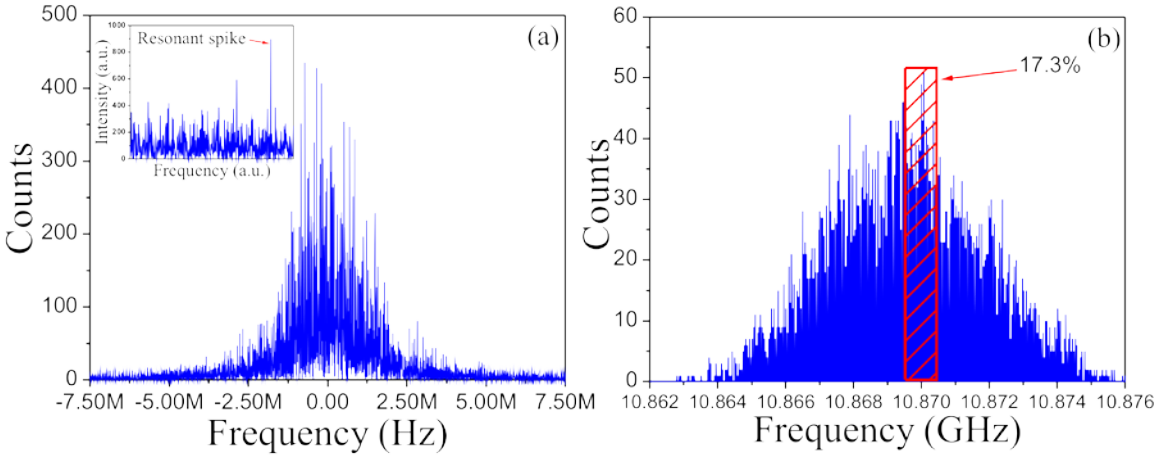

Figure 4-5. Simulated (a) and experimental (b) statistical distribution of the resonating peak positions in 15MHz span; Inset of (a): Chaotic interference pattern in optical spectra of random FP resonator.

The inset of Figure 4-5(a) reveals the random resonance feature of the random FP resonator. The numerically simulated spectrum is a result of a superposition of multiple round trips with random optical path lengths using Eq. (4.1), which exhibits a chaotic interference pattern and the resonance spike appearing at stochastic positions. If an unflattened SBS gain profile is adopted, the resonant lasing spikes would preferably occur in the frequency region where the Brillouin gain could overcome the total cavity loss, leading to the generation of random lasing behaviour. The simulated statistical distributions of the resonating peak positions are shown in Figure 4-5(a). For comparison, experimental frequency jitter measurement was performed by collecting 5500 spectra within a time period of one hour as shown in Figure 4-5(b). It is noted that both distributions generally follow a Gaussian profile but the simulated distribution tends to be more centrally distributed as a result of ignoring the external disturbance which leads to the gain shift. The linewidth measurement was carried out by capturing the beat spectra from ESA within a frequency span of 1MHz centered at 10.87GHz. Following the statistical result from Figure 4-5(b), the probability of the beat signal showing up within the specified span is estimated to be ~17.3%,

which agrees well with the practical operation that one out of 5 or 6 times of single measurements would capture one beat signal. The measurement results are given in Figure 4-6(b) where the linewidth profiles are acquired by averaging over 20 beat spectra to remove undesired noises. To demonstrate the viability and accuracy of the proposed linewidth measurement method, result obtained from conventional DSH method using 100km delay line is listed in Figure 4-6(a) for comparison. The linewidth of the NP fiber laser is measured to be 2.84±0.10 kHz, which agrees well with that acquired from conventional DSH method with a value of 3.00 kHz.

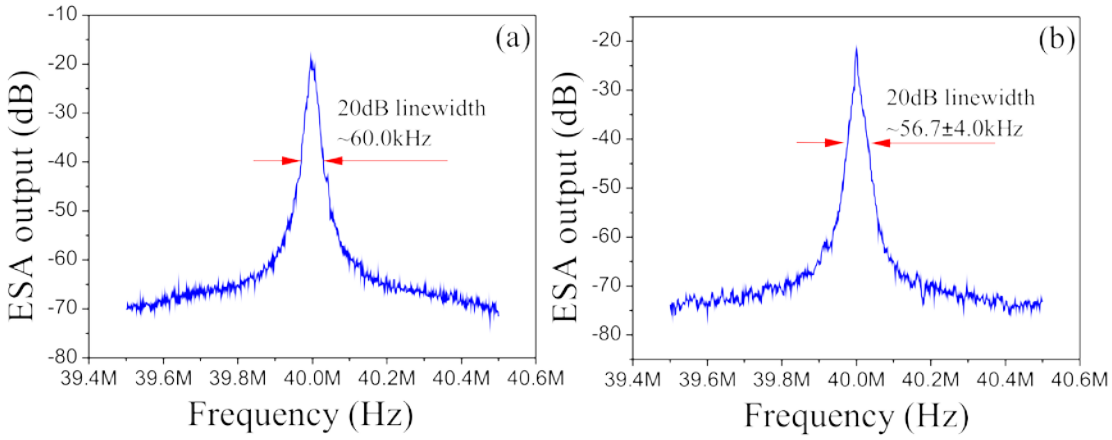

Figure 4-6. Laser linewidth measurements using conventional DSH method (a) and proposed method (b).

4.4 Conclusion

In summary, a novel BRFL is theoretically and experimentally proposed and demonstrated. The random fiber FP resonator is built up through pump depletion effects of SBS based on the unique bi-direction pumping scheme. A novel theoretical model is developed to elaborate the operation mechanism of the proposed random laser. Experimental results show that the proposed laser emits radiation with a narrow linewidth of ~860 Hz and could be effectively

utilized to characterize the linewidth with an accuracy of less than 0.9 kHz.

Chapter 5 Low noise Brillouin random fiber laser with random grating based resonator

This chapter presents experimental realization and characterization of another novel Brillouin random fiber laser (BRFL) with fiber random grating based Fabry-Perot (FP) resonator. Significantly enhanced random feedback from the femtosecond (fs) laser fabricated fiber random grating overwhelms the intrinsic Rayleigh backscattering from the standard SMF, which leads to efficient Brillouin gain for the lasing modes and reduced lasing threshold. Compared with the Rayleigh feedback resonator, the intensity and frequency noises of the proposed random laser are effectively suppressed due to the reduced resonating modes and mode competition thanks to the random grating formed filters. Using the heterodyne technique, the linewidth of the coherent random lasing spike is measured to be ~45.8Hz. Section 5.1 gives the background of different kinds of random fiber lasers. Section 5.2 introduces the experimental configuration and theoretical model of the novel BRFL. Section 5.3 shows the experimental characterization of the BRFL. Section 5.4 draws the final conclusion.

5.1 Introduction

Random fiber lasers distinguish themselves from the conventional counterparts with the presence of disordered and random feedback from either the Rayleigh backscattering induced by the frozen random density fluctuations during fiber fabrication or other artificially

induced random reflectors in optical fibers [27, 47, 74, 127-129]. Gains in such random fiber lasers have been extended using Erbium-doped fiber, Raman amplification and even Brillouin amplification to amply the recaptured randomly reflected light [75, 87, 88, 130, 131]. Based on the properties of the random feedback mechanisms, random fiber lasers could be divided into two categories. When multiple reflections within the random medium only return a portion of energy or intensity of light without the interference effect, this kind of random fiber lasers has been dubbed random fiber laser with incoherent feedback [68, 132, 133]. Previous works such as a Raman random fiber laser based on Raman gain and Rayleigh feedback in an open fiber cavity are the examples of the incoherent random fiber lasers. Provided that a high degree of lasing directionality and high scattering density are present, resonant feedback random fiber lasers could be achieved with sharp spectral peaks associated with high-Q resonances [47, 74, 86]. Examples include a random Er-doped fiber laser with Er-doped fiber gain and randomly distributed Bragg gratings and BRFLs with stimulated Brillouin scattering (SBS) as the gain and Rayleigh scattering as the distributed feedback mirrors. Recently, a novel BRFL with bi-directional pumping scheme was proposed by our group [134, 135], in which stimulated Brillouin scattering (SBS) and the distributed Rayleigh scattering share the same fiber. The fiber sections at both ends providing the highest gain act as the random feedback mirrors and form a random FP resonator. Coherent lasing output with a linewidth of ~860Hz measured by the delayed self-heterodyne (DSH) method was observed on the top of the Brillouin gain spectrum. The mode hopping and competition induced frequency instabilities were also observed, which contributed a lot to the intensity and frequency noises of the proposed random laser.

In this chapter, we introduce a novel random FP resonator formed by two fs laser fabricated fiber random gratings into the BRFL. The random gratings played two roles: 1)

they strongly enhanced the random feedback from Rayleigh scattering process by increasing the index change along the fiber in the order of 10^{-4}-10^{-5}, which is three orders more than that of the Rayleigh scattering in standard single mode fiber (SMF), leading to lower lasing threshold and narrower linewidth; 2) they also act as a superposition of many FP interferometers filtering out some of the random modes and the Brillouin gain is more efficient for the lasing modes. The mitigated mode competition facilitates the BRFL with significant suppression in intensity and frequency noises. The linewidth of the proposed laser characterized by a heterodyne method was revealed to be ~45.8Hz.

5.2 Experimental configuration and theoretical model

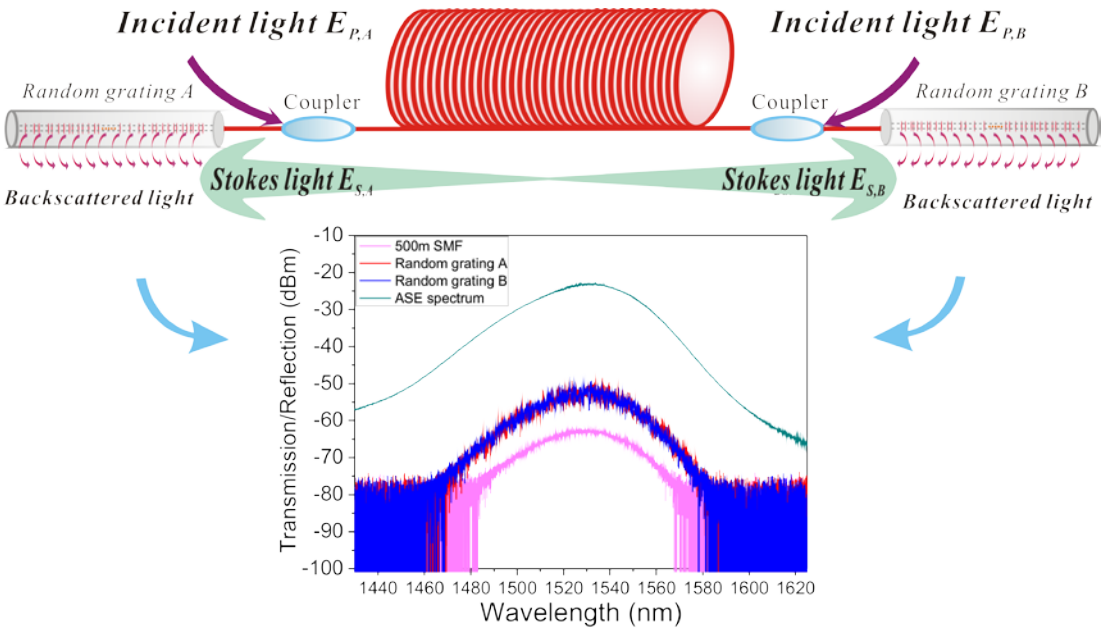

Figure 5-1. Configuration of BRFL with random grating based FP resonator and reflection spectra of random grating sample A and B.

The configuration of the BRFL with random grating based FP resonator is shown in Figure 5-1. Two pump lights $E_{P,A}$ and $E_{P,B}$ with equal power from the same laser source are launched into the two ends of the SBS fiber with length of L (=12km) through two couplers,

respectively. Once the threshold of the SBS is reached, the SBS process takes place in both directions. Pump depletion effect will be triggered when the pump power is sufficiently high. Without random gratings, Rayleigh scattering within the effective amplification length near both ends of the fiber will provide the random feedback of the Brillouin Stokes light and the re-captured Stokes light will be re-amplified by the pump from the other side. Thus the fiber sections within the effective amplification length will act as the random feedback mirrors and form the random FP resonator [134]. When the two random gratings each with length *l* (=10cm) fabricated as described in [136] are inserted at both ends of the SBS fiber through the coupler as shown in Figure 5-1, the Brillouin Stokes light at both ends of the SBS fiber will be not only reflected through the Rayleigh scattering by the two fiber sections but also reflected by the inserted random gratings. The bottom spectra in Figure 5-1 present a comparison between the reflection spectra of the two random grating samples and 500m SMF, which corresponds to the total effective amplification lengths in our previous work. It is illustrated that the reflection spectra for both random grating samples have been enhanced by more than 10dB compared with the 500m SMF. Thus the random feedback induced by the random grating pair would dominate over the Rayleigh scattering by the fiber sections. In the random grating based FP resonator, around 50000 scattering centers from the random grating samples at each end of the SBS fiber constitute numerous cavity modes within the resonator. These scattering centers induced by the fs laser that are discretely distributed along each 10cm modified SMF. The randomness of these cavity modes come from the random variation in the spacing between the neighboring scattering centers ranging from 0 to 3.5μm. Furthermore, the random variation in the optical path length for each round-trip also contributes to the randomness of the lasing modes even through Rayleigh scattering centers are much denser, however, the random grating has stronger reflection and hence higher Q-

values for the laser than that from the Rayleigh scattering alone competing for the Brillouin gain.

The index modification spots in the random grating could be considered as frozen scattering centers whose feedback amplitudes and locations are randomly distributed along the grating length. The backscattered Stokes light at the input end of the random grating is the summation of all the scattered lights from different scattering centers that provide effective random feedback of the random gratings. The Brillouin Stokes light in one round trip inside the random grating based FP resonator experiences twice of the scattering processes by the two random grating samples and twice of the gain processes by the two input pumps. Therefore, the optical field emitted from the output port could be written as Eq. (5.1):

$$E_{out} = \sum_{k=1}^{m} E_S \prod_{i=1}^{k} e^{-2\alpha L_{\mathrm{Ray},i}} R_{A,i} G_{B,i} R_{B,i} G_{A,i} e^{-i2\pi f n L_{\mathrm{Ray},i}/c},$$
$$R_{A,i} = \sum_{j=1}^{N_A'} A_{A,j} e^{-i4\pi n f z_{A,j}/c}, R_{B,i} = \sum_{j=1}^{N_B'} A_{B,j} e^{-i4\pi n f z_{B,j}/c} \quad (5.1)$$

where E_S is the Brillouin Stokes light; $L_{Ray,i}$ is the optical path length of ith round-trip, which is not a constant value and follows a random process statistically with the estimated value L_0 equal to $2L+2l$ and the estimated standard deviation σ_L equal to the total length of the two random gratings $2l$; m is the possible number of round-trips; α and n are the mean loss coefficient and refractive index, respectively; $G_{A,i}$ and $G_{B,i}$ are the SBS amplification coefficients for ith round trip provided by the two pump lights, respectively; $R_{A,i}$ and $R_{B,i}$ are the effective feedback factors associated with random grating sample A and B, respectively; $A_{A,j}$, $A_{B,j}$ and $z_{A,j}$, $z_{B,j}$ are the effective reflection amplitudes and locations of the N_A' and N_B' scattering centers that provide effective random feedback in each of the two random gratings, respectively; f is the optical frequency; and c is the speed of light in vacuum.

5.3 Experimental results

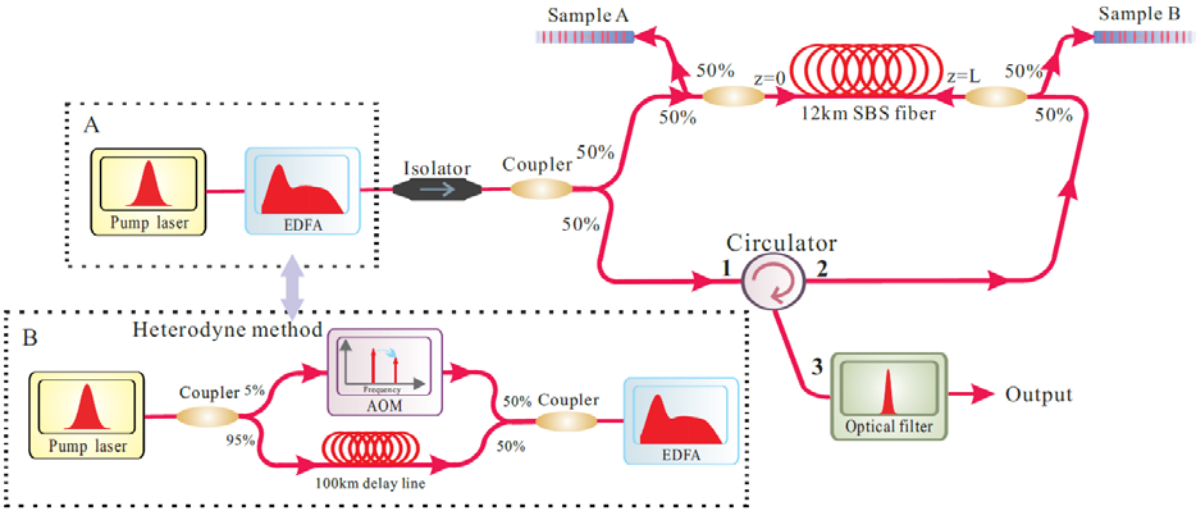

Figure 5-2. Experimental setup of the BRFL with random grating based FP resonator; heterodyne method for linewidth characterization when Part A is replaced by Part B.

The experimental setup of the proposed BRFL is presented in the upper part of Figure 5-2. Light from a fiber laser with 3.5 kHz linewidth (Rock Module, NP Photonics) was amplified by an Er-doped fiber amplifier (EDFA). An isolator is placed after the EDFA to avoid the damage induced by the backflow of the light waves. The amplified pump light was then split into two equal parts through a 50/50 coupler, which were then launched into each end of a 12km long SMF through another two couplers to build up the bi-direction pumping scheme. Random grating sample A and B were connected to the two ends of the 12km SMF through couplers. The 12km SMF as well as the two random gratings were placed inside a soundproof box in order to be isolated from external disturbances. A narrow optical filter (~3GHz) was used to remove the un-depleted pump light from the output of the circulator and make sure pure Stokes lasing output.

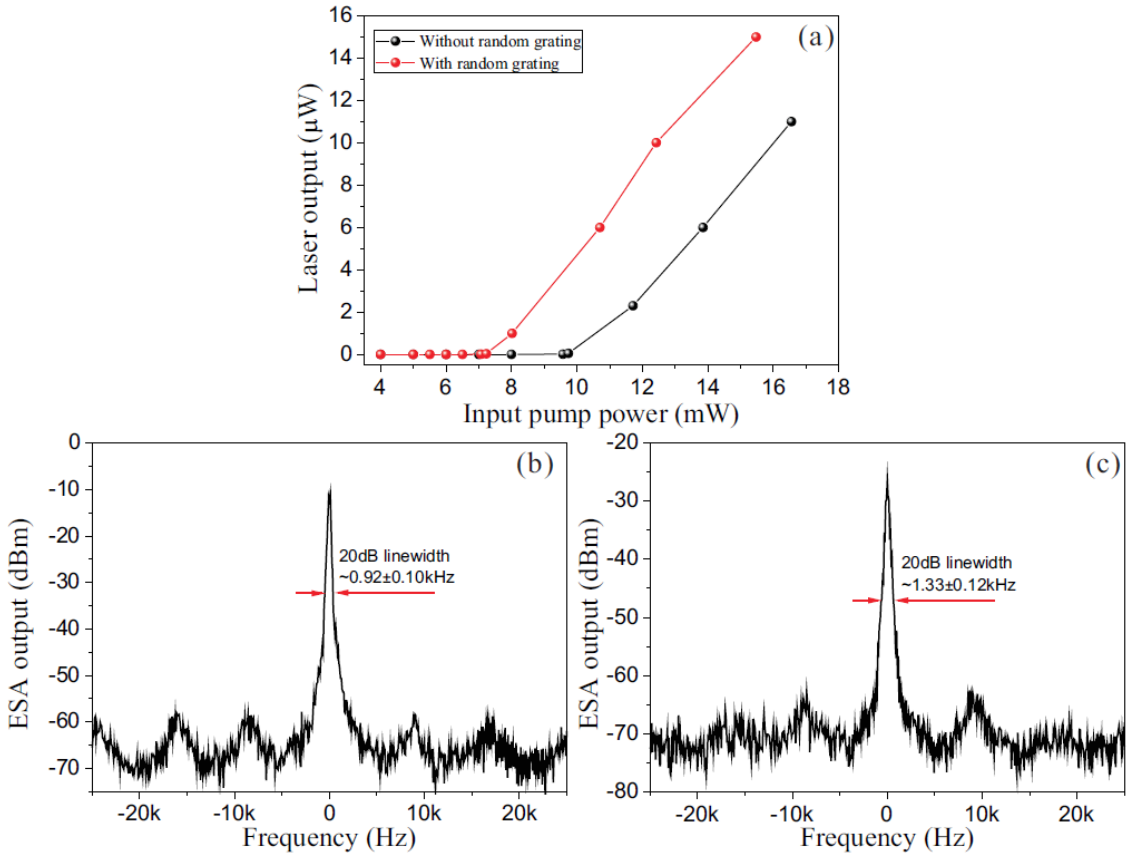

Figure 5-3. (a)Lasing thresholds of the BRFLs with random grating (red) and without random grating (black); Linewidths measured by the heterodyne method for cases with random grating (b) and without random grating (c).

The threshold measurements are conducted by comparing the BRFLs with random grating and without random grating. As shown in Figure 5-3(a) it is noticed that the threshold for the case with random grating based resonator is around 7mW, which is lower by 3mW than that of the case without the random gratings thanks to the significant enhancement of feedback provided by the random gratings. The linewidth of the proposed BRFL with random grating based resonator was characterized by a heterodyne method, which was realized by analyzing the beating spectrum of two BRFLs with the same linewidth but a frequency difference of 40MHz as shown in Part. B of Figure 5-2.

Light from the same fiber laser source was split into two parts by a 95/5 coupler, with the

smaller part sent through an acousto-optic modulator (AOM) with a frequency downshift of 40MHz and the larger part sent to a 100km delay fiber in order to make them uncorrelated. The powers of the transmitted lights in the two arms are adjusted to be approximately equal before being combined and sent to an EDFA. The amplified mixed lights were then launched into the 12km SBS fiber by replacing Part A with Part B in Figure 5-2 and two BRFLs with a frequency difference of 40MHz were generated. Thus the output from the optical filter is the beat signal between the two BRFLs centered at 40MHz. It is also noted that due to (i) the inhomogeneous broadening of the gain spectra along the SBS fiber induced by the material nonuniformity and inevitable vibration and temperature fluctuations that could interrupt the Brillouin gain spectrum of the SBS fiber and (ii) the time-dependent variations in the cavity length for each round-trip induced by the random distribution of the scattering centers of the random gratings, the location of the resonant lasing spike of each BRFL would be randomly distributed within the unflattened Brillouin gain profile at temporal frequency regions where the Brillouin gain surpasses the total cavity loss. Consequently, the beat signal from the two BRFLs was not always exactly located at 40MHz, but kept drifting around 40MHz in a range of about 10MHz, which is within the bandwidth of the Brillouin gain spectrum. In order to characterize the beat signal information, attempts have been made to capture the beat signal within a narrow frequency span in an electrical spectral analyzer (ESA) with a high frequency resolution of 50Hz. Figure 5-3(b)&(c) show the captured beat signals for the BRFLs with random gratings and without random gratings. The contrasts for both cases are approximately 50dB and 40dB, respectively. It is illustrated that the 20-dB linewidths for both cases are measured to be 0.92±0.10 kHz and 1.33±0.12 kHz, which correspond to 46.0±5.0 Hz and 66.5±6.0 Hz for 3-dB linewidth, respectively. Such narrow linewidths could be explained according to ref. [137]: i the threshold for the Brillouin oscillation with weak

external feedback is much lower than that of the single-beam SBS. When the net gain is close to the threshold of the Brillouin oscillation, the Brillouin spectrum has narrowed considerably and more dramatically in the case of longer SBS length. In the Brillouin random fiber lasers with either Rayleigh backscattering fiber based resonator or random grating based resonator, the gain is provided by the Brillouin gain from the 12km long SBS fiber, which could be as large as 60-80dB when 15mW pump is launched with different external feedback. Although the Rayleigh scattering from the two fiber sections only provides about -40dB feedback over 12km fiber, the unique bi-pump scheme is able to compensate this loss by amplifying the Brillouin Stokes light generated by one pump with the other pump within one round-trip. Therefore, the feedback within the resonator is sufficiently high to compensate the loss leading to a high Q value of the random laser and narrow linewidth output [134]. With the random grating based resonator, the feedback is further improved, which results in the increased net gain and narrower linewidth of the BRFL. The delayed self-heterodyne method in the previous work [134] is not used here as the instantaneous linewidth information of the proposed BRFL would be deteriorated by the long delay time introduced by the 250km delay fiber, which results in a time averaged envelope for many random lasing modes measured from the beat spectrum over the delay time.

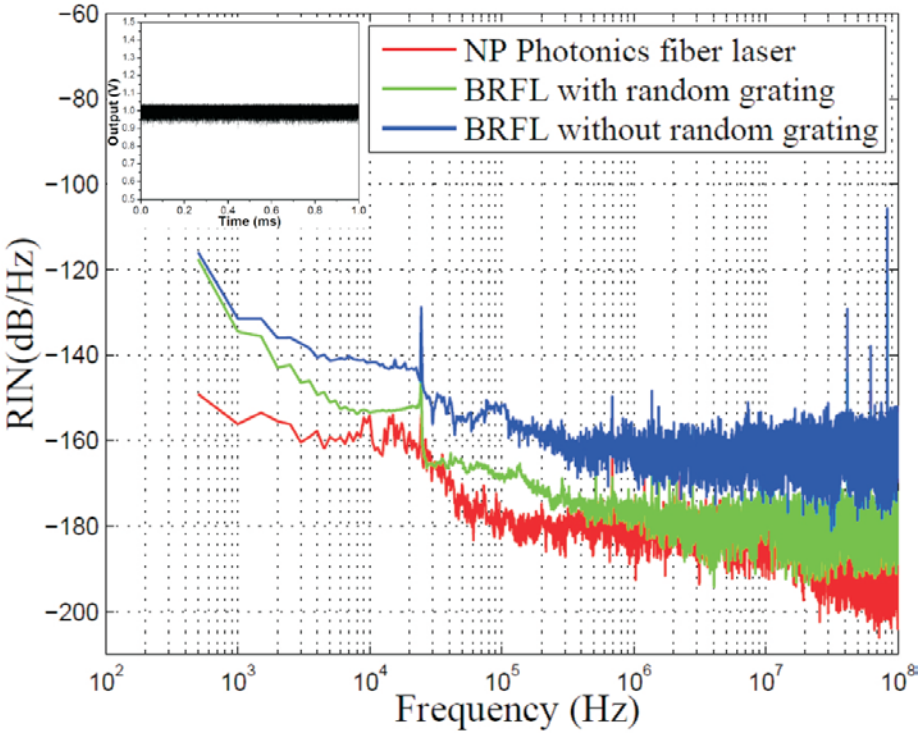

Figure 5-4. RIN of the BRFLs with random grating (green) and without random grating (blue) and the reference fiber laser (red).

The relative intensity noise (RIN) was measured by recording the laser emission with a photo-detector (PDB130C, Thorlabs) of bandwidth from DC to 350MHz connected to an oscilloscope (WaveRunner 64Xi-A, Teledyne LeCroy) and calculating the power fluctuation normalized to the average power level. The inset of Figure 5-4 gives an example of time domain signal of the proposed BRFL output. The constant time domain series indicates the single longitudinal mode operation of the BRFL in the given time period. For comparison, the RIN of the BRFLs with and without random gratings and the commercial NP photonics fiber laser were measured, respectively. It is noted that the RIN of the BRFL with random gratings in the high frequency region beyond MHz is higher than the value of the NP photonics fiber laser but much lower than that of the BRFL without random gratings. This is attributed to the significant decrease in the number of longitudinal modes supported by the

random grating. In the configuration of the BRFL without random grating, the Rayleigh scattering within the effective amplification lengths on both ends of the SBS fiber plays the dominant role in random feedback. Numerous Rayleigh scattering centers with very short and irregular intervals at both sides form a huge number of FP resonators with randomly varying cavity lengths, which leads to a high density of mode numbers within the Brillouin gain bandwidth. Thus the mode competitions and hopping are intensified, leading to high intensity noise. While in the case with random grating based resonator, the number of the index modification spots induced by the femtosecond laser is about 50000, which are discretely distributed along the modified 10cm long SMF. The randomness comes from the random variation between the neighboring modification spots ranging from 0 to 3.5μm. However, the discrete mode structure of the random grating renders fewer randomly distributed scattering centers compared to that of the Rayleigh scattering in SMF, which results in fewer random modes for lasing and thus lower mode density. Therefore, in the BRFL with random grating based resonator, the mode hopping effect within the Brillouin gain bandwidth induced by the mode competition is largely suppressed. It is also noticed that the proposed BRFL shows higher RIN than that of the NP photonics fiber laser in the low frequency range. The BRFL with random grating feedback has a higher sensitivity to the external disturbances such as temperature fluctuations, mechanical vibrations, and acoustic waves, which gives rise to the drift of Brillouin gain spectrum and cavity length fluctuations of the formed random FP resonators at low frequencies, when compared with the NP photonics fiber laser that has included RIN suppression mechanism by temperature control and electronic feedback.

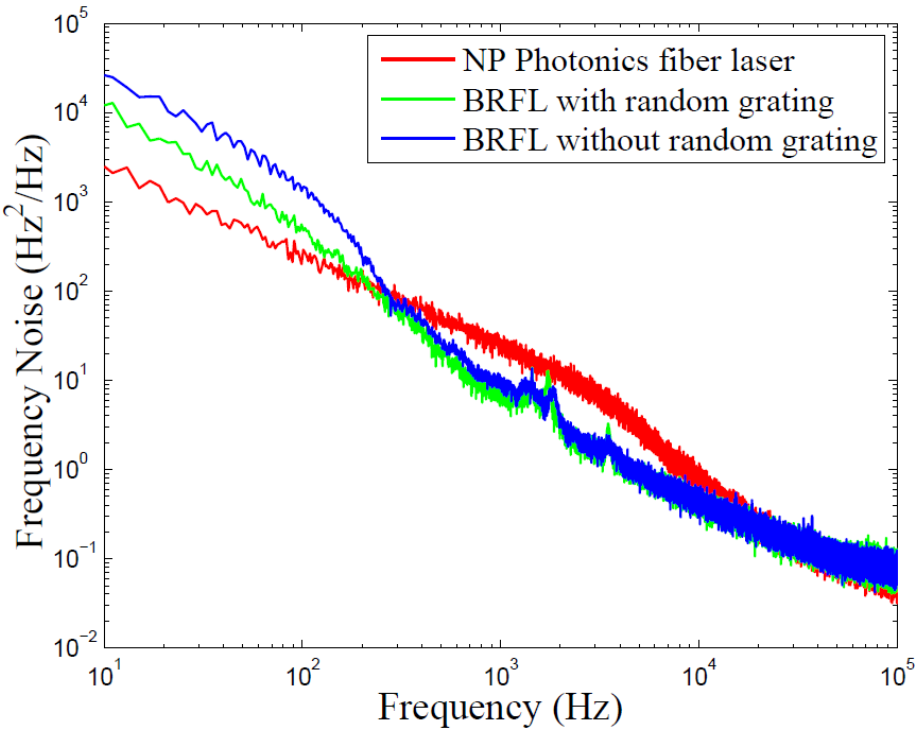

Figure 5-5. Frequency noise spectra of the BRFLs with random grating (green) and without random grating (blue) and the reference fiber laser (red).

The frequency noise measurements were performed with an imbalanced symmetric 3×3 coupler Michelson interferometer, which converts optical frequency fluctuation of the measured lasers into amplitude fluctuation. To ensure that the amplitude fluctuation dominates over all other noises, the imbalance of the interferometer is made sufficiently large by inserting a delay fiber of 4km long into one arm [97]. Two photo-detectors were used to receive the interferometric signals from the two output ports of the interferometer and the recorded data were sent into the Differential-Cross-Multiplication Algorithm [138] at a bandwidth of 100 kHz to extract the phase information of the fiber interferometer.

Using the phase demodulation scheme, the frequency noise spectra of the BRFLs with random grating and without random grating, and the NP Photonics fiber laser were obtained from the interferometric signals, respectively as shown in Figure 5-5. The frequency noise

levels for the BRFLs both surpass that of the reference fiber laser in the low frequency range around hundreds of Hz. The main factors contributing to the higher frequency noise in low frequency domain are the external disturbance induced instability of the cavity length of the FP resonator in the BRFL and the temperature fluctuation induced Brillouin gain drift. Firstly, in the case of the proposed BRFL with resonators formed either by Rayleigh scattering centers or by femtosecond laser induced scattering centers, the resonator mirrors are both randomly distributed within a finite length, which are more easily perturbed by external disturbances in the lab environment compared with the conventional fiber lasers with only two mirrors. The induced randomly varied cavity length of the BRFL modifies the mode structure significantly along the time, which makes the resonance frequency keep changing. Lacking mode stabilization mechanism makes the proposed BRFL suffering higher frequency noise at low frequency range below 0.5 kHz. Secondly, the thermally fluctuating effective refractive index associated with the pump light in the BRFL induced by the surrounding temperature variations compels the Brillouin gain spectrum drifting in a low frequency manner, which is bound to contribute to the frequency noise of the BRFL. It is interesting to note that the BRFL with random gating shows a lower frequency noise than that of the BRFL without the random grating owing to a more compact random grating based resonating cavity which is less sensitive to the external perturbations. Thanks to the long cavity length and randomly distributed feedback in the BRFL, the thermal-induced frequency noise which shows $1/f^{1/2}$ shape in the frequency noise spectrum for the reference fiber laser is largely suppressed [97, 139, 140]. Meanwhile, the phase matching prerequisite imposed by the pump and Stokes waves through the whole lasing process of the BRFL also contributes to the lower frequency noise level in frequency range beyond 0.5 kHz.

5.4 Conclusion

In summary, a novel BRFL constructed by the random grating based FP resonator is proposed and experimentally realized. Comparisons have been made between the proposed BRFL scheme and the previous scheme. The strengthened random feedback from the fs laser fabricated random gratings increases the lasing efficiency and narrows linewidth of lasing spike. With significant suppression in intensity noise and improvement in frequency noise, the proposed BRFL will pave the way for applications in high resolution spectrometers, coherent light sources and optical sensing.

Chapter 6 Multi-parameter sensor based on EDF random fiber lasers with fiber random grating feedback

This chapter presents a novel concept of utilizing erbium-doped fiber random fiber lasers (EDFRLs) to achieve multi-parameter sensing. The experimental configuration, theoretical model, and application of multi-parameter sensing of the EDFRL are described in details. The proposed random fiber ring laser consists of an EDF as the gain medium and a fiber random grating as the feedback medium. The random feedback is effectively realized by a large number of reflections from around 50000 femtosecond (fs) laser induced refractive index modulation regions over a 10cm standard single mode fiber. Numerous polarization-dependent spectral filters are formed and superimposed to provide multiple lasing lines with high signal-to-noise ratio up to 40dB, which gives an access for a high-fidelity multi-parameter sensing scheme. The number of sensing parameters can be controlled by the number of the lasing lines via input polarizations and wavelength shifts of each peak can be explored for the simultaneous multi-parameter sensing with one sensing probe. In addition, the random grating induced coupling between core and cladding modes can be potentially used for liquid medical sample sensing in medical diagnostics, biology and remote sensing in hostile environments. Section 6.1 gives the background of random fiber lasers and their applications. Section 6.2 introduces the experimental configuration and theoretical model of the EDFRL. Section 6.3 shows the experimental realization of the multi-parameter sensing using the EDFRL. Section 6.4 draws the final conclusion.

6.1 Introduction

In optical materials that appear opaque, multiple scattering usually takes place thousands of times in a random fashion for the penetrated light rays before they exit. Based on this type of propagation randomness, random lasers have been extensively studied and researched since the first time the laser action was obtained in disordered structures as proposed by Ambartsumyan, etc. in 1966 [15]. Over the past several decades, random lasers have been observed and demonstrated in various random media [17, 19, 25, 110, 112, 113, 141-143], including crystal powder material, laser dye with nanoparticles, rare-earth powders, semiconductor powder, polymer films with silver nanoparticles and even dye treated human tissues. The unique emission spectra and cost-effective features of random lasers make themselves excellent candidates in applications of environment lighting [144], remote sensing [145], speckle-free imaging [146], document coding [111], and medical diagnostics [25, 147]. The directionality and lasing efficiency of random lasers could be improved and optimized by replacing the disordered medium with optical fibers, namely the random fiber laser. The 1-D optical fiber waveguide provides good confinement in the transverse directions of the light rays trapped inside and effective one-dimension random feedback. RFLs have been realized using Er-doped fiber gain, Raman gain, and Brillouin gain with random feedback induced by Rayleigh scattering [27, 72, 102, 128, 134, 148], or artificially induced randomness such as a photonic crystal fiber filled with a suspension structure [68], Bragg gratings in rare-earth doped fiber [47], and polymer optical fiber [149]. Either in-coherent or coherent lasing outputs have been observed in these random lasing systems, with lasing spectra of bell-shaped peaks as broad as terahertz level [26] or even narrow spikes as sharp as sub-kilohertz [87, 88]. Random fiber lasers based on the Raman gain has been

widely used in many fields, including providing the distributed Raman amplification with lower effective noise and good stability in telecommunication applications [101, 127], remote temperature point-based sensing systems up to 300km [102, 150], and extending the sensing range in the distributed sensing systems [105, 151]. The Brillouin gain based random fiber laser has been utilized in spectral characterization for lasing linewidth measurements [134] as well as random bit generation [135].

In this chapter, a multi-parameter sensor based on the random fiber laser composed of a fiber ring laser with EDF gain and an injection of a fiber random grating is proposed and experimentally demonstrated. The fiber random grating consisting of around 50000 index modification spots induced by fs laser with a randomly varying separation in the scale of several microns provides highly disordered scattering feedback, which could be amplified by the Er-doped gain with wide bandwidth. The resultant sub-nanometer sharp spectral peaks associated with high-Q resonances are utilized for multi-parameter sensing. By controlling the polarization state of the light to be scattered by the random grating, selective modes could be amplified as a result of lasing lines with wide spectral separations. Different from fixed cavity laser that can only support one peak or multiple peaks with integer numbers of longitudinal modes, these multiple lasing lines are contributed by the multiple random modes which originate from different Fabry-Perot (FP) cavities formed by the scattering centers along the random grating sample. Furthermore the randomly distributed refractive index modification spots introduce random birefringence along the sample, making the FP filters polarization dependent. Hence the lasing lines have different strain and temperature dependence due to different index modifications as well as dispersion effects. With the sharp peaks of high-Q value in the RFL, simultaneous multi-parameter measurements could be realized with better resolution compared with the single-pass random grating sensor [136]. In

a previous work where a Raman random fiber laser with multiple lasing lines was achieved based on multiple fiber Bragg gratings (FBG) and Rayleigh feedback from a 22km long optical fiber [81]. Each lasing line is potentially able to be used for sensing depending on the temperature response of the FBG reflectors. However, the proposed random fiber laser based sensor possesses more advantages over the previous scheme such as same sensing head for multi-parameter sensing, higher SNR of the lasing lines, simple and cost-effective fabrication process without the need of phase mask or critical alignment and vibration control in the FBG manufacturing process, higher compactness and lower power consumption.

6.2 Experimental configuration and theoretical model

The experimental setup for the fiber random grating based EDF ring laser is shown in Fig. 6-1. A C-band Erbium-doped fiber amplifier (EDFA) ranging from 1528nm to 1565nm was used as the laser seed and gain medium. The amplified spontaneous emission (ASE) from the EDFA then passed through the isolator and the first polarization controller (PC 1). The isolator was placed next to the EDFA to avoid the damage induced by the backflow of the lasing light and the PC 1 was used to adjust the input polarization of the light before it was sent to the random grating sample through an optical circulator. The enlarged figure shows a schematic drawing of the light scattering in the random grating. The randomly backscattered light from the random grating was guided to another PC followed by an optical coupler with a ratio of 95/5. 95% of the light was sent back to the ring resonator, while 5% was used for detection.

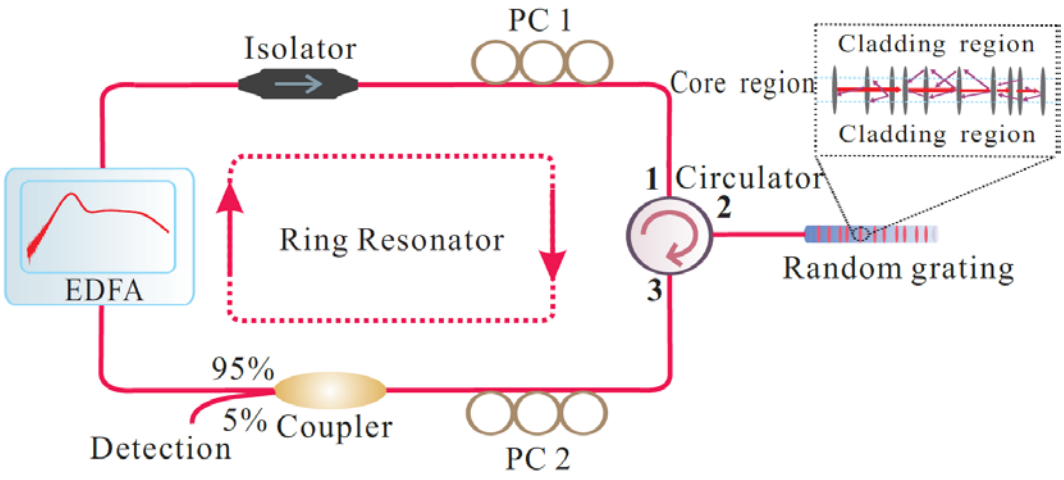

Figure 6-1. The schematic experimental setup of the random grating based Erbium-doped fiber ring laser; the magnified figure is a schematic illustration of the backscattering within the random grating sample; EDFA: Erbium-doped fiber amplifier; PC: Polarization controller.

As shown in Figure 6-1, the distributed backscattered light from the random grating is induced by the randomly distributed scattering centers which are generated by random index modification. These frozen scattering centers could be considered fully deterministic in time, but their amplitudes and locations are randomly distributed. The backscattered light at the input end of the random grating (Port 3 of the circulator) is the summation of all the scattered light waves from different scattering centers. Then the backscattered light is re-amplified by the EDFA and the re-amplified light is once again backscattered by the random grating. The lasing process is established through the interference between lights with different loop trips along the ring resonator. In simulations, only the amplified spontaneous emissions from the EDFA and the light after the first round trip are taken into account for the interference for simplicity. If the amplified spontaneous emissions are denoted by E_{ASE}, the light after the round trip through the random grating could be expressed as

$$E_R = \sum_{i=1}^{N} E_{ASE} A_i \exp(-i\frac{4\pi n z_i}{\lambda}) \tag{6.1}$$

where N is the total number of the scattering centers, A_i and z_i are the reflection coefficient and position of each scattering center, n is the refractive index of optical fiber, λ is the wavelength of the light, c is the light speed in vacuum. The backscattered light is then amplified by the EDFA and re-sent to the random grating sample. Therefore considering the phase term introduced by the light travelling outside the random grating length, the ASE after one loop could be written as

$$E'_{ASE} = \exp(-i\frac{2\pi nL}{\lambda})\sum_{i=1}^{N} GE_{ASE}A_i \exp(-i\frac{4\pi nz_i}{\lambda}) \qquad (6.2)$$

where L is the length of the loop, and G is the gain value provided by the EDFA. It could be seen from the above equations that the amplitude and phase of the ASE after one loop trip are determined by the spectrum of the initial ASE, the position and reflection coefficient of each scattering center, and the loop length. Thus the constructive interference between E'_{ASE} and E_{ASE} can be obtained by computing the product of $\langle E'_{ASE} \cdot E_{ASE} \rangle$. However, when the polarization of the input light is changed by adjusting PC1, the previous set of scattering centers that provide the effective backscattering is no longer effective due to the polarization mismatch. The reflection coefficients and positions of the scattering centers for the input light with new polarization are re-distributed. In this circumstance, both A_i and z_i in the above equations will follow a new random distribution, leading to a brand new spectrum of the light wave after first loop trip.

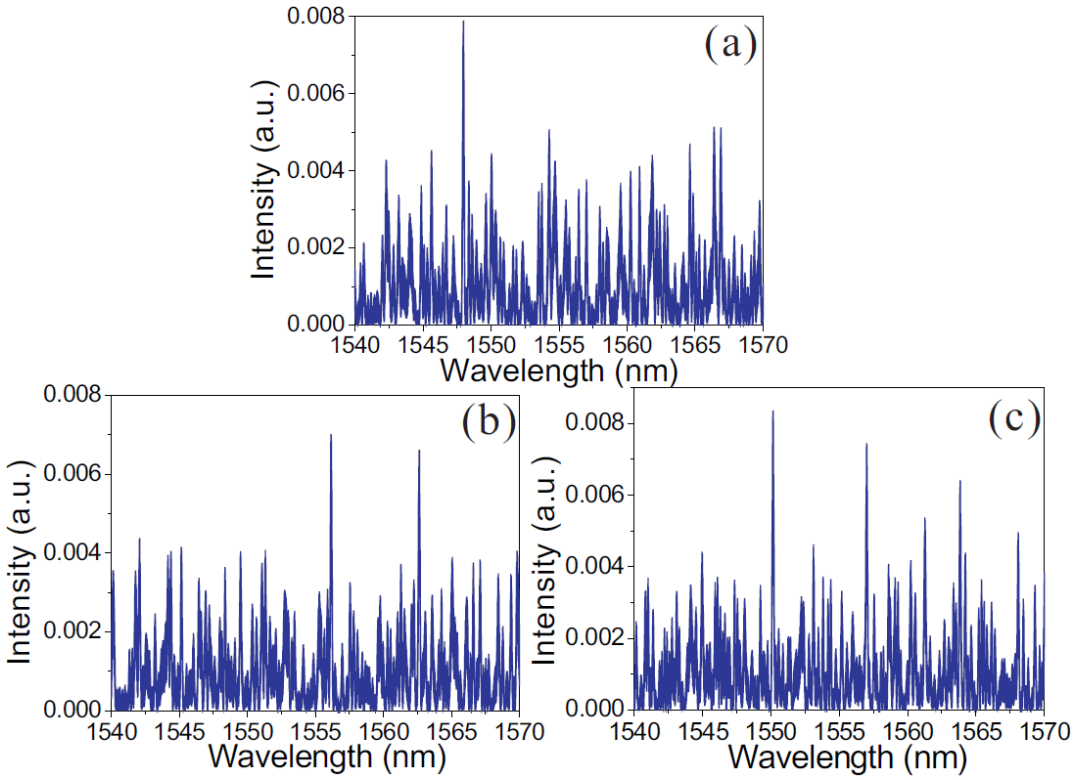

Figure 6-2. Simulated lasing output of the random grating based EDF ring laser with different input polarizations: (a) one lasing line, (b) two lasing lines, and (c) multiple lasing lines.

Figure 6-2 shows the simulated lasing output of the random grating based EDF ring laser with different input polarizations when a flat gain profile is adopted. In the simulations, the length of the loop is set to 50m and around 500 scattering centers were randomly generated along the 10cm long modified SMF. Considering the birefringent effect of the randomly induced index change by femtosecond laser, the polarization influence of the input ASE sent to the random grating sample is simulated by changing the random distribution of the locations and reflection coefficients of the scattering centers. E'_{ASE} is calculated as a function of the spectrum of the ASE based on Eq. (6.2). The interference between the E'_{ASE} and E_{ASE} is computed as shown in Figure 6-2 (a)-(c) with different input polarizations. It is noted that the output lasing lines strongly depend on the random distribution of the scattering centers and the polarization induced re-distribution of the scattering centers. Multiple lasing lines

with large spectral separations could be observed as a result of multiple resonances of the constructive interference between E'_{ASE} and E_{ASE}. Due to the strong mode competitions among these resonant modes induced by the flat gain profile, the contrasts of the resonant modes are comparable and their values are limited compared with the noisy background resonances. As will be shown later, when an unflattened gain profile, i.e. EDF gain, is applied instead, the resonant lasing modes will preferably appear at spectral regions where the gain overcomes loss with high contrasts.

6.3 Experimental results

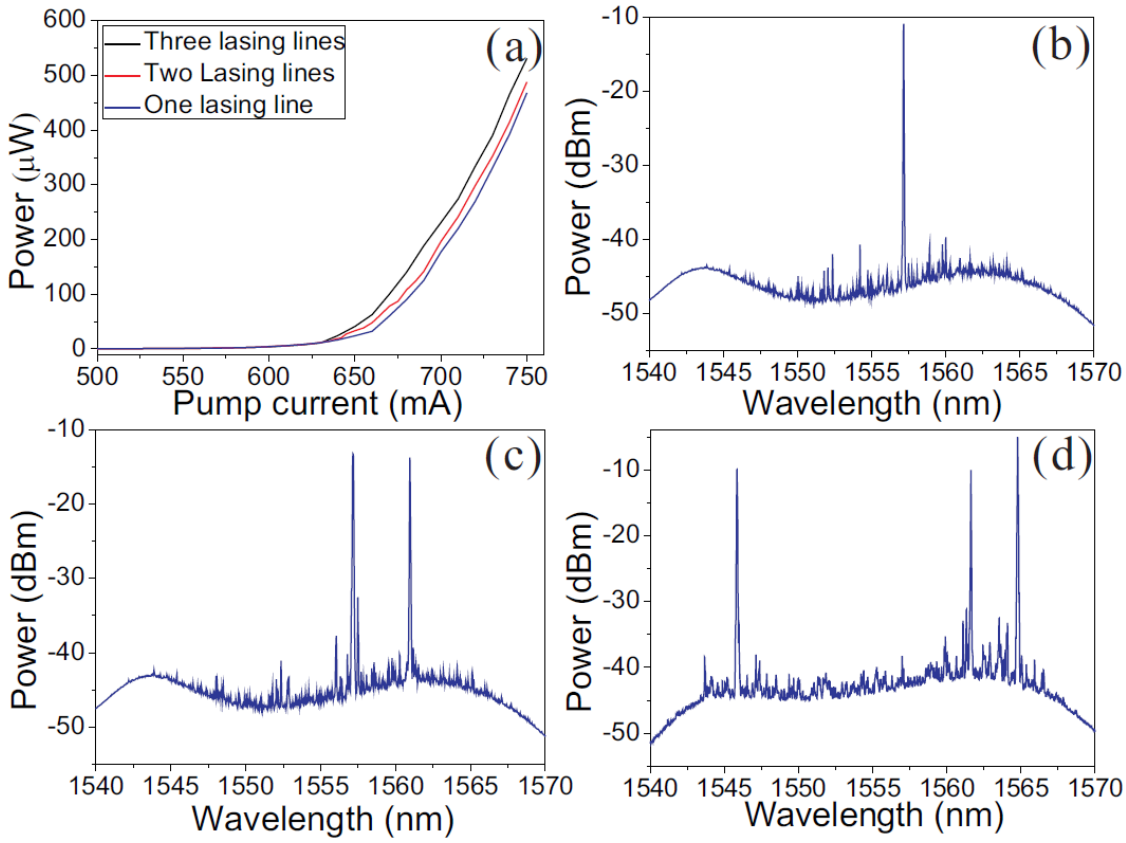

Figure 6-3. (a) Lasing thresholds indicated by the laser output power as a function of pump current for different numbers of emitted lasing lines. Experimental results of the lasing spectra with different input polarizations: (b) one lasing line, (c) two lasing lines, and (d) three lasing lines.

In the experiments, the random grating sample was placed in an aluminous soundproof box to protect the backscattering light from the environmental disturbances. The output power of the EDFA was gradually increased to reach the threshold and activate the ring laser. A portion of the ring laser output from the 5% port of the coupler was sent to an Optical Spectral Analyzer (OSA) for spectrum characterization. The polarization of the input light was adjusted by controlling the PC1. The laser output powers as the function of the EDFA current were plotted in Figure 6-3(a) with different input polarization states. Figure 6-3(b)-(d) show the corresponding measured lasing spectra of the random grating based fiber ring laser with different numbers of lasing lines. The EDFA currents for all cases were set above the threshold values. By changing the input polarization state of the ASE to the random grating sample, the outcome lasing spectra respond with different numbers of lasing lines associated with different random modes. The randomly distributed scattering centers induced by the femtosecond laser micro-machining introduce random birefringence along the fiber and form numerous polarization dependent spectral filters which are superimposed with each other, leading to specific coherent resonant lasing lines. The threshold for more lasing lines has a tendency to decrease. It is also notified that the resonant lasing lines are built up with very high signal-to-noise ratio up to 40dB, which is limited by the gain provided by the EDFA. The separation of these lasing lines could be as large as about 19nm, which is due to the spectral filtering effect of the FP filters formed by the closely separate scattering centers, that is, the resonant wavelength is selected by the polarization-dependent filters. Because of different spacing among the index modification spots, multiple lasing lines selected by different FP cavities have different strain and temperature dependence due to different index modulations at different locations, which gives access to the parameter measurement using the RFL imposed by the random grating feature.

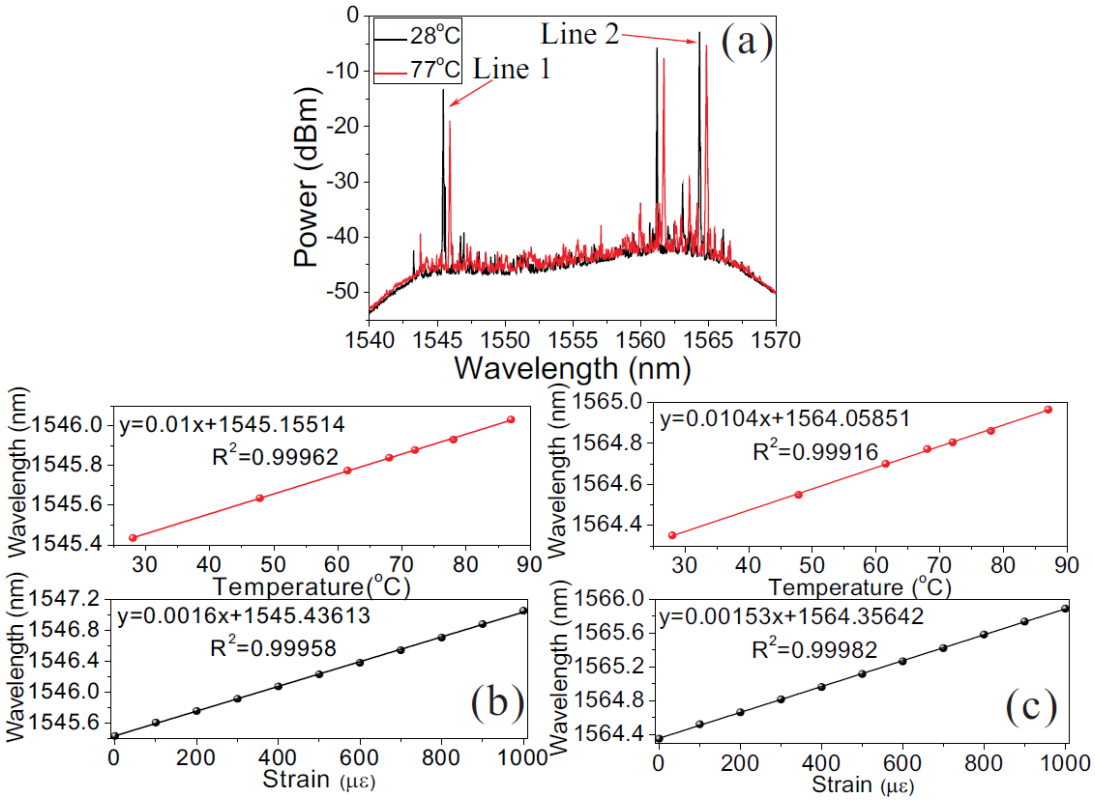

Figure 6-4. (a) Illustration of lasing line shifts as a result of temperature change; wavelength shift calibration results of temperature and strain measurements for Line 1(b) and Line 2 (c).

The wavelength responses of the multiple lasing lines could be utilized for measuring parameters which influence the phase differences of those FP filters formed along the random grating sample. The phase changes are different for FP cavities at different locations and also impacted by external disturbances with different extents at different wavelengths, leading to distinct wavelength shifts among the resultant multiple lasing lines. In experiments, temperature measurements were conducted by placing the random grating sample into an oven. The output lasing spectra at each temperature were recorded when the temperature inside the oven remained stable. To characterize the strain sensitivity of the proposed sensor, the two ends of the random grating were anchored horizontally between a motorized translational stage and a stationary stage. The system is capable of stretching the sensor

longitudinally by controlling the motorized stage along the axis of the random grating with a sequential strain step of 100 με. As shown in Figure 6-4(a), two lasing lines at 1545.4nm and 1564.4nm are selected for monitoring the spectral shifts responding to the temperature and strain variations. It could be seen from the figure that both lines experience significant spectral shifts when the surrounding temperature of the random grating was increased from 28°C to 77°C. It was also noticed that in the experiments the variation in the peak intensities of the lasing lines and generation of extra lasing lines were observed when relatively high temperature or large strain was applied on the sensor. However, if the external disturbances are not so large that the induced refractive index change is quite small compared to the femtosecond laser induced refractive index modification which is in the order of 10^{-4}~10^{-5} in the random grating, the target lasing lines still remain there for the spectral shift monitoring. More details of the temperature and strain measurements are depicted in Figure 6-4(b)(c), in which the wavelength shift-related temperature coefficients for both lasing lines are 10.0pm/°C and 10.4pm/°C and the wavelength shift-related strain coefficients for both lasing lines are 1.60pm/με and 1.53pm/με, respectively.

A character matrix $M_{T,\epsilon}$ is defined to represent the sensing performance of the lasing lines in the random grating based fiber ring laser by

$$\begin{bmatrix} \Delta\lambda_1 \\ \Delta\lambda_2 \end{bmatrix} = M_{T,\varepsilon} \begin{bmatrix} \Delta T \\ \Delta\varepsilon \end{bmatrix} = \begin{bmatrix} C_1^T & C_1^\varepsilon \\ C_2^T & C_2^\varepsilon \end{bmatrix} \begin{bmatrix} \Delta T \\ \Delta\varepsilon \end{bmatrix} = \begin{bmatrix} 10.0 & 1.60 \\ 10.4 & 1.53 \end{bmatrix} \begin{bmatrix} \Delta T \\ \Delta\varepsilon \end{bmatrix} \qquad (6.3)$$

where $\Delta\lambda_1$ and $\Delta\lambda_2$ represent the spectral shift of Line 1 and 2 induced by temperature and strain variations. C_1^T, C_1^ε, C_2^T, and C_2^ε are the temperature and strain coefficients of Line 1 and 2, respectively. The character matrix $M_{T,\epsilon}$ can be used to simultaneously determine the variations in the temperature and strain from the spectral shifts of lasing lines. Error analysis

for the measurement of multiple parameters is given by [67]:

$$\begin{bmatrix} \delta T \\ \delta \varepsilon \end{bmatrix} = \frac{M'_{T,\varepsilon}}{\Delta} \begin{bmatrix} \delta \lambda_1 \\ \delta \lambda_2 \end{bmatrix} \tag{6.4}$$

where δT and $\delta \varepsilon$ are the errors of temperature and strain, Δ is the determinant of $M_{T,\varepsilon}$, $M'_{T,\varepsilon}$, is the adjugate matrix of $M_{T,\varepsilon}$, and $\delta \lambda_1$ and $\delta \lambda_2$ are the errors of the spectral shift of lasing lines. According to the error analysis for simultaneous multi-parameter measurements, the calculated maximum errors of temperature and strain measurements are 2.3^{o}C and 15.2με.

6.4 Conclusion

In summary, a multi-parameter fiber-optic sensor based on random fiber laser has been proposed and experimentally demonstrated. A polarization sensitive random grating fabricated by femtosecond laser micro-machining was injected to an Erbium-doped fiber ring laser, generating multiple high-fidelity lasing lines. By choosing different lasing lines and monitoring their spectral responses to the external disturbances, multi-parameter sensing could be realized. The sensing error is able to be further improved by using gain media with broader bandwidth, so as to yield more distinct responses to the varied parameters. The innovative concept of utilizing the random laser for parameter quantification could be extended to applications in medical diagnostics, biology and remote sensing in hostile environments by substituting the random grating medium with target-oriented materials.

Chapter 7 Highly sensitive fiber random grating based EDF random fiber laser sensor for ultrasound detection

This chapter presents a novel fiber random grating based EDF random fiber laser for highly sensitive ultrasound detection. The configuration of the random fiber laser sensor, lasing characteristics, and ultrasound detection results are described in details. The random fiber laser is constructed with the EDF gain. A fiber random grating provides random distributed feedback for the random laser and acts as an ultrasound sensing head. The random laser can operate in a single-mode lasing scenario, which offers linear and pure temporal responses to the broadband ultrasonic acoustic emission from 20kHz to 0.8MHz. The multiple interfering reflection spectrum of the random grating provides large number of steep peak areas over a broad spectral range, which significantly enhances the sensitivity of the random laser sensor and makes it an ideal sensor in harsh environment with large temperature or strain variations. The proposed laser sensor offers signal-to-noise ratio improvement up to 20dB and higher sensitivity compared with conventional piezoelectric acoustic sensors. Section 7.1 gives the background of ultrasound detection using fiber-optic techniques. Section 7.2 introduces the experimental configuration and operation principle of the EDF random fiber laser sensor. Section 7.3 shows the experimental results of the ultrasound detection. Section 7.4 draws the final conclusion.

7.1 Introduction

Ultrasound detection is a vital and versatile technique, which has been widely researched and utilized in varieties of areas such as structural health monitoring, geophysical exploration, dimensional measurement, material testing, and biomedicine [152-156]. One phenomenal process that generates the ultrasonic waves is the acoustic emission, which is frequently accompanied by damage-related structural changes and gives rise to the release of elastic waves with typical frequency range between 100kHz and 1MHz and strain in the sub-micron/m range [157]. Thus an effective ultrasonic acoustic emission sensor with capabilities of broad bandwidth inspection and high sensitivity is highly desired.

Fiber-optic technique based ultrasound sensors have been extensively investigated and applied with significant advantages, such as immunity to electromagnetic interference, compact footprint, durability, and multiplexing capability over the conventional piezoelectricity based ultrasonic probes. Fiber Bragg gratings (FBGs) are the most commonly used sensing elements in the fiber-optic ultrasound sensors [158-162]. The most straightforward demodulation of the responses of the FBG to the ultrasound is to detect the power of the reflected light from the gratings [163-167]. However, the ultrasound sensors based on the regular FBGs usually suffer from the broad bandwidths of the regular FBGs, which force the sensitivity of the sensor to depend on the slight wavelength dependency of the intensity of the broadband light source [163, 164]. Although the phase-shifted FBG (PS-FBG) has been utilized to realize the ultrasound detection in megahertz [165-167], the narrow peak in the PS-FBG lacks the stability for demodulation due to the environmental change, which requires extra complex configurations such as Pound-Drever-Hall method for stabilization. This problem was solved in [168], but the proposed coherence-restored pulse

interferometry may lack the high sensitivity for ultrasound signals below 4MHz and simplicity due to the relatively complex demodulation schemes. It has been demonstrated that constructing an erbium fiber ring laser (EFRL) incorporated with fiber gratings is able to improve the ultrasound sensitivity owing to the significant power enhancement in the laser ring cavity [169]. However, the relative flat amplified spontaneous emission (ASE) profile of the erbium doped fiber (EDF) and the multi-mode lasing scenario lead to noisy temporal responses, which limit the sensitivity of the laser sensor and the maximum detectable frequency to tens of kilohertz. To solve the problem, a tunable filter is adopted to select the lasing wavelength at the maximum spectral slope region of the Bragg spectrum in order to increase the sensitivity [170], whereas the sensing system does not have high temperature or strain robustness and has limited detectable ultrasound frequency up to 200kHz because of the multi-mode lasing operation. PS-FBG is also incorporated into the EFRL acting as the sensing head, which allows single-longitudinal mode lasing and achieves highly sensitive ultrasound detection utilizing the spectral slope of the reflection spectrum of an apodized FBG (AFBG) [171]. However, this laser sensor is not applicable in harsh environments with high temperature and large strain changes, which may shift the narrow band dip of the PS-FBG out of the reflection spectrum of AFBG and remarkably reduces the sensitivity. The PS-FBG was also used to achieve the polarimetric heterodyning fiber grating laser for ultrasonic detection up to megahertz range [162], however, it lacks high sensitivity in detecting kilo-hertz ultrasound waves due to small birefringence variations induced by the large wavelength acoustic waves.

In this chapter, we present a highly sensitive fiber-optic ultrasound sensor based on the random fiber laser. A fiber random grating is used to provide random distributed feedback for the EFRL and for the first time utilized as the ultrasound sensing head. The effective

suppression of cavity modes owing to the random grating enables the laser sensor with linear response to the ultrasonic acoustic waves over broad frequency range and the multiple interfering reflection spectrum from the random period grating equips the sensor with tremendous number of steep peak areas, by which the sensing system, with high probability, has a lasing mode at a steep region of the reflection spectrum where the sensitivity is the greatest. Thus the random grating eases the setting of the system to its working point and guarantees ultrasound detection with high sensitivity over a broad operating spectral range. The proposed laser sensor exhibits broadband ultrasound response within 0.8MHz frequency range with high signal-to-noise ratio (SNR) without any locking mechanism, which offers a simple solution as an ideal sensor in harsh environment with large temperature or strain changes.

7.2 Experimental configuration and operation principle

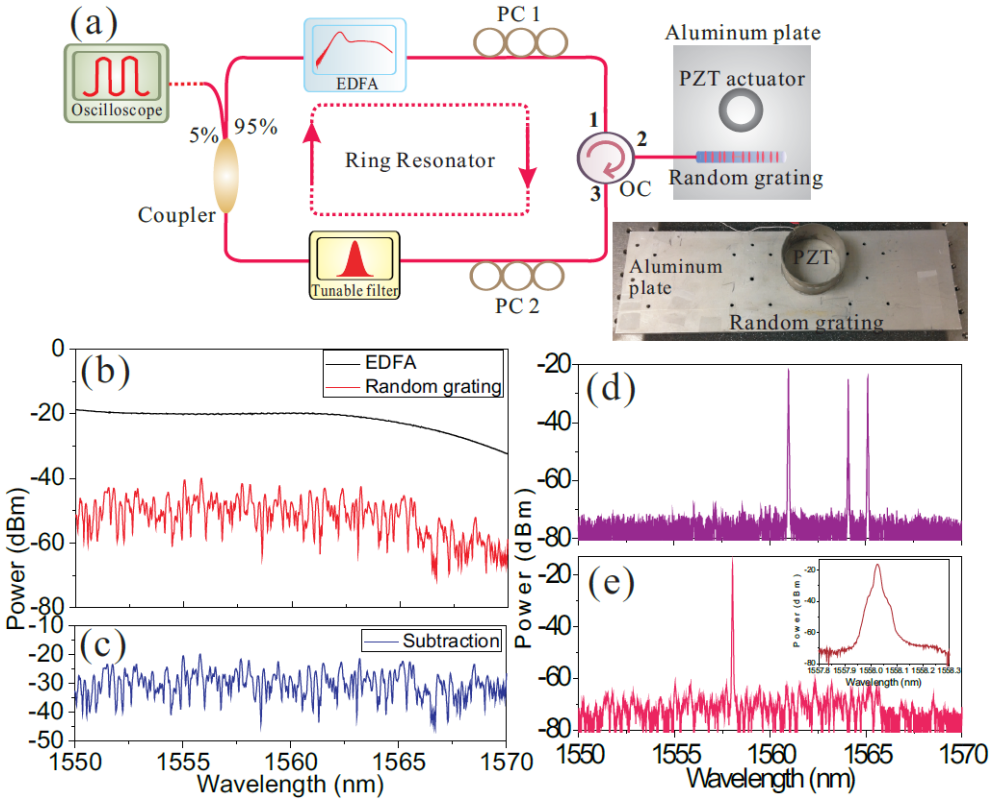

Figure 7-1. (a) Experimental setup of the fiber random grating based random laser sensor for ultrasound detection; (b) EDFA gain profile (Black) and reflected power spectrum from fiber random grating (Red); (c) Reflection spectrum of the fiber random grating; (d) Multi-wavelength lasing spectrum; (e) Single-wavelength lasing spectrum.

The experimental setup of the proposed fiber random grating based random laser sensor is shown in Figure 7-1(a). The random fiber laser consists of a C-band erbium-doped fiber amplifier (EDFA) as the laser seed and gain medium and a fiber random grating providing random distributed feedback, which is realized by a large number of reflections from around 50000 femtosecond laser induced refractive index modulation regions over a 10cm standard single mode fiber [136]. The ASE from the EDFA then passes through the first polarization controller (PC 1) and the optical circulator (OC) to the random grating sample. The random

distributed feedback light from the random grating then passes through PC 2 and a coupler with a ratio of 95/5 and is finally re-amplified by the EDFA. The two PCs are used to adjust the state of polarization (SOP) of the intra-cavity light in order to achieve polarization matching and increase lasing efficiency. Figure 7-1(b)&(c) show the ASE profile of the EDFA and the reflected ASE spectrum from the random grating as well as the subtraction between the two spectra, i.e. the reflection spectrum of the random grating. It is clearly illustrated that the relative flat ASE profile of the EDFA is tailored to multiple interfering spectrum by the random period grating thanks to the superposition of numerous Fabry-Perot interferometers and Mach-Zehnder interferometers formed by the index modification spots, which renders tremendous number of large spectral slope regions for the highly sensitive ultrasound sensing. The proposed random fiber laser is able to lase at multi- or single-wavelength, depending on the SOP of the intra-cavity light and the birefringent properties of the random grating sample [172]. An example of multi-wavelength lasing is shown in Figure 7-1(d). In order to realize highly efficient single-wavelength lasing and take advantage of the multiple interfering spectrum of the random grating for ultrasound sensing, a tunable filter (TF) with 3GHz bandwidth is inserted into the random fiber laser. Figure 7-1(e) gives an example of single-wavelength lasing at 1558nm with the help of the TF.

The ultrasound detection was conducted by bonding the two ends of the random grating sample and the lead zirconate titanate (PZT) actuator onto an aluminum plate with dimension of 320mm×100mm×7mm as shown in the inset photograph of Figure 7-1(a). The random grating was located 1cm away from the PZT actuator and kept straight by pre-stretching during the bonding process. The PZT actuator was driven by a function generator to generate Rayleigh waves that propagate as the acoustic surface wave along the aluminum plate considering that the thickness of the plate is comparable to the acoustic wavelength. Since

only the two ends of the fiber random grating were glued onto the aluminum plate, the generated Rayleigh wave in the aluminum plate, consisting of both longitudinal and shear waves, impinged the random grating in the form of dynamic longitudinal strain. Through the strain-optic effect, the induced change in the refractive index of the random grating sample due to the applied longitudinal strain could be expressed as

$$\Delta n = -\frac{1}{2} n^3 \varepsilon [p_{12} - \upsilon(p_{11} + p_{12})] \tag{7.1}$$

where ε is the dynamic longitudinal strain; p_{11} and p_{12} are optoelastic constants of silica; and v is the Poisson ratio of silica. Strictly speaking the random period of the random grating is also varied in the presence of the acoustic wave through the geometric effect, which, accompanied with the strain-optic effect, would change the optical path lengths of the many interferometers formed inside the random grating sample, leading to the spectral shift of the reflection spectrum. The dynamic strain generated by the PZT actuator in the ultrasonic frequency range is usually in the order of nano-strain, which leads to the spectral shift in the order of femto-meter by recalling that the strain sensitivity of the fiber random grating is around 1.2pm/με [136].

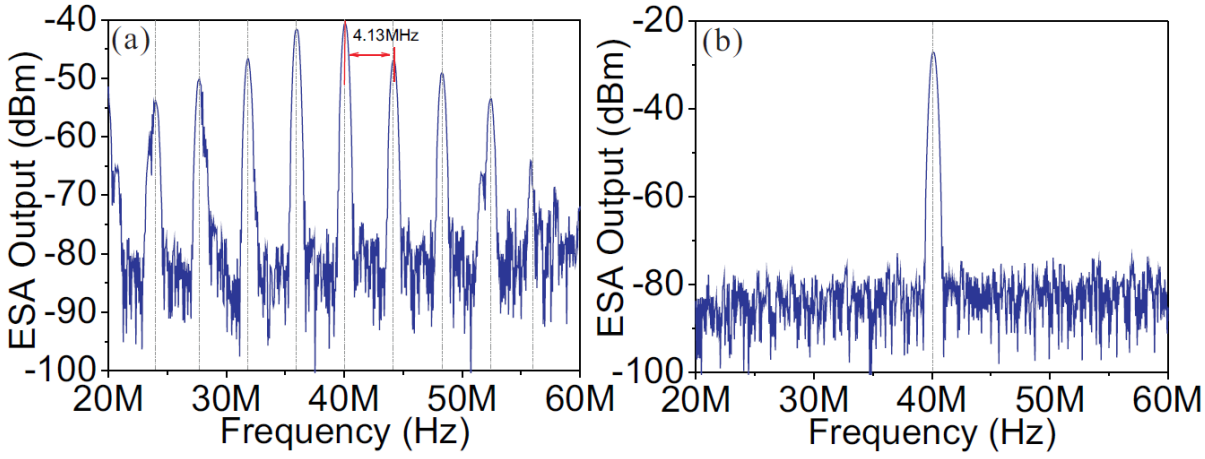

Figure 7-2. Radio frequency spectra of delayed self-heterodyne measurements for lasing output with mirror feedback (a) and random grating feedback (b).

The proposed random fiber laser builds up when the gain generated by the EDFA and tailored by the fiber random grating as well as adjusted by the SOP of the intra-cavity light exceeds the loss in the ring cavity. Due to the narrow bandwidth of the inserted TF and the homogeneous broadening property of the EDFA, single-wavelength lasing is established at the peak wavelength of the TF. Furthermore, the random distributed feedback from the fiber random grating accompanied with the help of the narrow bandwidth of the TF is able to select a small number of cavity modes of the ring cavity from large number of modes within the bandwidth of the EDFA, which suppresses the mode competition and ensures single-mode lasing scenario near the transmission peak of the TF [106]. The narrow single-mode lasing is beneficial to the ultrasound sensing which relies on the loss modulation of the laser ring cavity, resulting in linear and pure time series responses. However, it has to be admitted that as the fiber random grating is not a truly random medium, the contribution of the reflection from each scattering center along the random grating is not equally distributed. Thus the SOP of the light and the gain level of the EDFA should be carefully controlled so as to realize the single-mode lasing. Figure 7-2 shows a comparison of the beating signal results at 40MHz using the delayed self-heterodyne method between the fiber ring laser incorporated with mirror feedback and the random grating feedback. The laser output was divided into two parts by a 50/50 coupler, with one part passing through an acousto-optic modulator which downshifted the optical frequency of the laser light by 40MHz and the other part through an optical fiber delay line that is longer than the laser's coherence length. A photo-detector was put after the recombination of the two light beams by the 2nd 50/50 coupler to detect the beat signal at 40MHz, which was observed in an electrical spectrum analyzer. It is clearly shown in Figure 7-2(a) that multi-longitudinal mode lasing could be easily observed in the mirror feedback case with a mode spacing of 4.13MHz, which

corresponds to a ring cavity length of 55.5m. The case with random grating feedback presents a pure single-mode lasing peak with a contrast over 50dB as shown in Figure 7-2(b). During the ultrasound detection, the lasing output from the 5% port of the 95/5 coupler was directly detected by a 350MHz photo-detector and the oscillation signals were observed and recorded by an oscilloscope with a sampling rate of 5MS/s.

The sensing principle of the proposed random fiber laser for ultrasound detection is based on the loss modulation of the laser ring cavity, where the sensitivity depends on the spectral slope of the wavelength position selected by the TF in the reflection spectrum of the fiber random grating. Generally, the strain-optic and geometric effects induced by the ultrasonic wave would cause the refractive index profile changes along the random grating, leading to the spectrum shift. Consequently, the output power of the proposed random laser changes with the shift of the reflection spectrum of the random grating, as the insertion loss from the random grating is varied. Thanks to the steep spectral slope regions in the reflection spectrum of the random grating, the achievable sensing sensitivity of the random laser will be much better than that of the fiber ring laser sensors based on the gain profile of the broadband light source with less steep spectral slope areas. Furthermore, it has been demonstrated that the reflection spectrum of the random grating shifts with almost unchanged shape with variations of temperature in tens of degrees or strain in hundreds of micro-strains [136], which ensures linear modulation of the cavity loss and results in periodic temporal responses.

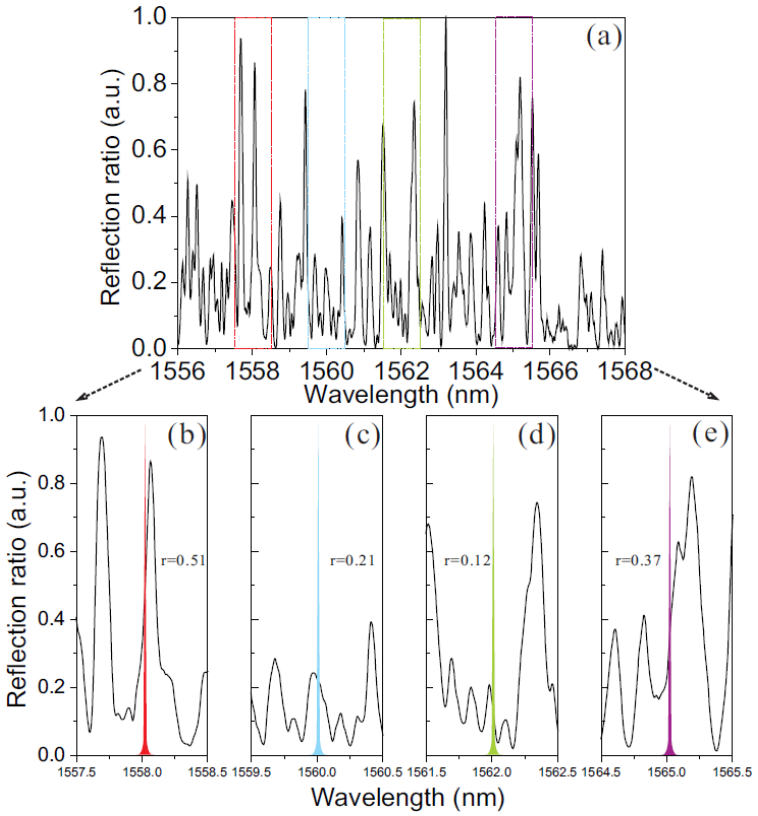

Figure 7-3. (a) Normalized reflection spectrum of fiber random grating in the range between 1556nm and 1568nm; Selected lasing wavelengths at (b) 1558.024nm, (c) 1560.018nm, (d) 1562.014nm, and (e) 1565.026nm.

The detected output AC signal from the photo-detector has a voltage determined by:

$$V_S = R\Delta\lambda_S SGP \tag{7.2}$$

where V_S is the detected AC output voltage, R is the photodetector's response factor, $\Delta\lambda_S$ is the spectral shift caused by the longditudinal strain, S is the spectral slope at the lasing wavelength, G is the gain provided by the EDFA, and P is the laser power. Since the spectral shift of the random grating is proportional to the applied strain, which could be expressed as $\Delta\lambda_S=\alpha\varepsilon$, where α is a constant parameter at a specific lasing wavelength related to refractive index, optoelastic coefficients, and Poisson's ratio, the minimum detectable strain is obtained when the voltages generated by the ultrasonic signal and noise are equal: $V_S=V_N$, where the

noise output V_N includes the intensity and frequency noise of the random laser as well as the noise from the photo-detector itself and could be determined by measuring the proposed random laser output without ultrasound wave impact on the random grating. Thus the minimum detectable strain is obtained as:

$$\varepsilon_{\min} = \frac{V_N}{\alpha RSGP} \tag{7.3}$$

As could be seen from Eq. (7.3), the minimum detectable strain varies with the spectral slope of the lasing wavelength provided that other parameters of the laser system remain constant. Figure 7-3 shows four different wavelengths at 1558.024nm, 1560.018nm, 1562.014nm and 1565.026nm that are selected by the TF for the random lasing in the experiments. The normalized reflection ratios for each selected lasing wavelength are r=0.51, 0.21, 0.12, and 0.37. The local spectral slopes at these wavelengths are S=5.78nm^{-1}, 0.76nm^{-1}, 2.66nm^{-1}, and 4.89nm^{-1}, corresponding to the estimated minimum detectable strains of 0.72nε, 5.48 nε, 1.57 nε, and 0.85 nε by using Eq. (7.3) with parameter values of α=1.2pm/με, R=1V/mW, G=40dB, P=1mW, and V_N=0.05V.

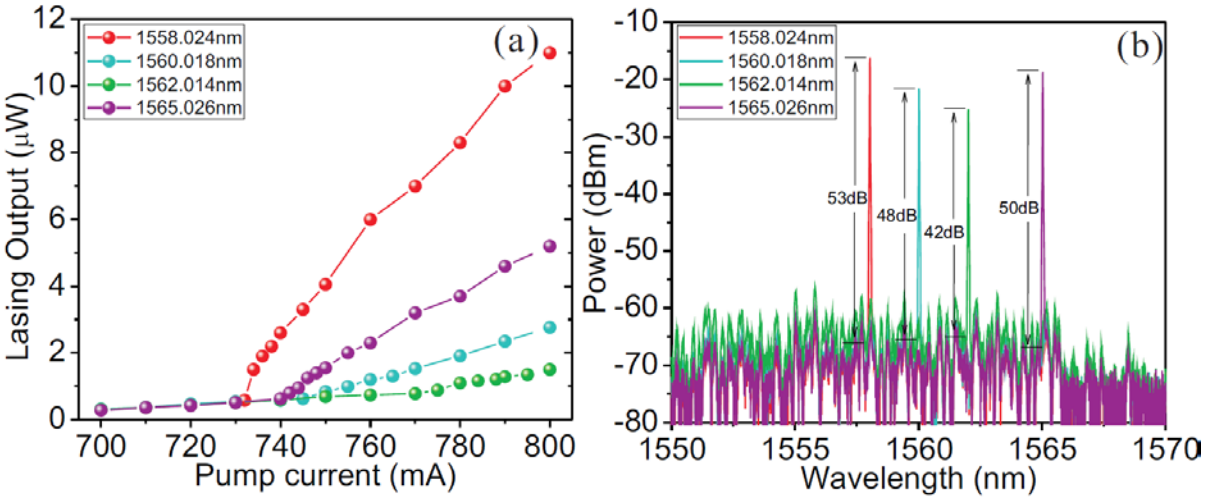

Figure 7-4. (a) Lasing thresholds of the proposed random fiber laser at the four selected lasing wavelengths; (b) Lasing spectra at the selected lasing wavelengths.

The lasing performances of the proposed random fiber laser at the four selected lasing wavelengths are presented in Figure 7-4. Figure 7-4(a) shows the lasing thresholds at the four lasing wavelengths. It is noted that the lasing threshold decreases and the lasing efficiency increases with the increase of the reflection ratio at the selected wavelength. The lasing spectra at the four lasing wavelengths are shown in Figure 7-4(b) with an EDFA pump current of 1A. The contrast of the lasing spike at the four wavelengths also increases with the reflection ratio, all of which show a value over 40dB. It is worth mentioning that by adjusting the SOP of the intra-cavity light through the two PCs, single-mode lasing could be realized for all the four wavelengths, which enables linear response in the ultrasound detection.

7.3 Experimental results

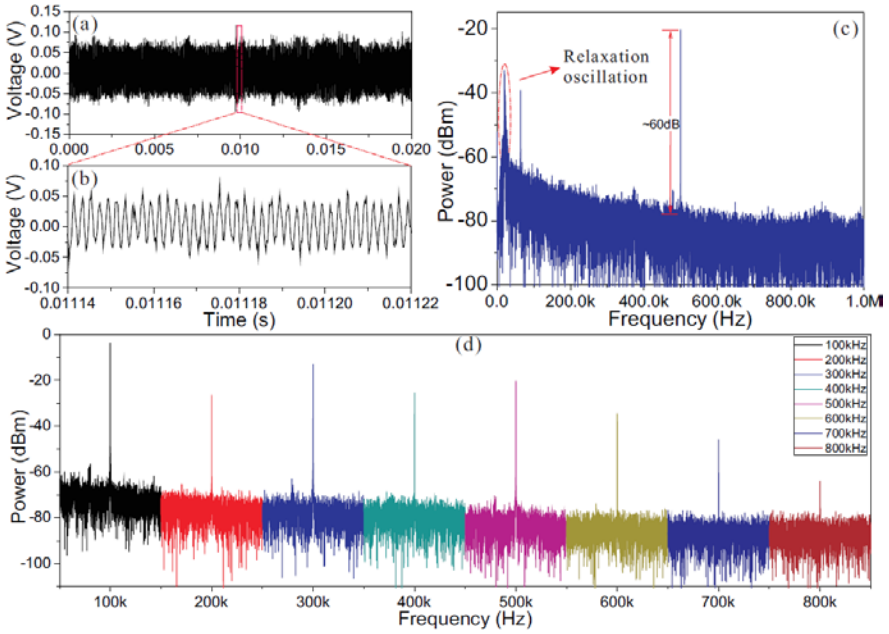

Figure 7-5. Temporal (a) and enlarged temporal (b) responses of the proposed random fiber laser ultrasound sensor; Spectral responses of the sensor for 0.5MHz ultrasonic wave (c) and ultrasound with different frequencies (d).

The experiments of the ultrasound detection were performed when the random fiber laser was operating at each selected lasing wavelength. The EDFA was driven by the same electric current of 1A for all selected lasing wavelengths. Sinusoidal waves with ultrasonic frequencies were generated by the function generator, which drives the PZT actuator glued onto the aluminum plate to resonate at the given frequencies. An example of the temporal response of the random fiber laser is shown in Figure 7-5(a)&(b), where the enlarged time series of the lasing output presents decent periodic sinusoidal signal with a frequency of 0.5MHz at the lasing wavelength of 1565.026nm. However, some low-frequency modulations could be observed in the temporal responses, which are attributed by the intrinsic relaxation oscillation with broadband frequency components around 20kHz in the random fiber laser. The SNR of the detected ultrasound signal is estimated by calculating the ratio of the power of the signal frequency and averaged power of the neighboring frequency components after performing the Fast Fourier Transform (FFT) on the time-series signals over 100k points with a sampling rate of 5MS/s as shown in Figure 7-5(c). The SNR of the detected 0.5MHz ultrasound signal is estimated as high as 60dB. In Figure 7-5(d), ultrasound detection results for different frequencies ranging from 0.1MHz to 0.8MHz are shown with high SNR.

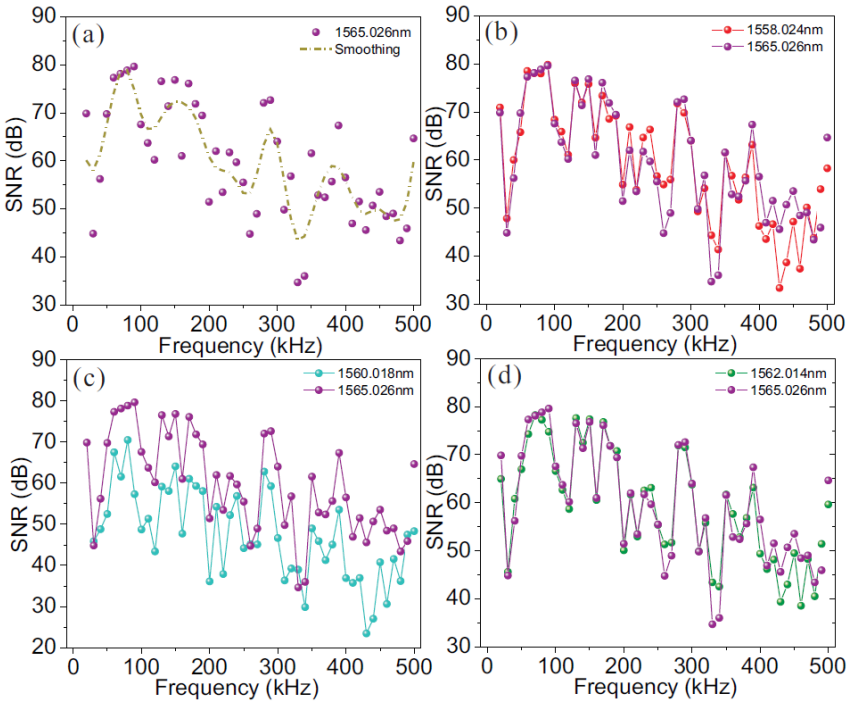

Figure 7-6. (a) SNR as a function of the ultrasound frequency at lasing wavelength of 1565.026nm and the corresponding smoothing curve; (b)-(d) Comparisons of the SNR curves among different lasing wavelengths.

The frequency response of the random laser sensor at lasing wavelength of 1565.026nm is illustrated in Figure 7-6(a), which shows high SNRs for frequencies ranging from 20kHz to 0.8MHz. Ultrasonic waves with higher frequencies can be detected as long as the effective grating length is reduced to less than the wavelength of the ultrasound waves [173, 174]. In order to clearly observe the trend of the results, a smoothing method with an averaging window of 7 is used to smooth the data as shown in the dashed line. The smoothed curve descends with the frequency due to the amplitude decay of the acoustic wave in the aluminum plate and at the same time undergoes a non-periodic evolution, which generally follows the relationship between the detection sensitivity and the wavelength of the ultrasound wave but the periodicity is disrupted by the non-uniformity of the random grating induced by the random index modification. The large variations and non-monotonic trend in

the SNR curve may bring potential issues such as distortion in detecting broadband acoustic emission signals, which could be mitigated by either optimizing the random grating periods and its effective length, or applying appropriate calibration methods and signal processing algorithms. Figure 7-6(b)-(d) shows the comparison of the SNR curves among different lasing wavelengths. All the lasing wavelengths have shown excellent SNRs for the ultrasound sensing with frequencies from 20kHz to 0.8MHz, which demonstrates that the proposed random fiber laser ultrasonic sensor is applicable with high sensitivity in harsh environments where the reflection spectrum of the fiber random grating would be significantly shifted. However, it should be noticed that not all the lasing wavelengths are ensured with high sensitivity, especially the wavelength at which the spectral slope is zero. This would not take advantage of the sharp peaks in the reflection spectrum of the random grating but almost only depends on the shape of the ASE profile.

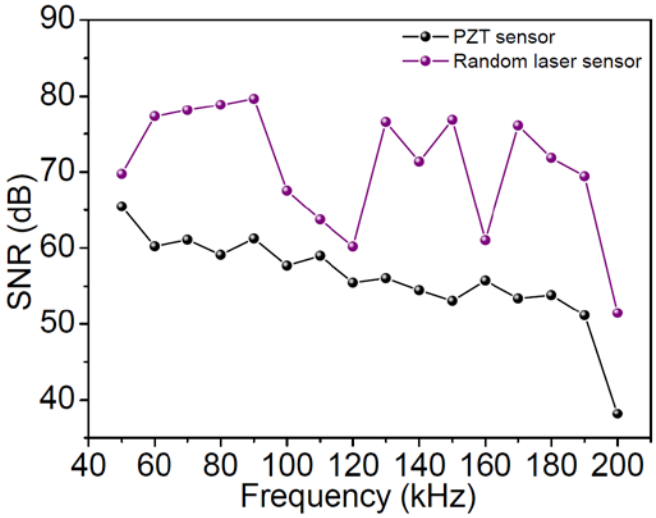

Figure 7-7. Comparison of the SNR curves between the proposed random laser sensor and PZT sensor.

Figure 7-7 shows a comparison of the frequency responses of the proposed random laser sensor operating at 1565.026nm and the conventional PZT acoustic sensor with maximum

detectable frequency up to 200kHz, where the laser sensor has much better performances. The sensitivity of the proposed laser sensor could be estimated by:

$$Sensitivity = \frac{V_S - V_N}{\varepsilon V_{DC}} \tag{7.4}$$

where V_{DC} is the DC output voltage. The sensitivities of the proposed random laser sensor and the PZT sensor are compared at 90kHz where the laser sensor has the maximum response as shown in Table 7-1. The strain induced by the PZT actuator at 90kHz is estimated to be around 50nε by using Eq. (7.2) and the proposed random laser sensor has a better sensitivity than that of the PZT sensor. It should be noted that the laser sensor's V_N includes the noise of the relaxation oscillation of the random laser, which limits the sensitivity of the proposed laser sensor. While in the estimation of the SNR of the laser sensor's frequency response, the relaxation oscillation noise is not counted, leading to better SNR performance.

Table 7-1. Sensitivities of the random laser sensor and PZT sensor

@ 90kHz	V_S (V)	V_N (V)	V_{DC} (V)	Sensitivity ($n\varepsilon^{-1}$)
Laser sensor	3.35	0.05	0.01	6.60
PZT sensor	0.08	0.002	0.001	1.56

7.4 Conclusion

In summary, a highly sensitive random fiber laser based ultrasound sensor is proposed and demonstrated. The fiber random grating, being the random distributed feedback provider and sensing element, shows remarkable properties for the random lasing such as the support of single-mode lasing and excellent sensing performance with high sensitivity over a broad operating wavelength range. The proposed sensor is able to achieve broadband ultrasound detection within 0.8MHz with high SNR and is an ideal sensor in harsh environment with

large temperature or strain variations. It is believed that the proposed laser sensor is a truly practical ultrasonic sensor and would find important applications in many ultrasound-related areas such as structural health monitoring, geophysical exploration, material testing, and biomedicine.

Chapter 8 Time-delay signature suppression in a chaotic semiconductor laser by fiber random grating induced distributed feedback

This chapter presents a novel technique to conceal the time delay signature (TDS) of the chaotic semiconductor laser output by utilizing random distributed feedback from a fiber random grating. A theoretical model is developed based on the Lang-Kobayashi model in order to numerically explore the chaotic dynamics of the laser diode subjected to the random distributed feedback. It is predicted that the random distributed feedback is superior to the single reflection feedback in suppressing the TDS. In experiments, a massive number of feedbacks with randomly varied time delays induced by a fiber random grating introduce large numbers of external cavity modes into the semiconductor laser, leading to the high dimension of chaotic dynamics and thus the concealment of the TDS. The obtained TDS with the maximum suppression is 0.0088, which is the smallest to date. Section 8.1 gives the background of TDS suppression of chaotic semiconductor lasers. Section 8.2 introduces the experimental configuration of the chaotic semiconductor laser with fiber random grating feedback. Section 8.3 shows the theoretical model and simulated results. Section 8.4 presents the experimental results of TDS suppression by fiber random grating feedback. Section 8.5 draws the final conclusion.

8.1 Introduction

Chaos theory reveals that a nonlinear high dimension system may bifurcate to more complex dynamics including chaos [175]. This erratic behavior has been investigated intensively in more practical lasers and has remained a fertile research field for the past decades [28, 29]. Chaotic signals generated from semiconductor lasers are of great interests for a number of promising applications, including high-speed random bit generation, secure communication, data encryption, and chaotic ranging [35, 38, 176-185]. Particularly, laser diode based chaotic output has acted as a physical entropy source for true random number generation, benefiting from outcome unpredictability with no dependence on any previous outcome. The most effective and simplest method to perturb the single mode semiconductor laser into chaos is by returning a small fraction of the laser emission into the laser diode cavity using an external reflector [31, 186, 187]. Coherence collapse dynamics is expected when the frequency of the external cavity is much smaller than the laser's intrinsic relaxation oscillation frequency, leading to high-dimensional chaotic behavior [33]. However, such time-delay systems often suffer from feedback time delay signature (TDS), which could be easily identified by the autocorrelation function (ACF). TDS is potentially detrimental in chaos-based cryptosystems and truly random number generation [188]. Hence its suppression is important and highly desired for these applications. To this end, various feedback configurations, including simple single mirror feedback [189], dual-path feedback from double mirrors [190], and fiber Bragg grating feedback [191, 192], have been investigated and studied. More complex configurations including mutually coupled feedback using two lasers [193, 194], feedback with cascaded coupled laser injection [195], and on-chip integrated optical feedback [196] have also been proposed to suppress the TDS. However,

these techniques increase the hardware complexity of the experimental setup and are not fully applicable in a practical sense.

In this chapter, a simple approach for TDS suppression is developed by employing the feedback from a fiber random grating fabricated by the femtosecond (fs) laser with a large number (>104) of reflectors with random time delays. Randomly placed reflectors along the fiber provide effective random distributed feedback to a laser diode, which is capable of obscuring the TDS of the chaotic output. A theoretical model is established to illustrate the chaotic dynamics of the laser diode subjected to the random distributed feedback and the simulated results predict the larger suppression ratio than that of the single mirror feedback configuration. The experimental results obtained from the random grating feedback show the TDS could be suppressed to a value of 0.0088, which is the smallest value reported to date.

8.2 Experimental configuration

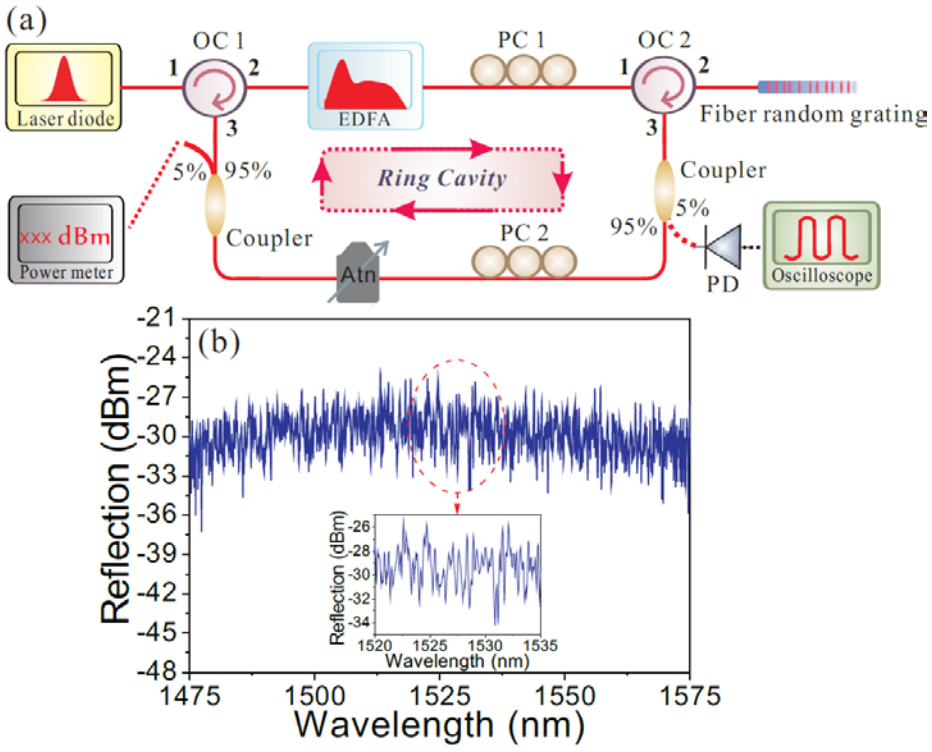

Figure 8-1. (a) Configuration of the laser diode subjected to fiber random grating feedback. OC: Optical Circulator; EDFA: Erbium Doped Fiber Amplifier; PC: Polarization Controller; Atn: Optical Attenuator; PD: Photo-detector; (b) Reflection spectrum of fiber random grating. Inset: enlarged reflection spectrum.

The configuration of the laser diode with random grating feedback is shown in Figure 8-1(a). Light from a single mode laser diode was first amplified with an Erbium-doped fiber amplifier (EDFA) by passing it through an optical circulator (OC1). A polarization controller (PC1) was used to adjust the state of polarization (SOP) of the amplified light before it is reflected by the random grating. The fiber random grating was manufactured using a fs pulse duration regeneratively amplified Ti:sapphire laser operating at 800nm and having an 80 fs pulse duration. Index modification spots with random spacing from 0 to 3.5μm were written along the fiber axis using a precision air bearing stage to translate the fiber and 50× microscope objective to focus the beam [136]. Around 50000 spots were made along the 10cm long standard single mode fiber (SMF). Figure 8-1(b) shows an example of the reflection spectrum of the random grating. A strong interference pattern generated by the backscattered light from different scattering centers is observed (see inset Figure 8-1(b)) and could be regarded as the result of the superposition of numerous Fabry-Perot interferometers and Mach-Zehnder interferometers formed by the index modification spots. The random distributed feedback from the random grating is then passed through a 95/5 coupler. The 5% of the tapped light was detected by a photo-detector (Newport) with a bandwidth of 25GHz and its time domain series was recorded by an oscilloscope. The 95% of the tapped light was sent as the feedback to the laser diode. PC2 was to ensure that the polarizations reflected back from the random grating were equal with that entering into. An optical attenuator was used to adjust the strength of the feedback to the laser diode and a power meter was used to

measure the feedback strength.

8.3 Theoretical model and simulated results

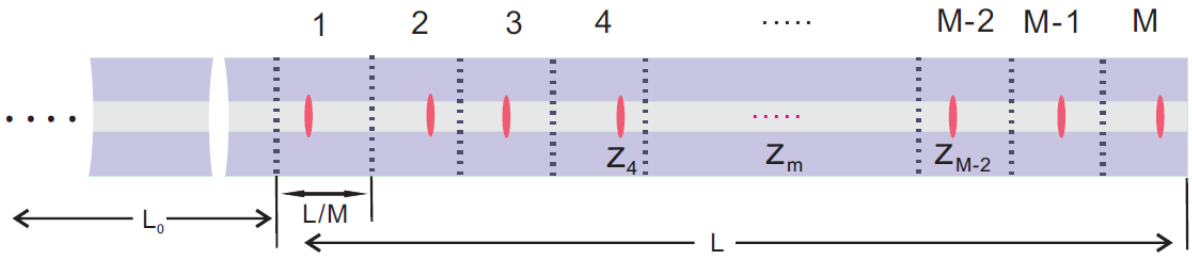

Figure 8-2. Simplified model of the randomly distributed scattering centers in fiber random grating.

In order to investigate the influence of random distributed optical feedback on the dynamics of the chaotic semiconductor laser, the fiber random grating could be theoretically modeled as a collection of large number of enhanced Rayleigh scattering centers randomly distributed along the SMF with L=10cm. Each scattering center introduces optical feedback with a specific delay to the laser diode. As shown in Figure 8-2, a simplified model is developed for the random grating sample. The random grating can be divided into M sections with equal length L/M. Each section has one scattering center, which is randomly located within the section with uniform distribution and assumed to have equal reflection coefficients. The position of each scattering center is denoted as Z_m. The optical path length of the fiber ring structure is 53.5m and the leading fiber length of the random grating sample is L_0=4.01m, corresponding to a total time delay of 307.6ns.

If the light from the laser diode is denoted as $E(t)=A(t)e^{i\varphi(t)}$, under the random distributed optical feedback and neglecting multiple reflections among the scattering centers, the laser field can be numerically simulated by modifying the Lang-Kobayashi model [188, 197-200] as follows:

$$\frac{dA}{dt}=\frac{1}{2}\left[\frac{g(N-N_0)}{1+\varepsilon\left|E\right|^2}-\frac{1}{\tau_p}\right]A+\frac{1}{\tau_{in}}\sum_{m=1}^{M}k_m A(t-\tau_m)\cos[\omega\tau_m+\varphi(t)-\varphi(t-\tau_m)]+F_A(t)$$
$$\frac{d\varphi}{dt}=\frac{1}{2}\alpha\left[\frac{g(N-N_0)}{1+\varepsilon A^2}-\frac{1}{\tau_p}\right]+\frac{1}{\tau_{in}A}\sum_{m=1}^{M}k_m A(t-\tau_m)\sin[\omega\tau_m+\varphi(t)-\varphi(t-\tau_m)]+F_\varphi(t) \quad (8.1)$$
$$\frac{dN}{dt}=pJ_{th}-\frac{N}{\tau_N}-\frac{g(N-N_0)}{1+\varepsilon A^2}A^2$$

with

$$F_A(t)=2\beta N/A+\sqrt{2\beta N}\zeta_A(t)$$
$$F_\varphi(t)=(1/A)\sqrt{2\beta N}\zeta_\varphi(t) \quad (8.2)$$

where k_m and τ_m are the feedback reflectivity and feedback delay for each scattering center in the fiber random grating, respectively. k_m is equal for all of the M scattering centers and τ_m follows uniform distribution within each divided section. Considering the computing efficiency and the limited computing power of the computers in the lab, simulations with M=100 and 200 were performed, respectively. Although the M value used in simulation is smaller than the number of reflectors in the fiber random grating, it is still able to predict the TDS suppression as shown later in this letter. The parameters of the laser used in simulations are listed as follows: N_0=4.55×10^{23} m^{-3} is the transparency carrier density, g=3×10^{-12} m^{3}s^{-1} is the differential gain, ε=5×10^{-23} m^3 is the gain saturation parameter, τ_p=1.17ps is the photon lifetime, τ_N=2.5ns is the carrier lifetime, α=5.0 is the linewidth enhancement factor, τ_{in}=7.38ps is the round-trip time in the laser diode cavity, J_{th}=6.568×10^{32} m^{-3}s^{-1} is the threshold current density, p=2.0 is the pumping factor, $\omega=2\pi c/\lambda$ is the angular frequency of the laser field, where λ=1550nm and c=3×10^8 m/s, $F_A(t)$ and $F\varphi(t)$ are polar decomposition in amplitude and phase of the spontaneous emission noise, including the fluctuations arising from the spontaneous process and denoted in the form of the Langevin noise source, β is the spontaneous emission rate, $\zeta_A(t)$ and $\zeta_\varphi(t)$ represent uncorrelated white Gaussian noises with

zero mean and correlations following $<\zeta_A(t)>=<\zeta_\varphi(t)>=0$ and $<\zeta_A(t)\zeta_A(t')>=<\zeta_\varphi(t)\zeta_\varphi(t')>=\delta(t-t')$ and $<\zeta_A(t)\zeta_\varphi(t')>=0$, the spontaneous emission noise is about eight orders of magnitude smaller than the laser field in amplitude.

Numerical simulations were performed using Eq. (8.1) and (8.2) with random distributed feedback and single reflection feedback, respectively. In simulations, the current density J was set as $2J_{th}$, at which the intrinsic relaxation oscillation frequency of the laser diode was around 7GHz. The ACF of the chaotic laser output is computed to obtain the TDS using the following equation:

$$C(\tau)=\frac{\left\langle (I(t)-\left\langle I(t)\right\rangle)(I(t+\tau)-\left\langle I(t)\right\rangle)\right\rangle}{(\left\langle (I(t)-\left\langle I(t)\right\rangle)^2\right\rangle\left\langle (I(t+\tau)-\left\langle I(t)\right\rangle)^2\right\rangle)^{1/2}} \tag{8.3}$$

where $I(t)$ is the chaotic time domain series, τ is the time delay.

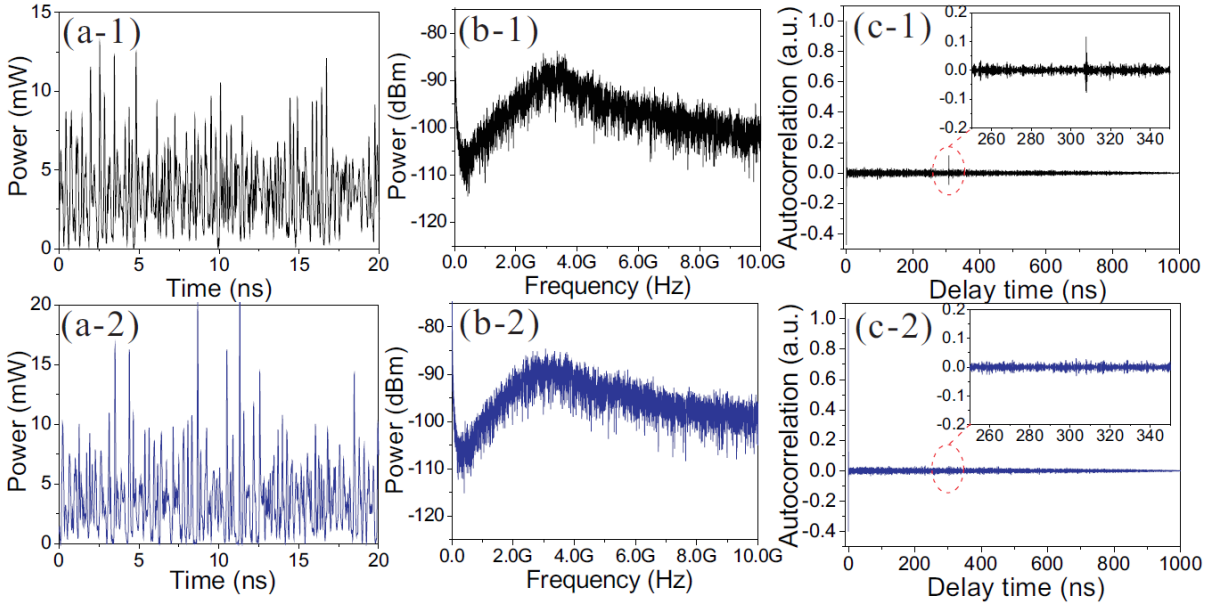

Figure 8-3. Simulation results of (a) time domain series, (b) power spectra, and (c) ACFs for laser diode subjected to single reflection feedback (1) and random distributed feedback (2), respectively.

Figure 8-3(a)-(c) plot the time domain series of the chaotic laser output, power spectra, and ACFs of the output signals for single reflection feedback and random distributed

feedback, respectively. The total feedback reflectivity from the distributed feedback in the simulation is the same as the single reflection feedback, which is 0.09 in amplitude. With this level of feedback strength, the laser diode is perturbed into a state of chaotic emission as shown in column 1 of Figure 8-3. Although the power spectra for both cases look similar, the ACFs of the time domain series show obvious TDS for the single reflection feedback while the TDS is significantly suppressed and hardly noticeable for the random distributed feedback. This indicates that random distributed feedback is able to obscure the periodicity in the time domain series by introducing many sets of the external cavity modes to the laser diode, leading to chaotic emission free from the TDS.

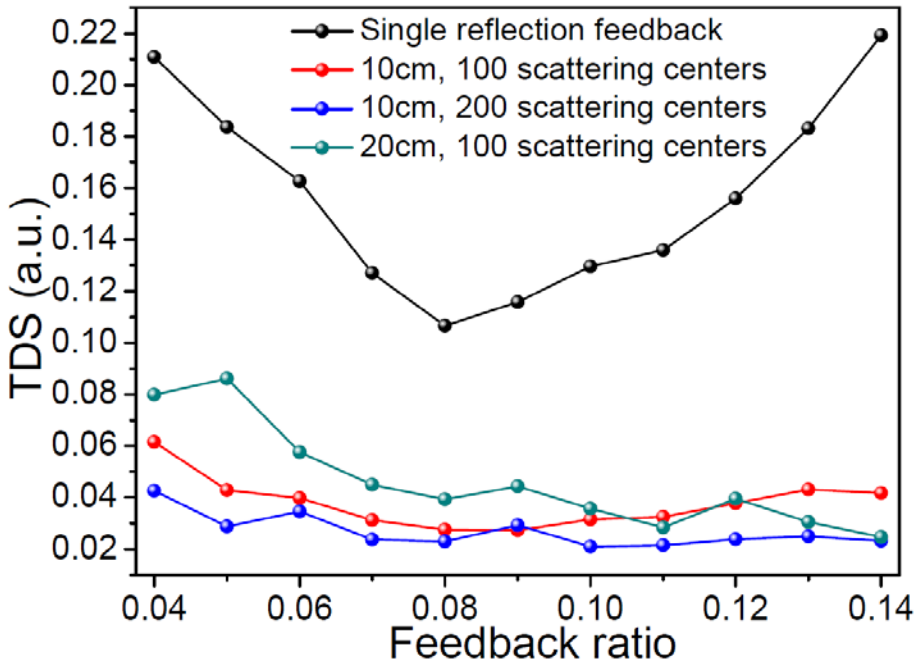

Figure 8-4. Computed TDS values of the chaotic laser subjected to single reflection feedback (black) and random distributed feedbacks from 10cm long random grating with 100 scattering centers (red), 10cm long random grating with 200 scattering centers (blue), 20cm long random grating with 100 scattering centers (dark cyan) as a function of feedback ratio.

The influence of reflection ratios on the TDS for both cases was also investigated as

shown in Figure 8-4. In the simulations, different distributed feedbacks were modeled in order to investigate the dependence of TDS suppression on the random grating parameters. The results show that whenever the grating length or the number of the scattering centers is changed, the significant suppression of the TDS could still be achieved with proper feedback ratio and a larger number of scattering centers is able to suppress the TDS more significantly. It is also found that over a relatively large range of reflection strengths, the random distributed feedback has much lower TDS values, with suppression ratios greater than 10 times that of the single reflection feedback. Furthermore, the TDS value of the random distributed feedback is less dependent on the feedback strength than that of the single reflection case.

8.4 Experimental results

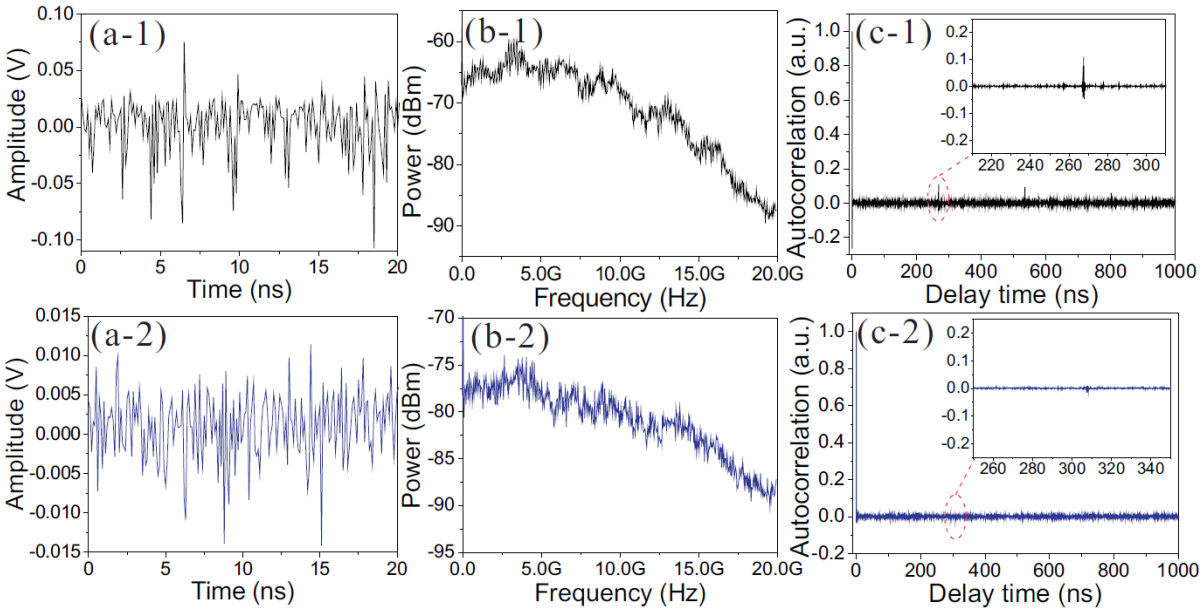

Figure 8-5. Experimental results of (a) time domain series, (b) power spectra, and (c) ACFs for laser diode subjected to single mirror feedback (1) and random grating feedback (2), respectively.

In experiments, a fiber random grating sample or a single mirror was connected with port

2 of OC 2 in Figure 8-1(a), respectively. The laser diode was operating with a driven current 2 times the threshold value, which emitted light with an output power around 1.0mW and an intrinsic relaxation oscillation frequency of 7GHz. The feedback from the random grating and the mirror was adjusted to 0.22 (in amplitude) and the experimental results are shown in Figure 8-5. The measured time domain series, power spectra and ACFs of the chaotic output signal are obtained for both random grating feedback and mirror feedback. It is noted that the power spectra for both cases extend to lower frequency range, which could be explained by the anti-guidance effects in semiconductor lasers induced by the external feedback. The red-shift is even more obvious in the experimental results than within the simulation results due to the stronger feedback injected into the laser diode during the experiments. As expected, the ACF result for random grating feedback shows a significant suppression in the TDS and the minimum TDS value is obtained when the feedback strength is 0.22, which is only 0.0088 and almost negligible when compared with that of the mirror feedback result.

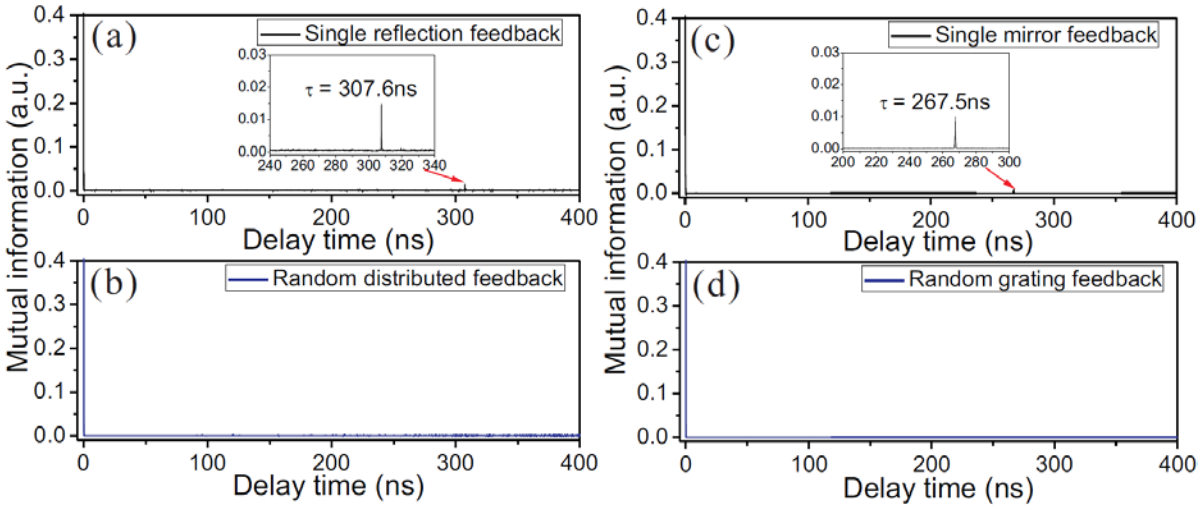

Figure 8-6. Mutual information of simulated results for chaotic laser subjected to (a) single reflection feedback and (b) random distributed feedback with a feedback ratio of 0.09; Mutual information of experimental results for chaotic laser subjected to (c) single mirror feedback and (d) fiber random grating feedback with a feedback ratio of 0.22.

Mutual information (MI) was also computed for the simulated and experimental chaotic time domain series to justify the suppression of TDS as shown in Figure 8-6 using the following equation:

$$M(\tau) = \sum_{I(t),I(t+\tau)} p(I(t), I(t+\tau)) \log \frac{p(I(t), I(t+\tau))}{p(I(t))\, p(I(t+\tau))} \tag{8.4}$$

where $p(I(t), I(t+\tau))$ is the joint probability density, $p(I(t))$ and $p(I(t+\tau))$ are the marginal probability densities. It is clearly shown that the random distributed feedback from the fiber random grating is able to effectively cancel the TDS in the chaotic time domain series for both simulated and experimental results, which is mainly attributed to two effects: i) as the TDS in the single reflection scheme originates from the beating between the longitudinal modes in the single external cavity, the large number of scattering centers in the fiber random grating introduces large numbers of external cavity modes competing for the limited optical gain. Chaotic instability with high dimension is then expected and a strong and stable beating between any two of these longitudinal modes is prevented; ii) the random distributed feedback from the random grating as indicated in the noise-like interfering reflection spectrum due to the individual point writing technique with less phase control induces the frequency-dependent group delay, which corresponds to the group velocity dispersion, on different frequency components of the optical feedback to the laser diode, leading to the obscuring of the information of round trip time delay.

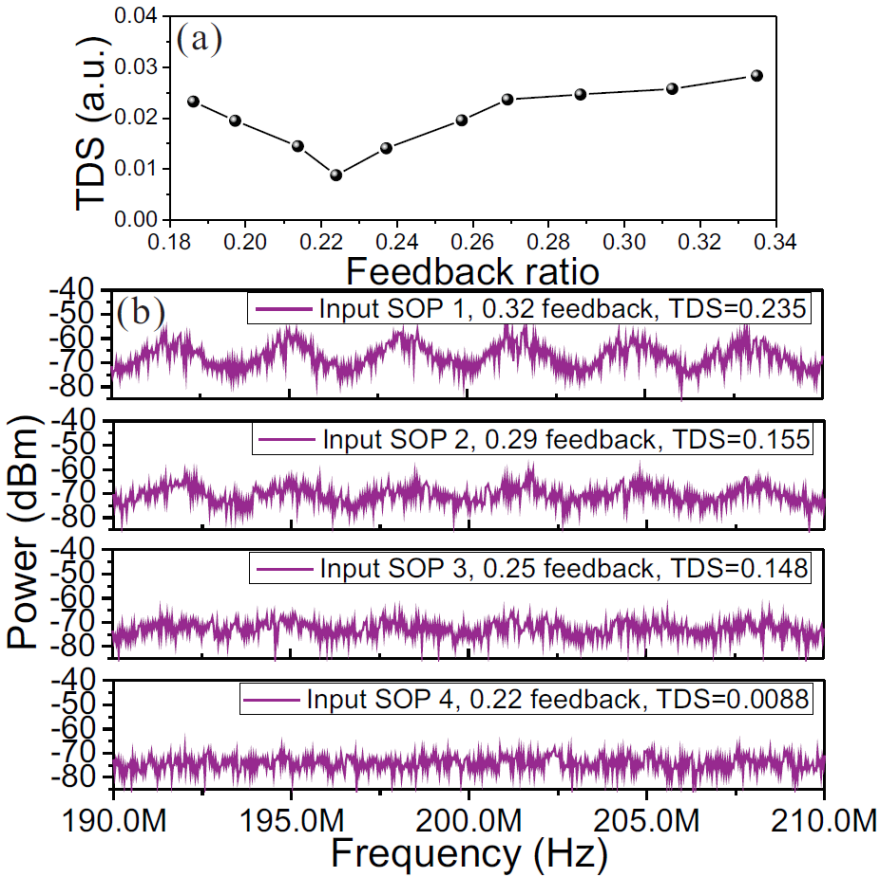

Figure 8-7. (a) TDS value of the chaotic laser subjected to the random grating feedback with the optimized input SOP to the fiber random grating sample; (b) Power spectra of the chaotic laser output with different input SOPs to the fiber random grating sample and the corresponding TDS values.

Due to the randomly distributed index modification spots along the fiber random grating, the directions for the principal birefringence axes of each scattering center are different from each other. Thus it is impossible to realize the alignment of the SOP of the light launched into the random grating with the directions of the local principal birefringence axes at each scattering center, resulting in different reflection coefficients at each reflector. The suppression performance of the random distributed feedback therefore depends on the SOP of the light that was launched into the random grating sample, which could be studied by adjusting PC 1 and keeping PC 2 fixed. It is found that the SOP of the light launched into the

random grating significantly influences the TDS of the chaotic output. By adjusting the SOP of the input light to an optimized state where a large number of scattering centers have almost comparable contributions to the reflection, the dependence on the feedback strength of the TDS for the random grating feedback is obtained as shown in Figure 8-7(a). The feedback strength was varied through the optical attenuator in Figure 8-1(a) and both PCs were kept unchanged. The measured curve has a similar trend with the simulated result shown in Figure 8-4 and shows low TDS values over the measured feedback strength range as expected. However, when the SOP of the light launched into the random grating was changed, the feedback strength as well as the TDS experiences large variations as shown in Figure 8-7(b). This phenomenon is mainly attributed to the polarization dependent scattering from the scattering centers that are fabricated through the fs laser modification in the random grating. The resultant random birefringence makes the scattering centers highly polarization dependent and scatter the input light at different reflection levels according to the polarization matching conditions. Consequently, two distinct situations are expected: i) it is possible that there is one or two scattering centers that scatter back dominant light power over the others when perfectly polarization-matched with that of the input light, which renders similar results with the single reflection feedback and large TDS values; ii) On the other hand, it is also possible to find an SOP of the input light which leads to a light backscattering almost equally shared among a number of scattering centers rather than a reflection by one or two dominant scattering centers, which effectively takes advantages of the random distributed feedback from the random grating and obscures the periodicity of the time series. The first three power spectra in Figure 8-7(b) belonging to the first situation clearly show a periodicity with a frequency spacing of 3.25MHz, which corresponds to the total ring length of 61.52m. While the periodicity in the last power spectrum which belongs

to the second situation is hardly observed. Naturally, the TDS values in the first situation are much larger than that in the second situation.

8.5 Conclusion

In conclusion, the suppression of TDS has been theoretically and experimentally realized in a semiconductor laser subjected to the distributed feedback from a fiber random grating. A theoretical model is established for numerical simulations, which predicts the robustness of the random distributed feedback in eliminating the periodicity in laser diode-based optical chaos. The experimental results show a tremendous suppression in TDS with a minimum value of 0.0088 to date, allowing the effective and simple approach applicable in the concealment of the encryption system parameters and hence improving the security in optical chaos based communications.

Chapter 9 Summary and future work

9.1 Summary

This thesis mainly focuses on developing a novel fiber random grating using fs laser micromachining technique and its applications in random fiber lasers and chaotic semiconductor lasers. The background of fs laser micromachining technique and the development of fiber random gratings are also reviewed and discussed. The fabrication process of the novel fiber random grating is described and its optical properties are analyzed theoretically and demonstrated experimentally. The randomly varying spaced plane-by-plane writing technique brings novel physical properties to the fiber random grating, such as multiple interfering reflection spectrum and induced random birefringence along the sample fiber. Based on its optical properties, a multi-parameter fiber-optic sensor is realized to simultaneously measure the temperature, axial strain, and surrounding refractive index by employing a wavelength-division spectral cross-correlation algorithm. Maximum sensitivities of 10.32 pm/°C, 1.24 pm/με, and −1520.6 pm/RIU were achieved with small errors for temperature, axial strain, and surrounding refractive index, respectively. The developed sensor can be potentially applicable in areas of engineering, biomedical, biological, and environmental sensing with its robust physical strength and high sensitivities.

We have also developed two novel BRFLs with bi-pumping scheme based on the intrinsic Rayleigh scattering feedback and fiber random grating feedback. In the first work, a novel BRFL with a narrow linewidth of ~860 Hz was proposed and demonstrated based on the bi-directionally pumped SBS in a 10-km-long optical fiber. The physical mechanism of such a random fiber laser is clarified through a random fiber FP resonator, which is built up

through the pump depletion effects of SBS at both ends of the fiber and enables narrow random lasing emission. The novel laser is successfully applied for linewidth characterization beyond 860 Hz of light source under test. In the second work, fiber random grating based resonator replaces the intrinsic Rayleigh scattering based resonator in the bi-pumped BRFL, which significantly enhances the random feedback and increases the lasing efficiency. The linewidth of the coherent random lasing spike is measured to be ~45.8 Hz using the heterodyne technique. The intensity and frequency noises are further suppressed compared to that of the intrinsic Rayleigh feedback resonator based BRFL.

The fiber random grating is also applied in EDF based random fiber lasers, which realizes both static and dynamic parameter sensing. The fiber random grating provides numerous polarization-dependent spectral filters, which are superimposed with each other to generate multiple lasing lines with high signal-to-noise ratio up to 40dB. This gives an access for a high-fidelity multiple-static-parameter sensing scheme. By controlling the number of the lasing lines through the SOP of intra-cavity light, different numbers of sensing parameters can be measured through monitoring the wavelength shift of the lasing lines. Temperature and strain are simultaneously measured with maximum errors of 2.3^{o}C and 15.2με. Ultrasound detection is also achieved by the fiber random grating based EDF random laser. Thanks to the random distributed feedback from the fiber random grating, the single-mode operation of the random fiber laser ensures linear and pure temporal responses to the broadband ultrasonic acoustic emission from 20kHz to 0.8MHz. The sensitivity of the ultrasound detection is enhanced by the large number of steep peak areas over a broad spectral range, by which, the sensing system, with high probability, has a lasing mode at a steep region of the reflection spectrum where the sensitivity is the greatest. The proposed sensor is an ideal alternative in harsh environment with large temperature or strain variations.

Compared to the conventional piezoelectric acoustic sensors, the novel sensor enables a signal-to-noise ratio improvement up to 20dB.

Finally, we demonstrate that the time delay signature of a chaotic semiconductor laser output could be cancelled out by employing the fiber random grating feedback. A modified Lang-Kobayashi model is developed to explore the chaotic dynamics of the laser diode subjected to the random distributed feedback. Both the simulations and experiments demonstrate the concealment of the time delay signature in the chaotic output thanks to the large numbers of external cavity modes introduced into the semiconductor laser by the fiber random grating. The induced high dimension of chaotic dynamics suppresses the time delay signature to a value of 0.0088, which is the smallest to date.

9.2 Future work

The proposed fiber random grating is a novel compact random fiber medium with enhanced random distributed feedback, which would pave the way for a lot of important applications and researches. The work summarized in this thesis only introduces part of the applications of the fiber random grating and will spark further interests in other reliable researches and implementations.

Future work on fiber random grating may focus on the optimization of its reflection and transmission strength and further miniaturization. As the fiber random grating used in previous works has relatively large transmission loss, only the reflection spectrum could be employed, which significantly complicates the experimental configuration in the fiber random grating based BRFL with bi-pump scheme. With optimized fabrication technique, fiber random gratings could be directly inscribed at both ends of the SBS gain fiber, which eliminates the needs for optical couplers and increases the ratio of the input power coupled to

the gain fiber. Thus the random distributed feedback from fiber random grating could be fully exploited by the laser system, leading to enhanced lasing efficiency. The size of the fiber random grating may also be miniaturized by writing index modification spots with denser spacing. Currently the maximum spacing between neighboring spots is 3.5μm, which could be further decreased to sub-micron. Consequently, more index modification spots could be made along a shorter length of optical fiber. The decreased length of fiber random grating would be beneficial for the improvement of both laser intensity and frequency noises, as the external disturbances will have less impact on the short random cavities with good packages and soundproof facilities.

Another future work based on the fiber random grating would be developing multi-wavelength random fiber lasers as narrow-linewidth multi-wavelength fiber lasers are of significant interests for fiber-optic sensors, spectroscopy, optical communications, and microwave generation. Although multi-wavelength random fiber lasers with Raman gain and EDF gain have drawn intensive attention and turned to be a promising light source with simple design, they suffer from either broadband linewidth or intense mode competition induced by the homogeneous gain of the EDF. One way to overcome these drawbacks is to utilize semiconductor optical amplifier based random fiber laser with fiber random grating feedback, which on one hand mitigates the mode competition and ensures stable multi-wavelength lasing thanks to the inhomogeneous gain of SOA, and on the other hand is able to achieve narrow linewidth with the cavity mode suppression by the random distributed feedback from the fiber random grating.

Furthermore, fiber random grating based random fiber laser is also able to realize random number generation without time delay signature. With the gain from SOA and random distributed feedback from fiber random grating, a random fiber ring laser could be

built up. By introducing a long fiber delay into the half-open ring cavity, large numbers of cavity modes would induce high-dimension laser dynamics. By adjusting the pumping power of SOA and random feedback strength from fiber random grating, a broadband random fiber laser could be realized for optical random number generation at high speed and without time delay signature.

Curriculum Vitae

Full name Yanping Xu

Education

Ph.D. in Physics (Sep.2013-Aug.2017)
Department of Physics
University of Ottawa, Ottawa, Canada
Supervisors: Prof. Xiaoyi Bao and Prof. Ping Lu

M.Sc. (Sep.2011-Aug.2013)
Department of Physics
University of Ottawa, Ottawa, Canada
Supervisors: Prof. Xiaoyi Bao and Prof. Ping Lu

B.S. (Sep.2007-Jun.2011)
College of Physics
Jilin University, Changchun, P. R. China

Publications

Journal Paper

1. **Yanping Xu**, Liang Zhang, Liang Chen, and Xiaoyi Bao, “Single-mode SOA-based 1kHz-linewidth dual-wavelength random fiber laser,” Opt. Express 25(14), 15828-15837 (2017).
2. **Yanping Xu**, Liang Zhang, Song Gao, Ping Lu, Stephen Mihailov, and Xiaoyi Bao, “Highly sensitive fiber-random-grating based random laser sensor for ultrasound detection,” Opt. Lett. 42(7), 1353-1356 (2017).
3. **Yanping Xu**, Ping Lu, Liang Chen, and Xiaoyi Bao, “Recent developments in micro-structured fiber optic sensors,” Fibers. 5(1), 3 (2017). (***Invited***)
4. **Yanping Xu**, Mingjiang Zhang, Ping Lu, Stephen Mihailov, and Xiaoyi Bao, "Multi-parameter sensor based on random fiber lasers,” AIP Adv. 6, 095009 (2016).
5. **Yanping Xu**, Song Gao, Ping Lu, Stephen Mihailov, Liang Chen and Xiaoyi Bao, “Low noise Brillouin random fiber laser with random grating based resonator,” Opt. Lett. 41(14), 3197-3200 (2016).
6. **Yanping Xu**, Meiqi Ren, Yang Lu, Ping Lu, Ping Lu, Xiaoyi Bao, Lixian Wang, Younes Messaddeq and Sophie LaRochelle, “Multi-parameter sensor based on the SBS in the inverse-parabolic graded-index fiber,” Opt. Lett. 41(6), 1138-1141 (2016).
7. **Yanping Xu**, Ping Lu, Song Gao, Dao Xiang, Ping Lu, Stephen Mihailov and Xiaoyi Bao, “Optical fiber random grating-based multiparameter sensor,” Opt. Lett. 40(23), 5514-5517 (2015).
8. **Yanping Xu**, Ping Lu, Jia Song, Ping Lu, Liang Chen, Xiaoyi Bao, and Xiaopeng Dong, “Dispersion effects of high-order-mode fiber on temperature and axial strain discrimination,” Photonic Sensors. 5(3), 224-234 (2015).
9. **Yanping Xu**, Dao Xiang, Zhonghua Ou, Ping Lu, and Xiaoyi Bao, “Random Fabry–Perot resonator-based sub-kHz Brillouin fiber laser to improve spectral resolution in linewidth measurement,” Opt. Lett. 40(9), 1920-1923 (2015).
10. **Yanping Xu**, Ping Lu, Zengguang Qin, Jeremie Harris, Farhana Baset, Ping Lu, Vedula Ravi Bhardwaj, and Xiaoyi Bao, “Vibration sensing using a tapered bend-insensitive fiber based Mach-Zehnder interferometer,” Opt. Express 21(3), 3031-3042 (2013).

11. **Yanping Xu**, Mingjiang Zhang, Liang Zhang, Ping Lu, Stephen Mihailov, and Xiaoyi Bao, “Suppression of time-delay signature in chaotic semiconductor laser by fiber random grating induced distributed feedback,” *Accepted by Optics Letters*.
12. **Yanping Xu**, and Xiaoyi Bao, “Micro-structured fibers and their applications in fiber-optic sensors and random fiber lasers,” *Accepted by Canadian Journal of Physics*.
13. Liang Zhang, **Yanping Xu**, Song Gao, Bhavaye Saxena, Liang Chen, and Xiaoyi Bao, “Multi-wavelength coherent Brillouin random fiber laser with ultra-high optical signal-to-noise ratio,” IEEE J. Sel. Top. Quantum Electron. 24(3), 1-8 (2018).
14. Liang Zhang, **Yanping Xu**, Song Gao, Bhavaye Saxena, Liang Chen, and Xiaoyi Bao, “Linearly polarized low-noise Brillouin random fiber laser,” Opt. Lett. 42(4), 739-742 (2017).
15. Ping Lu, **Yanping Xu**, Farhana Baset, Xiaoyi Bao, and Ravi Bhardwaj, “In-line fiber microcantilever vibration sensor,” Appl. Phys. Lett. 103, 211113 (2013).
16. Song Gao, Liang Zhang, **Yanping Xu**, Liang Chen, Xiaoyi Bao, “High-speed truly physical random bit generation via Brillouin random fiber laser with non-uniform fibers,” IEEE Photon. Technol. Lett. 29(16), 1352-1355 (2017).
17. Song Gao, Liang Zhang, **Yanping Xu**, Ping Lu, Liang Chen, and Xiaoyi Bao, "Tapered fiber based Brillouin random fiber laser and its application for linewidth measurement," Opt. Express 24 (25), 28353-28360 (2016).
18. Dao Xiang, Ping Lu, **Yanping Xu**, Liang Chen, Xiaoyi Bao, “Random Brillouin fiber laser for tunable ultra-narrow linewidth microwave generation,” Opt. Lett. 41(20), 4839-4842 (2016).
19. Dao Xiang, Ping Lu, **Yanping Xu**, Song Gao, Liang Chen, and Xiaoyi Bao, “Truly random bit generation based on a novel random Brillouin fiber laser,” Opt. Lett. 40(22), 5415–5418 (2015).
20. Ping Lu, Jeremie Harris, **Yanping Xu**, Yang Lu, Liang Chen, and Xiaoyi Bao, “Simultaneous refractive index and temperature measurements using a tapered bend-resistant fiber interferometer,” Opt. Lett. 37(22), 4567–4569 (2012).
21. Liang Zhang, Chen Wang, Zhengying Li, **Yanping Xu**, Bhavaye Saxena, Song Gao, Liang Chen, and Xiaoyi Bao, "High-efficiency Brillouin random fiber laser using all-polarization maintaining ring cavity," Opt. Express 25, 11306-11314 (2017).
22. Jia Song, Wenhai Li, Ping Lu, **Yanping Xu**, Liang Chen, Xiaoyi Bao, “Long-Range High Spatial Resolution Distributed Temperature and Strain

Sensing Based on Optical Frequency-Domain Reflectometry," Photonics Journal. 6(3), 6801408 (2014)

23. Jeremie Harris, Ping Lu, Hugo Larocque, **Yanping Xu**, Liang Chen, and Xiaoyi Bao, "Highly sensitive in-fiber interferometric refractometer with temperature and axial strain compensation," Opt. Express 21(8), 9996-10009 (2013)

Conference Paper

1. **Yanping Xu**, Mingjiang Zhang, Ping Lu, Stephen Mihailov, and Xiaoyi Bao, "Multi-parameter fiber-optic sensors based on fiber random grating," 2017, OFS25th, Jeju, Korea.
2. **Yanping Xu**, Liang Zhang, Mingjiang Zhang, Ping Lu, Stephen Mihailov, and Xiaoyi Bao, "Fiber random grating feedback induced chaos in semiconductor laser with highly suppressed time-delay signature," 2017, Optical Fiber Communication Conference, Los Angeles, California, USA.
3. **Yanping Xu**, Dao Xiang, Zhonghua Ou, Song Gao, and Xiaoyi Bao, "Novel bi-pumped Brillouin random fiber laser and its applications," 2015, Schawlow-Townes Symposium: Poster Session, Ottawa, Canada.
4. **Yanping Xu**, Meiqi Ren, Yang Lu, Ping Lu, Xiaoyi Bao, and Sophie LaRochelle. "Multi-parameter sensing based on the stimulated Brillouin scattering of higher-order acoustic modes in OAM fiber," 2015, OFS24th, Curitiba, Brazil.
5. **Yanping Xu**, Ping Lu, Farhana Baset, Vedula Ravi Bhardwaj, Xiaoyi Bao. "Bend-insensitive fiber based vibration sensor," 2014, OFS23rd, Santander, Spain.
6. **Yanping Xu**, Ping Lu, Jia Song, Liang Chen, and Xiaoyi Bao, Xiaopeng Dong, Ping Lu. "Discrimination of temperature and axial strain using dispersion effects of high-order-mode fibers," Sensors, 2013 IEEE, Baltimore, MD, USA.
7. Liang Zhang, **Yanping Xu**, Song Gao, Bhavaye Saxena, Liang Chen, and Xiaoyi Bao, "Multi-wavelength Coherent Brillouin Random Fiber Laser with High Optical Signal-to-Noise Ratio," 2017, Conference on Lasers and Electro-Optics, San Jose, California, USA.
8. Jérémie Harris, Ping Lu, Hugo Larocque, **Yanping Xu**, Liang Chen and Xiaoyi Bao. "Temperature and strain compensation for refractive index measurement using bend-insensitive optical fiber," Photonic Sensors. 15th Annual Photonics North Conference; 2013 June 3-5; Ottawa, ON, Canada.

Bibliography

[1] Du, D., Liu, X., Korn, G., Squier, J.; Mourou, G. Laser ‐ induced breakdown by impact ionization in SiO2 with pulse widths from 7 ns to 150 fs. *Applied physics letters* **1994**, *64*, 3071-3073.

[2] Pronko, P., Dutta, S., Squier, J., Rudd, J., Du, D.; Mourou, G. Machining of sub-micron holes using a femtosecond laser at 800 nm. *Optics communications* **1995**, *114*, 106-110.

[3] Joglekar, A.P., Liu, H.-h., Spooner, G., Meyhöfer, E., Mourou, G.; Hunt, A. A study of the deterministic character of optical damage by femtosecond laser pulses and applications to nanomachining. *Applied Physics B: Lasers and Optics* **2003**, *77*, 25-30.

[4] Chimmalgi, A., Choi, T., Grigoropoulos, C.; Komvopoulos, K. Femtosecond laser aperturless near-field nanomachining of metals assisted by scanning probe microscopy. *Applied Physics Letters* **2003**, *82*, 1146-1148.

[5] Gattass, R.R.; Mazur, E. Femtosecond laser micromachining in transparent materials. *Nature photonics* **2008**, *2*, 219-225.

[6] Davis, K.M., Miura, K., Sugimoto, N.; Hirao, K. Writing waveguides in glass with a femtosecond laser. *Optics letters* **1996**, *21*, 1729-1731.

[7] Sudrie, L., Franco, M., Prade, B.; Mysyrowicz, A. Study of damage in fused silica induced by ultra-short IR laser pulses. *Optics Communications* **2001**, *191*, 333-339.

[8] Mihailov, S.J., Smelser, C.W., Lu, P., Walker, R.B., Grobnic, D., Ding, H., Henderson, G.; Unruh, J. Fiber Bragg gratings made with a phase mask and 800-nm femtosecond radiation. *Optics letters* **2003**, *28*, 995-997.

[9] Martinez, A., Dubov, M., Khrushchev, I.; Bennion, I. Direct writing of fibre Bragg gratings by femtosecond laser. *Electronics Letters* **2004**, *40*, 1170-1172.

[10] Letokhov, V. Stimulated emission of an ensemble of scattering particles with negative absorption. *JETP Letters* **1967**, *5*, 212-215.

[11] Letokhov, V. Generation of light by a scattering medium with negative resonance absorption. *Soviet Journal of Experimental and Theoretical Physics* **1968**, *26*, 835-840.

[12] Wiersma, D.S., van Albada, M.P.; Lagendijk, A. Random laser? *Nature* **1995**, *373*,

[13] Wu, X., Fang, W., Yamilov, A., Chabanov, A., Asatryan, A., Botten, L.; Cao, H. Random lasing in weakly scattering systems. *Physical Review A* **2006**, *74*, 053812.

[14] Ambartsumyan, R., Basov, N., Kryukov, P.; Letokhov, V. Laser with nonresonant

feedback. *JETP Letters* **1966**, *3*, 167-169.

[15] Ambartsumyan, R., Basov, N., Kryukov, P.; Letokhov, V. A laser with a nonresonant feedback. *IEEE Journal of Quantum Electronics* **1966**, *2*, 442-446.

[16] Markushev, V.M., Zolin, V.; Briskina, C.M. Luminescence and stimulated emission of neodymium in sodium lanthanum molybdate powders. *Quantum Electronics* **1986**, *16*, 281-283.

[17] Lawandy, N.M., Balachandran, R., Gomes, A.; Sauvain, E. Laser action in strongly scattering media. *Nature* **1994**, *368*, 436-438.

[18] Cao, H., Zhao, Y., Ong, H., Ho, S., Dai, J.Y., Wu, J.Y.; Chang, R. Ultraviolet lasing in resonators formed by scattering in semiconductor polycrystalline films. *Applied Physics Letters* **1998**, *73*, 3656-3658.

[19] Cao, H., Zhao, Y., Ho, S., Seelig, E., Wang, Q.; Chang, R. Random laser action in semiconductor powder. *Physical Review Letters* **1999**, *82*, 2278.

[20] Anglos, D., Stassinopoulos, A., Das, R.N., Zacharakis, G., Psyllaki, M., Jakubiak, R., Vaia, R.A., Giannelis, E.P.; Anastasiadis, S.H. Random laser action in organic–inorganic nanocomposites. *JOSA B* **2004**, *21*, 208-213.

[21] Frolov, S., Shkunov, M., Fujii, A., Yoshino, K.; Vardeny, Z.V. Lasing and stimulated emission in/spl pi/-conjugated polymers. *IEEE journal of quantum electronics* **2000**, *36*, 2-11.

[22] Dice, G., Mujumdar, S.; Elezzabi, A. Plasmonically enhanced diffusive and subdiffusive metal nanoparticle-dye random laser. *Applied Physics Letters* **2005**, *86*, 131105.

[23] Li, B., Williams, G., Rand, S., Hinklin, T.; Laine, R. Continuous-wave ultraviolet laser action in strongly scattering Nd-doped alumina. *Optics letters* **2002**, *27*, 394-396.

[24] Feng, Y., Huang, S., Qin, G., Musha, M.; Ueda, K.-i. Random microchip laser. *Optics express* **2005**, *13*, 121-126.

[25] Polson, R.C.; Vardeny, Z.V. Random lasing in human tissues. *Applied physics letters* **2004**, *85*, 1289-1291.

[26] Turitsyn, S.K., Babin, S.A., Churkin, D.V., Vatnik, I.D., Nikulin, M.; Podivilov, E.V. Random distributed feedback fibre lasers. *Physics Reports* **2014**, *542*, 133-193.

[27] Turitsyn, S.K., Babin, S.A., El-Taher, A.E., Harper, P., Churkin, D.V., Kablukov, S.I., Ania-Castañón, J.D., Karalekas, V.; Podivilov, E.V. Random distributed feedback fibre laser. *Nature Photonics* **2010**, *4*, 231-235.

[28] Henry, C. Theory of the linewidth of semiconductor lasers. *IEEE Journal of Quantum Electronics* **1982**, *18*, 259-264.

[29] Ohtsubo, J. *Semiconductor lasers: stability, instability and chaos*, ed.; Springer: 2012.

[30] Schuster, H.G.; Lüdge, K. *Nonlinear laser dynamics: from quantum dots to cryptography*, ed.; John Wiley & Sons: 2012.

[31] Mukai, T.; Otsuka, K. New route to optical chaos: Successive-subharmonic-oscil-lation cascade in a semiconductor laser coupled to an external cavity. *Physical review letters* **1985**, *55*, 1711.

[32] Morikawa, T., Mitsuhashi, Y., Shimada, J.; Kojima, Y. Return-beam-induced oscillations in self-coupled semiconductor lasers. *Electronics Letters* **1976**, *12*, 435-436.

[33] Lenstra, D., Verbeek, B.; Den Boef, A. Coherence collapse in single-mode semiconductor lasers due to optical feedback. *IEEE Journal of Quantum Electronics* **1985**, *21*, 674-679.

[34] Colet, P.; Roy, R. Digital communication with synchronized chaotic lasers. *Optics letters* **1994**, *19*, 2056-2058.

[35] Uchida, A., Amano, K., Inoue, M., Hirano, K., Naito, S., Someya, H., Oowada, I., Kurashige, T., Shiki, M.; Yoshimori, S. Fast physical random bit generation with chaotic semiconductor lasers. *Nature Photonics* **2008**, *2*, 728-732.

[36] Kanter, I., Aviad, Y., Reidler, I., Cohen, E.; Rosenbluh, M. An optical ultrafast random bit generator. *Nature Photonics* **2010**, *4*, 58-61.

[37] Akizawa, Y., Yamazaki, T., Uchida, A., Harayama, T., Sunada, S., Arai, K., Yoshimura, K.; Davis, P. Fast Random Number Generation With Bandwidth-Enhanced Chaotic Semiconductor Lasers at 8×50 Gb/s. *IEEE Photonics Technology Letters* **2012**, *24*, 1042-1044.

[38] Myneni, K., Barr, T.A., Reed, B.R., Pethel, S.D.; Corron, N.J. High-precision ranging using a chaotic laser pulse train. *Applied Physics Letters* **2001**, *78*, 1496-1498.

[39] Lin, F.-Y.; Liu, J.-M. Chaotic radar using nonlinear laser dynamics. *IEEE Journal of Quantum Electronics* **2004**, *40*, 815-820.

[40] Murali, K., Sinha, S.; Ditto, W.L. Implementation of NOR gate by a chaotic Chua's circuit. *International Journal of Bifurcation and Chaos* **2003**, *13*, 2669-2672.

[41] Sinha, S.; Ditto, W.L. Dynamics based computation. *Physical Review Letters* **1998**, *81*, 2156.

[42] Feced, R.; Zervas, M.N. Effects of random phase and amplitude errors in optical fiber Bragg gratings. *Journal of lightwave technology* **2000**, *18*, 90-101.

[43] Skaar, J.; Feced, R. Reconstruction of gratings from noisy reflection data. *JOSA A* **2002**, *19*, 2229-2237.

[44] Rosenthal, A.; Horowitz, M. Reconstruction of a fiber Bragg grating from noisy reflection data. *JOSA A* **2005**, *22*, 84-92.

[45] Derevyanko, S. Design of a flat-top fiber Bragg filter via quasi-random modulation of the refractive index. *Optics letters* **2008**, *33*, 2404-2406.

[46] Yin, H., Gbadebo, A.; Turitsyna, E.G. Top-hat random fiber Bragg grating. *Optics letters* **2015**, *40*, 3592-3594.

[47] Gagné, M.; Kashyap, R. Demonstration of a 3 mW threshold Er-doped random fiber laser based on a unique fiber Bragg grating. *Optics express* **2009**, *17*, 19067-19074.

[48] Gagné, M., Bojor, L., Maciejko, R.; Kashyap, R. Novel custom fiber Bragg grating fabrication technique based on push-pull phase shifting interferometry. *Optics express* **2008**, *16*, 21550-21557.

[49] Gagné, M., Loranger, S., Lapointe, J.; Kashyap, R. Fabrication of high quality, ultra-long fiber Bragg gratings: up to 2 million periods in phase. *Optics express* **2014**, *22*, 387-398.

[50] Gagné, M.; Kashyap, R. Random fiber Bragg grating Raman fiber laser. *Optics letters* **2014**, *39*, 2755-2758.

[51] Kamrujjaman Serker, N., Wu, Z.; Li, S. A nonphysics-based approach for vibration-based structural health monitoring under changing environmental conditions. *Structural Health Monitoring* **2010**, *9*, 145-158.

[52] Topliss, S.M., James, S.W., Davis, F., Higson, S.P.; Tatam, R.P. Optical fibre long period grating based selective vapour sensing of volatile organic compounds. *Sensors and Actuators B: Chemical* **2010**, *143*, 629-634.

[53] Grobnic, D., Mihailov, S.J., Smelser, C.W.; Walker, R.B. Multiparameter sensor based on single high-order fiber Bragg grating made with IR-Femtosecond radiation in single-mode fibers. *IEEE Sensors Journal* **2008**, *8*, 1223-1228.

[54] Frazão, O., Ferreira, L., Araújo, F.; Santos, J. Applications of fiber optic grating technology to multi-parameter measurement. *Fiber and integrated optics* **2005**, *24*, 227-244.

[55] Yang, R., Yu, Y.-S., Chen, C., Xue, Y., Zhang, X.-L., Guo, J.-C., Wang, C., Zhu, F., Zhang, B.-L.; Chen, Q.-D. S-tapered fiber sensors for highly sensitive measurement of refractive index and axial strain. *Journal of Lightwave Technology* **2012**, *30*, 3126-3132.

[56] Rao, Y.-J., Wang, Y.-P., Ran, Z.-L.; Zhu, T. Novel fiber-optic sensors based on long-period fiber gratings written by high-frequency CO 2 laser pulses. *Journal of Lightwave Technology* **2003**, *21*, 1320.

[57] Zhao, C.-L., Yang, X., Demokan, M.; Jin, W. Simultaneous temperature and refractive

index measurements using a 3 slanted multimode fiber Bragg grating. *Journal of lightwave technology* **2006**, *24*, 879.

[58] Lu, P., Men, L., Sooley, K.; Chen, Q. Tapered fiber Mach–Zehnder interferometer for simultaneous measurement of refractive index and temperature. *Applied Physics Letters* **2009**, *94*, 131110.

[59] Hu, D.J.J., Lim, J.L., Jiang, M., Wang, Y., Luan, F., Shum, P.P., Wei, H.; Tong, W. Long period grating cascaded to photonic crystal fiber modal interferometer for simultaneous measurement of temperature and refractive index. *Optics letters* **2012**, *37*, 2283-2285.

[60] Kim, H.-J., Kwon, O.-J., Lee, S.; Han, Y.-G. Polarization-dependent refractometer for discrimination of temperature and ambient refractive index. *Optics letters* **2012**, *37*, 1802-1804.

[61] Lu, P., Harris, J., Xu, Y., Lu, Y., Chen, L.; Bao, X. Simultaneous refractive index and temperature measurements using a tapered bend-resistant fiber interferometer. *Optics letters* **2012**, *37*, 4567-4569.

[62] Lee, S.-M., Saini, S.S.; Jeong, M.-Y. Simultaneous measurement of refractive index, temperature, and strain using etched-core fiber Bragg grating sensors. *IEEE Photonics Technology Letters* **2010**, *22*, 1431-1433.

[63] Alberto, N.J., Marques, C.A., Pinto, J.L.; Nogueira, R.N. Three-parameter optical fiber sensor based on a tilted fiber Bragg grating. *Applied Optics* **2010**, *49*, 6085-6091.

[64] Men, L., Lu, P.; Chen, Q. Intelligent multiparameter sensing with fiber Bragg gratings. *Applied Physics Letters* **2008**, *93*, 071110.

[65] Trono, C., Baldini, F., Brenci, M., Chiavaioli, F.; Mugnaini, M. Flow cell for strain-and temperature-compensated refractive index measurements by means of cascaded optical fibre long period and Bragg gratings. *Measurement Science and Technology* **2011**, *22*, 075204.

[66] Harris, J., Lu, P., Larocque, H., Xu, Y., Chen, L.; Bao, X. Highly sensitive in-fiber interferometric refractometer with temperature and axial strain compensation. *Optics express* **2013**, *21*, 9996-10009.

[67] Jin, W., Michie, W.C., Thursby, G., Konstantaki, M.; Culshaw, B. Simultaneous measurement of strain and temperature: error analysis. *Optical Engineering* **1997**, *36*, 598-609.

[68] de Matos, C.J., Menezes, L.d.S., Brito-Silva, A.M., Gámez, M.M., Gomes, A.S.; de Araújo, C.B. Random fiber laser. *Physical review letters* **2007**, *99*, 153903.

[69] Gysel, P.; Staubli, R.K. Statistical properties of Rayleigh backscattering in single-mode fibers. *Journal of Lightwave Technology* **1990**, *8*, 561-567.

[70] Van Deventer, M.O. Polarization properties of Rayleigh backscattering in single-mode fibers. *Journal of Lightwave Technology* **1993**, *11*, 1895-1899.

[71] Fotiadi, A.A.; Kiyan, R.V. Cooperative stimulated Brillouin and Rayleigh backscattering process in optical fiber. *Optics letters* **1998**, *23*, 1805-1807.

[72] Zhu, T., Bao, X.; Chen, L. A single longitudinal-mode tunable fiber ring laser based on stimulated Rayleigh scattering in a nonuniform optical fiber. *Journal of Lightwave Technology* **2011**, *29*, 1802-1807.

[73] Li, M.-J., Li, S.; Nolan, D.A. Nonlinear fibers for signal processing using optical Kerr effects. *Journal of lightwave technology* **2005**, *23*, 3606.

[74] Lizárraga, N., Puente, N., Chaikina, E., Leskova, T.; Méndez, E. Single-mode Er-doped fiber random laser with distributed Bragg grating feedback. *Optics express* **2009**, *17*, 395-404.

[75] Li, Y., Lu, P., Bao, X.; Ou, Z. Random spaced index modulation for a narrow linewidth tunable fiber laser with low intensity noise. *Optics letters* **2014**, *39*, 2294-2297.

[76] Zhu, T., Chen, F., Huang, S.; Bao, X. An ultra-narrow linewidth fiber laser based on Rayleigh backscattering in a tapered optical fiber. *Laser Physics Letters* **2013**, *10*, 055110.

[77] Agrawal, G.P. *Nonlinear fiber optics*, ed.; Academic press: 2007.

[78] Rao, Y., Zhang, W., Zhu, J., Yang, Z., Wang, Z.; Jia, X. Hybrid lasing in an ultra-long ring fiber laser. *Optics express* **2012**, *20*, 22563-22568.

[79] Churkin, D., Vatnik, I., Turitsyn, S.; Babin, S. Random distributed feedback Raman fiber laser operating in a 1.2 μm wavelength range. *Laser Physics* **2011**, *21*, 1525-1529.

[80] Teng, R., Ding, Y.; Chen, L. Random fiber laser operating at 1,115 nm. *Applied Physics B* **2013**, *111*, 169-172.

[81] El-Taher, A.E., Harper, P., Babin, S., Churkin, D., Podivilov, E., Ania-Castanon, J.D.; Turitsyn, S. Effect of Rayleigh-scattering distributed feedback on multiwavelength Raman fiber laser generation. *Optics letters* **2011**, *36*, 130-132.

[82] Sugavanam, S., Yan, Z., Kamynin, V., Kurkov, A., Zhang, L.; Churkin, D. Multiwavelength generation in a random distributed feedback fiber laser using an all fiber Lyot filter. *Optics express* **2014**, *22*, 2839-2844.

[83] Pinto, A.M., Frazão, O., Santos, J.; Lopez-Amo, M. Multiwavelength fiber laser based on a photonic crystal fiber loop mirror with cooperative Rayleigh scattering. *Applied Physics B: Lasers and Optics* **2010**, *99*, 391-395.

[84] Pinto, A., Frazão, O., Santos, J.; Lopez-Amo, M. Multiwavelength Raman fiber lasers

using Hi-Bi photonic crystal fiber loop mirrors combined with random cavities. *Journal of Lightwave Technology* **2011**, *29*, 1482-1488.

[85] Tkach, R.W., Chraplyvy, A.R.; Derosier, R. Spontaneous Brillouin scattering for single-mode optical-fibre characterisation. *Electronics Letters* **1986**, *22*, 1011-1013.

[86] Pang, M., Xie, S., Bao, X., Zhou, D.-P., Lu, Y.; Chen, L. Rayleigh scattering-assisted narrow linewidth Brillouin lasing in cascaded fiber. *Optics letters* **2012**, *37*, 3129-3131.

[87] Pang, M., Bao, X.; Chen, L. Observation of narrow linewidth spikes in the coherent Brillouin random fiber laser. *Optics letters* **2013**, *38*, 1866-1868.

[88] Pang, M., Bao, X., Chen, L., Qin, Z., Lu, Y.; Lu, P. Frequency stabilized coherent Brillouin random fiber laser: theory and experiments. *Optics express* **2013**, *21*, 27155-27168.

[89] Giles, C.R.; Desurvire, E. Modeling erbium-doped fiber amplifiers. *Journal of lightwave technology* **1991**, *9*, 271-283.

[90] Saxena, B., Bao, X.; Chen, L. Suppression of thermal frequency noise in erbium-doped fiber random lasers. *Optics letters* **2014**, *39*, 1038-1041.

[91] Okoshi, T., Kikuchi, K.; Nakayama, A. Novel method for high resolution measurement of laser output spectrum. *Electronics letters* **1980**, *16*, 630-631.

[92] Iiyama, K., Hayashi, K.-i., Ida, Y., Ikeda, H.; Sakai, Y. Reflection-type delayed self-homodyne/heterodyne method for optical linewidth measurements. *Journal of lightwave technology* **1991**, *9*, 635-640.

[93] Dawson, J.W., Park, N.; Vahala, K.J. An improved delayed self-heterodyne interferometer for linewidth measurements. *IEEE Photonics Technology Letters* **1992**, *4*, 1063-1066.

[94] Güttner, A., Welling, H., Gericke, K.; Seifert, W. Fine structure of the field autocorrelation function of a laser in the threshold region. *Physical Review A* **1978**, *18*, 1157.

[95] Gallion, P.; Debarge, G. Quantum phase noise and field correlation in single frequency semiconductor laser systems. *IEEE Journal of Quantum Electronics* **1984**, *20*, 343-349.

[96] Rowe, H.E. Signals and noise in communication systems. **1965**,

[97] Cranch, G.; Miller, G. Fundamental frequency noise properties of extended cavity erbium fiber lasers. *Optics letters* **2011**, *36*, 906-908.

[98] Xu, D., Yang, F., Chen, D., Wei, F., Cai, H., Fang, Z.; Qu, R. Laser phase and frequency noise measurement by Michelson interferometer composed of a 3×3 optical fiber coupler. *Optics express* **2015**, *23*, 22386-22393.

[99] Takushima, Y., Choi, H.; Chung, Y.C. Measurement of Differential Phasor Diagram of Multilevel DPSK Signals by Using an Adjustment-Free Delay Interferometer Composed of a 3×3 Optical Coupler. *Journal of Lightwave Technology* **2009**, *27*, 718-730.

[100] Welch, P. The use of fast Fourier transform for the estimation of power spectra: a method based on time averaging over short, modified periodograms. *IEEE Transactions on audio and electroacoustics* **1967**, *15*, 70-73.

[101] Jia, X.-H., Rao, Y.-J., Peng, F., Wang, Z.-N., Zhang, W.-L., Wu, H.-J.; Jiang, Y. Random-lasing-based distributed fiber-optic amplification. *Optics express* **2013**, *21*, 6572-6577.

[102] Wang, Z., Rao, Y., Wu, H., Li, P., Jiang, Y., Jia, X.; Zhang, W. Long-distance fiber-optic point-sensing systems based on random fiber lasers. *Optics express* **2012**, *20*, 17695-17700.

[103] Fernandez-Vallejo, M., Bravo, M.; Lopez-Amo, M. Ultra-long laser systems for remote fiber Bragg gratings arrays interrogation. *IEEE Photonics Technology Letters* **2013**, *25*, 1362-1364.

[104] Jia, X.-H., Rao, Y.-J., Wang, Z.-N., Zhang, W.-L., Jiang, Y., Zhu, J.-M.; Yang, Z.-X. Towards fully distributed amplification and high-performance long-range distributed sensing based on random fiber laser. OFS2012 22nd International Conference on Optical Fiber Sensor,

[105] Wang, Z., Zeng, J., Li, J., Fan, M., Wu, H., Peng, F., Zhang, L., Zhou, Y.; Rao, Y. Ultra-long phase-sensitive OTDR with hybrid distributed amplification. *Optics letters* **2014**, *39*, 5866-5869.

[106] Li, Y., Lu, P., Baset, F., Ou, Z., Song, J., Alshehri, A., Bhardwaj, V.R.; Bao, X. Narrow linewidth low frequency noise Er-doped fiber ring laser based on femtosecond laser induced random feedback. *Applied Physics Letters* **2014**, *105*, 101105.

[107] Gouedard, C., Husson, D., Sauteret, C., Auzel, F.; Migus, A. Generation of spatially incoherent short pulses in laser-pumped neodymium stoichiometric crystals and powders. *JOSA B* **1993**, *10*, 2358-2363.

[108] Sha, W., Liu, C.-H.; Alfano, R. Spectral and temporal measurements of laser action of Rhodamine 640 dye in strongly scattering media. *Optics letters* **1994**, *19*, 1922-1924.

[109] Wiersma, D.S.; Lagendijk, A. Light diffusion with gain and random lasers. *Physical Review E* **1996**, *54*, 4256.

[110] Gottardo, S., Cavalieri, S., Yaroshchuk, O.; Wiersma, D.S. Quasi-two-dimensional diffusive random laser action. *Physical review letters* **2004**, *93*, 263901.

[111] Wiersma, D.S. The physics and applications of random lasers. *Nature physics* **2008**, *4*,

359-367.

[112] Williams, G., Bayram, S., Rand, S., Hinklin, T.; Laine, R. Laser action in strongly scattering rare-earth-metal-doped dielectric nanophosphors. *Physical Review A* **2001**, *65*, 013807.

[113] Meng, X., Fujita, K., Zong, Y., Murai, S.; Tanaka, K. Random lasers with coherent feedback from highly transparent polymer films embedded with silver nanoparticles. *Applied Physics Letters* **2008**, *92*, 201112.

[114] Ip, E., Lau, A.P.T., Barros, D.J.; Kahn, J.M. Coherent detection in optical fiber systems. *Optics express* **2008**, *16*, 753-791.

[115] Subías, J., Heras, C., Pelayo, J.; Villuendas, F. All in fiber optical frequency metrology by selective Brillouin amplification of single peak in an optical comb. *Optics express* **2009**, *17*, 6753-6758.

[116] Guyomarc'h, D., Hagel, G., Zumsteg, C.; Knoop, M. Some aspects of simulation and realization of an optical reference cavity. *Physical Review A* **2009**, *80*, 063802.

[117] Campos, J.M., Destrez, A., Jacquet, J.; Toffano, Z. Ultra-fast optical spectrum analyzer for DWDM applications. *IEEE Transactions on Instrumentation and Measurement* **2004**, *53*, 124-129.

[118] Takakura, T., Iga, K.; Tako, T. Linewidth measurement of a single longitudinal mode AlGaAs laser with a Fabry-Perot interferometer. *Japanese Journal of Applied Physics* **1980**, *19*, L725.

[119] Ludvigsen, H., Tossavainen, M.; Kaivola, M. Laser linewidth measurements using self-homodyne detection with short delay. *Optics Communications* **1998**, *155*, 180-186.

[120] Horak, P.; Loh, W.H. On the delayed self-heterodyne interferometric technique for determining the linewidth of fiber lasers. *Optics express* **2006**, *14*, 3923-3928.

[121] Han, M.; Wang, A. Analysis of a loss-compensated recirculating delayed self-heterodyne interferometer for laser linewidth measurement. *Applied Physics B: Lasers and Optics* **2005**, *81*, 53-58.

[122] Chen, X., Han, M., Zhu, Y., Dong, B.; Wang, A. Implementation of a loss-compensated recirculating delayed self-heterodyne interferometer for ultranarrow laser linewidth measurement. *Applied optics* **2006**, *45*, 7712-7717.

[123] Domingo, J.S., Pelayo, J., Villuendas, F., Heras, C.; Pellejer, E. Very high resolution optical spectrometry by stimulated Brillouin scattering. *IEEE Photonics Technology Letters* **2005**, *17*, 855-857.

[124] Sevillano, P., Subías, J., Heras, C., Pelayo, J.; Villuendas, F. Brillouin induced self-heterodyne technique for narrow line width measurement. *Optics express* **2010**, *18*,

15201-15206.

[125] Mihélic, F., Bacquet, D., Zemmouri, J.; Szriftgiser, P. Ultrahigh resolution spectral analysis based on a Brillouin fiber laser. *Optics letters* **2010**, *35*, 432-434.

[126] Bao, X.; Chen, L. Recent progress in Brillouin scattering based fiber sensors. *Sensors* **2011**, *11*, 4152-4187.

[127] Churkin, D.V., Sugavanam, S., Vatnik, I.D., Wang, Z., Podivilov, E.V., Babin, S.A., Rao, Y.; Turitsyn, S.K. Recent advances in fundamentals and applications of random fiber lasers. *Advances in Optics and Photonics* **2015**, *7*, 516-569.

[128] Fotiadi, A.A. Random lasers: An incoherent fibre laser. *Nature Photonics* **2010**, *4*, 204-205.

[129] Sugavanam, S., Tarasov, N., Shu, X.; Churkin, D.V. Narrow-band generation in random distributed feedback fiber laser. *Optics express* **2013**, *21*, 16466-16472.

[130] El-Taher, A., Alcon-Camas, M., Babin, S., Harper, P., Ania-Castanón, J.D.; Turitsyn, S.K. Dual-wavelength, ultralong Raman laser with Rayleigh-scattering feedback. *Optics letters* **2010**, *35*, 1100-1102.

[131] Babin, S., El-Taher, A., Harper, P., Podivilov, E.; Turitsyn, S. Tunable random fiber laser. *Physical Review A* **2011**, *84*, 021805.

[132] Churkin, D.V., El-Taher, A.E., Vatnik, I.D., Ania-Castañón, J.D., Harper, P., Podivilov, E.V., Babin, S.A.; Turitsyn, S.K. Experimental and theoretical study of longitudinal power distribution in a random DFB fiber laser. *Optics express* **2012**, *20*, 11178-11188.

[133] Smirnov, S.V.; Churkin, D.V. Modeling of spectral and statistical properties of a random distributed feedback fiber laser. *Optics express* **2013**, *21*, 21236-21241.

[134] Xu, Y., Xiang, D., Ou, Z., Lu, P.; Bao, X. Random Fabry–Perot resonator-based sub-kHz Brillouin fiber laser to improve spectral resolution in linewidth measurement. *Optics letters* **2015**, *40*, 1920-1923.

[135] Xiang, D., Lu, P., Xu, Y., Gao, S., Chen, L.; Bao, X. Truly random bit generation based on a novel random Brillouin fiber laser. *Optics letters* **2015**, *40*, 5415-5418.

[136] Xu, Y., Lu, P., Gao, S., Xiang, D., Mihailov, S.; Bao, X. Optical fiber random grating-based multiparameter sensor. *Optics letters* **2015**, *40*, 5514-5517.

[137] Gaeta, A.L.; Boyd, R.W. Stimulated Brillouin scattering in the presence of external feedback. *International Journal of Nonlinear Optical Physics* **1992**, *1*, 581-594.

[138] Chiu, B.; Hastings, M.C. Digital demodulation for passive homodyne optical fiber interferometry based on a 3 x 3 coupler. SPIE's 1994 International Symposium on Optics, Imaging, and Instrumentation,

[139] Foster, S., Tikhomirov, A.; Milnes, M. Fundamental thermal noise in distributed feedback fiber lasers. *IEEE journal of quantum electronics* **2007**, *43*, 378-384.

[140] Foster, S., Cranch, G.A.; Tikhomirov, A. Experimental evidence for the thermal origin of 1/f frequency noise in erbium-doped fiber lasers. *Physical Review A* **2009**, *79*, 053802.

[141] Zhu, J.-L., Li, W.-H., Sun, Y., Lu, J.-G., Song, X.-L., Chen, C.-Y., Zhang, Z.; Su, Y. Random laser emission in a sphere-phase liquid crystal. *Applied Physics Letters* **2015**, *106*, 191903.

[142] Sakai, M., Inose, Y., Ema, K., Ohtsuki, T., Sekiguchi, H., Kikuchi, A.; Kishino, K. Random laser action in GaN nanocolumns. *Applied Physics Letters* **2010**, *97*, 151109.

[143] Yu, S., Yuen, C., Lau, S., Park, W.I.; Yi, G.-C. Random laser action in ZnO nanorod arrays embedded in ZnO epilayers. *Applied physics letters* **2004**, *84*, 3241-3243.

[144] Dubois, J.; La Rochelle, S., *Active cooperative tuned identification friend or foe (ACTIFF)*. 1999, Google Patents.

[145] Wiersma, D.S.; Cavalieri, S. Light emission: A temperature-tunable random laser. *Nature* **2001**, *414*, 708-709.

[146] Redding, B., Choma, M.A.; Cao, H. Speckle-free laser imaging using random laser illumination. *Nature photonics* **2012**, *6*, 355-359.

[147] Choe, R., Corlu, A., Lee, K., Durduran, T., Konecky, S.D., Grosicka‐Koptyra, M., Arridge, S.R., Czerniecki, B.J., Fraker, D.L.; DeMichele, A. Diffuse optical tomography of breast cancer during neoadjuvant chemotherapy: a case study with comparison to MRI. *Medical physics* **2005**, *32*, 1128-1139.

[148] Vatnik, I.D., Churkin, D.V.; Babin, S.A. Power optimization of random distributed feedback fiber lasers. *Optics express* **2012**, *20*, 28033-28038.

[149] Hu, Z., Miao, B., Wang, T., Fu, Q., Zhang, D., Ming, H.; Zhang, Q. Disordered microstructure polymer optical fiber for stabilized coherent random fiber laser. *Optics letters* **2013**, *38*, 4644-4647.

[150] Martins, H., Marques, M.B.; Frazão, O. 300 km-ultralong Raman fiber lasers using a distributed mirror for sensing applications. *Optics express* **2011**, *19*, 18149-18154.

[151] Jia, X.-H., Rao, Y.-J., Wang, Z.-N., Zhang, W.-L., Yuan, C.-X., Yan, X.-D., Li, J., Wu, H., Zhu, Y.-Y.; Peng, F. Distributed Raman amplification using ultra-long fiber laser with a ring cavity: characteristics and sensing application. *Optics express* **2013**, *21*, 21208-21217.

[152] Dorighi, J.F., Krishnaswamy, S.; Achenbach, J.D. Stabilization of an embedded fiber optic Fabry-Perot sensor for ultrasound detection. *IEEE transactions on ultrasonics,*

ferroelectrics, and frequency control **1995**, *42*, 820-824.

[153] Dewhurst, R.J.; Shan, Q. Optical remote measurement of ultrasound. *Measurement Science and Technology* **1999**, *10*, R139.

[154] Betz, D.C., Thursby, G., Culshaw, B.; Staszewski, W.J. Acousto-ultrasonic sensing using fiber Bragg gratings. *Smart Materials and Structures* **2003**, *12*, 122.

[155] Xu, M.; Wang, L.V. Photoacoustic imaging in biomedicine. *Review of scientific instruments* **2006**, *77*, 041101.

[156] Wild, G.; Hinckley, S. Acousto-ultrasonic optical fiber sensors: overview and state-of-the-art. *IEEE Sensors Journal* **2008**, *8*, 1184-1193.

[157] Grosse, C.U.; Ohtsu, M. *Acoustic emission testing*, ed.; Springer Science & Business Media: 2008.

[158] Fomitchov, P.; Krishnaswamy, S. Response of a fiber Bragg grating ultrasonic sensor. *Optical Engineering* **2003**, *42*, 956-963.

[159] Qiao, Y., Zhou, Y.; Krishnaswamy, S. Adaptive demodulation of dynamic signals from fiber Bragg gratings using two-wave mixing technology. *Applied optics* **2006**, *45*, 5132-5142.

[160] Tsuda, H., Kumakura, K.; Ogihara, S. Ultrasonic sensitivity of strain-insensitive fiber Bragg grating sensors and evaluation of ultrasound-induced strain. *Sensors* **2010**, *10*, 11248-11258.

[161] Liu, T., Hu, L.; Han, M. Multiplexed fiber-ring laser sensors for ultrasonic detection. *Optics express* **2013**, *21*, 30474-30480.

[162] Guan, B.-O., Jin, L., Zhang, Y.; Tam, H.-Y. Polarimetric heterodyning fiber grating laser sensors. *Journal of lightwave technology* **2012**, *30*, 1097-1112.

[163] Perez, I.M., Cui, H.; Udd, E. Acoustic emission detection using fiber Bragg gratings. SPIE's 8th Annual International Symposium on Smart Structures and Materials,

[164] Okabe, Y., Fujibayashi, K., Shimazaki, M., Soejima, H.; Ogisu, T. Delamination detection in composite laminates using dispersion change based on mode conversion of Lamb waves. *Smart materials and structures* **2010**, *19*, 115013.

[165] Wu, Q.; Okabe, Y. Ultrasonic sensor employing two cascaded phase-shifted fiber Bragg gratings suitable for multiplexing. *Optics letters* **2012**, *37*, 3336-3338.

[166] Wu, Q.; Okabe, Y. High-sensitivity ultrasonic phase-shifted fiber Bragg grating balanced sensing system. *Optics express* **2012**, *20*, 28353-28362.

[167] Rosenthal, A., Razansky, D.; Ntziachristos, V. High-sensitivity compact ultrasonic detector based on a pi-phase-shifted fiber Bragg grating. *Optics letters* **2011**, *36*, 1833-

1835.

[168] Rosenthal, A., Kellnberger, S., Bozhko, D., Chekkoury, A., Omar, M., Razansky, D.; Ntziachristos, V. Sensitive interferometric detection of ultrasound for minimally invasive clinical imaging applications. *Laser & Photonics Reviews* **2014**, *8*, 450-457.

[169] Tsuda, H. Fiber Bragg grating vibration-sensing system, insensitive to Bragg wavelength and employing fiber ring laser. *Optics letters* **2010**, *35*, 2349-2351.

[170] Han, M., Liu, T., Hu, L.; Zhang, Q. Intensity-demodulated fiber-ring laser sensor system for acoustic emission detection. *Optics express* **2013**, *21*, 29269-29276.

[171] Wu, Q., Okabe, Y.; Sun, J. Investigation of dynamic properties of erbium fiber laser for ultrasonic sensing. *Optics express* **2014**, *22*, 8405-8419.

[172] Xu, Y., Zhang, M., Lu, P., Mihailov, S.; Bao, X. Multi-parameter sensor based on random fiber lasers. *AIP Advances* **2016**, *6*, 095009.

[173] Minardo, A., Cusano, A., Bernini, R., Zeni, L.; Giordano, M. Response of fiber Bragg gratings to longitudinal ultrasonic waves. *IEEE transactions on ultrasonics, ferroelectrics, and frequency control* **2005**, *52*, 304-312.

[174] Liu, T.; Han, M. Analysis of π-Phase-Shifted Fiber Bragg Gratings for Ultrasonic Detection. *IEEE Sensors Journal* **2012**, *12*, 2368-2373.

[175] Feigenbaum, M.J. The onset spectrum of turbulence. *Physics Letters A* **1979**, *74*, 375-378.

[176] Sciamanna, M.; Shore, K.A. Physics and applications of laser diode chaos. *Nature Photonics* **2015**, *9*, 151-162.

[177] Wu, W.-T., Liao, Y.-H.; Lin, F.-Y. Noise suppressions in synchronized chaos lidars. *Optics express* **2010**, *18*, 26155-26162.

[178] Argyris, A., Syvridis, D., Larger, L., Annovazzi-Lodi, V., Colet, P., Fischer, I., Garcia-Ojalvo, J., Mirasso, C.R., Pesquera, L.; Shore, K.A. Chaos-based communications at high bit rates using commercial fibre-optic links. *Nature* **2005**, *438*, 343-346.

[179] Lin, F.-Y.; Liu, J.-M. Diverse waveform generation using semiconductor lasers for radar and microwave applications. *IEEE journal of quantum electronics* **2004**, *40*, 682-689.

[180] Annovazzi-Lodi, V., Aromataris, G., Benedetti, M.; Merlo, S. Secure chaotic transmission on a free-space optics data link. *IEEE Journal of Quantum Electronics* **2008**, *44*, 1089-1095.

[181] Lin, F.-Y.; Liu, J.-M. Chaotic lidar. *IEEE journal of selected topics in quantum electronics* **2004**, *10*, 991-997.

[182] Uchida, A., Davis, P.; Itaya, S. Generation of information theoretic secure keys using a chaotic semiconductor laser. *Applied physics letters* **2003**, *83*, 3213-3215.

[183] Takeuchi, Y., Shogenji, R.; Ohtsubo, J. Chaotic dynamics in semiconductor lasers subjected to polarization-rotated optical feedback. *Applied Physics Letters* **2008**, *93*, 181105.

[184] Wang, A., Li, P., Zhang, J., Zhang, J., Li, L.; Wang, Y. 4.5 Gbps high-speed real-time physical random bit generator. *Optics express* **2013**, *21*, 20452-20462.

[185] Wang, A., Wang, L., Li, P.; Wang, Y. Minimal-post-processing 320-Gbps true random bit generation using physical white chaos. *Optics Express* **2017**, *25*, 3153-3164.

[186] Mørk, J., Mark, J.; Tromborg, B. Route to chaos and competition between relaxation oscillations for a semiconductor laser with optical feedback. *Physical review letters* **1990**, *65*, 1999.

[187] Erneux, T., Gavrielides, A.; Sciamanna, M. Stable microwave oscillations due to external-cavity-mode beating in laser diodes subject to optical feedback. *Physical Review A* **2002**, *66*, 033809.

[188] Rontani, D., Locquet, A., Sciamanna, M., Citrin, D.S.; Ortin, S. Time-delay identification in a chaotic semiconductor laser with optical feedback: a dynamical point of view. *IEEE Journal of Quantum Electronics* **2009**, *45*, 879-1891.

[189] Rontani, D., Locquet, A., Sciamanna, M.; Citrin, D. Loss of time-delay signature in the chaotic output of a semiconductor laser with optical feedback. *Optics letters* **2007**, *32*, 2960-2962.

[190] Wu, J.-G., Xia, G.-Q.; Wu, Z.-M. Suppression of time delay signatures of chaotic output in a semiconductor laser with double optical feedback. *Optics express* **2009**, *17*, 20124-20133.

[191] Li, S.-S.; Chan, S.-C. Chaotic time-delay signature suppression in a semiconductor laser with frequency-detuned grating feedback. *IEEE Journal of Selected Topics in Quantum Electronics* **2015**, *21*, 541-552.

[192] Li, S.-S., Liu, Q.; Chan, S.-C. Distributed feedbacks for time-delay signature suppression of chaos generated from a semiconductor laser. *IEEE Photonics Journal* **2012**, *4*, 1930-1935.

[193] Hong, Y. Experimental study of time-delay signature of chaos in mutually coupled vertical-cavity surface-emitting lasers subject to polarization optical injection. *Optics express* **2013**, *21*, 17894-17903.

[194] Wu, J.-G., Wu, Z.-M., Tang, X., Lin, X.-D., Deng, T., Xia, G.-Q.; Feng, G.-Y. Simultaneous generation of two sets of time delay signature eliminated chaotic signals by using mutually coupled semiconductor lasers. *IEEE Photonics Technology Letters*

2011, *23*, 759-761.

[195] Li, N., Pan, W., Xiang, S., Yan, L., Luo, B.; Zou, X. Loss of time delay signature in broadband cascade-coupled semiconductor lasers. *IEEE Photonics Technology Letters* **2012**, *24*, 2187-2190.

[196] Sunada, S., Harayama, T., Arai, K., Yoshimura, K., Davis, P., Tsuzuki, K.; Uchida, A. Chaos laser chips with delayed optical feedback using a passive ring waveguide. *Optics express* **2011**, *19*, 5713-5724.

[197] Uchida, A., Heil, T., Liu, Y., Davis, P.; Aida, T. High-frequency broad-band signal generation using a semiconductor laser with a chaotic optical injection. *IEEE journal of quantum electronics* **2003**, *39*, 1462-1467.

[198] Lang, R.; Kobayashi, K. External optical feedback effects on semiconductor injection laser properties. *IEEE journal of Quantum Electronics* **1980**, *16*, 347-355.

[199] Wang, A., Yang, Y., Wang, B., Zhang, B., Li, L.; Wang, Y. Generation of wideband chaos with suppressed time-delay signature by delayed self-interference. *Optics express* **2013**, *21*, 8701-8710.

[200] Agrawal, G.P.; Dutta, N.K. *Semiconductor lasers*, ed.; Springer Science & Business Media: 2013.